Active Torque Ripple Reduction in Permanent-Magnet AC Motors

by

Christopher Anthony Greamo
B.S., Electrical Engineering
Carnegie-Mellon University, 1993

Submitted to the Department of
Electrical Engineering and Computer Science
in Partial Fulfillment of the Requirements for the
Degree of

MASTER OF SCIENCE
in Electrical Engineering
at the

Massachusetts Institute of Technology

June 1995

Signature of Author_____
Department of EECS
April 13, 1995

Certified by_____
Bernard C. Lesieutre
Assist. Professor, EECS Department
Thesis Supervisor

Accepted by_____
Frederic R. Morgenthaler
Chairman, Committee on Graduate Students

Acknowledgments

I would like to offer my sincere thanks to a number people without whom completion of this project would not have been possible. To my advisor Dr. Bernard("Bernie") Lesieutre not only for his technical knowledge and insights, but also for his enthusiastic support of the project. To Scott Ellerthorpe, Peter Cho, Andrew Bedingfield of the Naval Undersea Warfare Center(NUWC) in Newport, R.I. and Dr. Duane Hanselman of the University of Maine for their individual insights into the physics of electric motors. To Andrew Barnett, John Raposa, and Dan Thivierge also of the NUWC for their combined technical assistance in the laboratory.

I would also like to offer thanks to my family and friends, especially to my girlfriend, Annukka, and my parents, Juliann and Anthony for their emotional support. It is deeply appreciated.

Active Torque Ripple Reduction in Permanent-Magnet AC Motors
by
Christopher Anthony Greamo

Submitted to the Department of Electrical Engineering and
Computer Science on April 13, 1995 in partial fulfillment
of the requirements for the Degree of Master of Science in
Electrical Engineering

Abstract

Autonomous Underwater Vehicles (AUVs) pose a unique challenge in the design of motor drive systems. The motor is required to be low weight and to produce high torque with high efficiency and reliability. Permanent-magnet AC (brushless DC) motors are well suited for this application. However, it is highly desirable that the motor work quietly to avoid disturbing the environment and/or detection. Unfortunately, permanent-magnet motors tend to have high torque ripple in trade-off for their high output torque and efficiency which results in persistent noise transmission with a well defined signature. The focus of this thesis is the study of torque ripple reduction methods for permanent-magnet motors in an attempt to design a drive system with high power density coupled with low torque ripple.

In this study, active shaping of the stator current waveforms is used to cancel torque ripple due to both slot harmonics and cogging effects. Both problems of current waveform selection and enforcement are addressed. A unique close-loop approach to selecting the appropriate current harmonics using estimates of the torque ripple spectrum from a load torque measurements is discussed. The scheme uses a model reference adaptive control algorithm which requires no a priori knowledge of motor parameters. A pulse-width modulation(PWM) scheme for imposing the current waveform on the stator windings with minimal phase and amplitude distortion is also presented. Detailed simulation results are provided which indicate that a better 80 dB reduction in torque ripple through active current control is possible without a significant reduction in the system's power efficiency.

Thesis Supervisor: Dr. Bernard L. Lesieutre
Title: Assistant Professor of Electrical Engineering

Table of Contents

1. Background Page 6

1.1 Autonomous Underwater Vehicles (AUVs).....6
1.2 Permanent-Magnetic AC Motors.....6
1.3 Axial-Field Motors.....7
1.4 Existing Torque Ripple Reduction Methods.....9

2. System Modeling Page 11

2.1 The Three-Phase Permanent-Magnet AC Motor (PMAC).....11
2.2 Tangential Torque in PMAC Motors.....16
2.3 Axial Forces in Axial-Field PMAC Motors.....21

3. Active Torque Ripple Reduction
Part I: Current Selection Page 23

3.1 Harmonic System Analysis.....23
3.2 Harmonic Analysis of PMAC Motor.....28
3.3 Minimum Torque Ripple Controller.....35
3.4 Harmonic System Simulation & Parameter Estimation.....39

4. Active Torque Ripple Reduction
Part II: Current Enforcement Page 51

4.1 The Current Controlled Voltage Source Inverter (CCVSI).....51
4.2 Standard Pulse-Width Modulation(PWM) Schemes.....55
4.3 Model Reference PWM Scheme.....57
4.4 Model Reference PWM CCVSI Simulation.....60
4.5 Model Reference PWM CCVSI Experimental Results.....67

5. Practical Issues Page 74

5.1 Power Electronic Limitations.....74
5.2 Torque Spectrum Measurements.....76

6. Detailed System Simulation Page 78

6.1 Simulation Parameters....78

6.2 Simulation Results....79

6.2.1 Baseline Simulation....79

6.2.2 Active Torque Ripple Reduction Simulation....86

6.2.3 Limited Current Harmonics Cases....91

6.2.4 Extended Simulation Run....94

7. Conclusions Page 99

7.1 Contributions....99

7.2 Summary of Results....100

7.3 Future Work....100

References Page 101

1 Background

1.1 Autonomous Underwater Vehicles (AUVs)

Autonomous Underwater Vehicles or AUVs are unmanned, submarine type vehicles which are designed to infiltrate and investigate dangerous or otherwise inaccessible underwater environments. **Figure 1.1** is a non-scale depiction of an AUV.

Figure 1.1: Side-View Sketch of AUV

The vehicles are completely self-contained. They usually use an electric drive system powered by internally carried batteries, and follow a pre-programmed mission with little or no external guidance. For this reason, power efficiency and system reliability are key design constraints.

The heart of many AUV missions is the collection of intelligence with minimal disturbance to the environment under observation. For military scenarios, stealth is especially important for mission success and vehicle survivability. To this end, it is important for the AUV drive system to operate relatively noise-free while maintaining high efficiency and reliability. A major noise source in electric motor drives is *torque ripple* or a variation in the motor's torque production due to unavoidable imperfections in the motor's construction. This torque ripple can excite mechanical modes in the drive shaft which transmit sounds at discrete frequencies into the environment defining an easily recognizable signature for the vehicle. The effect is most pronounced during low speed operation. For this reason, much effort has been directed by the U.S. Navy into understanding the causes torque ripple and developing methods to reduce it.

1.2 Permanent-Magnet AC Motors

Recent technological developments have made Permanent-Magnet AC or PMAC motors a viable choice for an AUV drive system. High power density permanent-magnet material can be used to make light-weight motors

capable of delivering very high torque[7]. Advances in power electronic devices and circuits result in highly efficient and reliable drive systems.

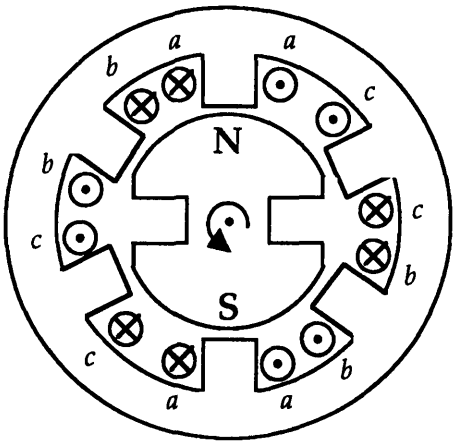

Figure 1.2: Cross Section of a Three-Phase Radial-Field PMAC Motor

An important engineering trade-off in PMAC motor design is power density and torque ripple[6]. In many PMAC motors, neither the stator nor the rotor have smooth profiles(**Figure 1.2**). Slots on the stator for the phase windings and the permanent magnet pieces on the rotor cause a "jagged" interface between the stator and rotor edges. Due to this saliency, the total tangential force on the rotor is not constant over all rotor positions. The forces caused by the interaction between a rough stator and the rotor are called "cogging" and "reluctance" torques. In a rotating machine, such as an AUV drive system, these torques produce periodic vibrations in the motor's total output torque and is one source of torque ripple.

1.3 Axial-Field Motors

Radial-Field PMAC motors, like the one depicted in **Figure 1.2**, are not the only PMAC configuration. Instead of surrounding the permanent-magnet rotor radially by the stator, the rotor and stator may be stacked axially as shown by **Figure 1.3**. The magnetic flux lines pass through the rotor parallel to the drive shaft(*i.e.* along the axial direction) instead of radially outward from the center of rotation. Note that the direction of the resulting force on the rotor is tangential(*i.e.* the same) for both configurations.

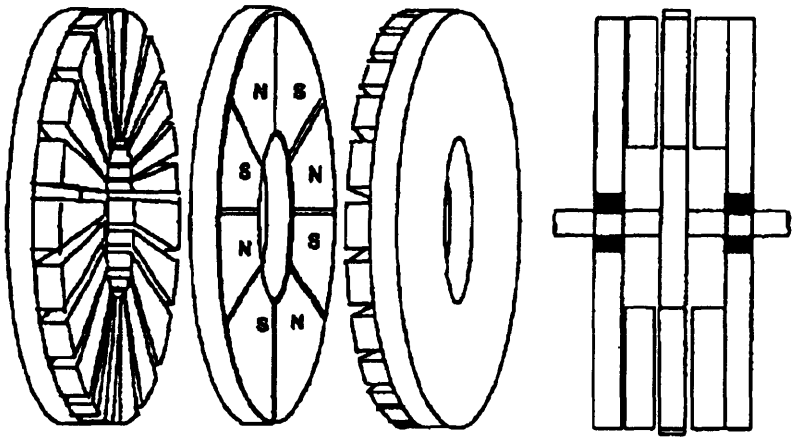

Figure 1.3: Side View of A Dual-Stator Axial-Field PMAC Motor

One major benefit of the axial-field configuration is the ability to use two stators, one placed on either side of the rotor. This feature allows high torques and efficiency, which are desirable for AUV drive systems.

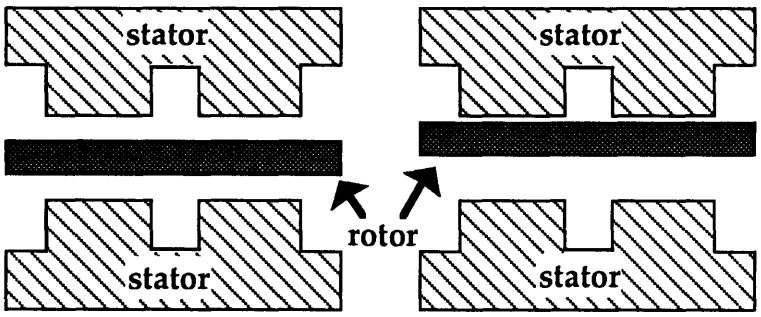

Figure 1.4: Aligned vs. Misaligned Rotor

There are two main drawbacks to the axial-field motor. One is the complexity of construction. Not only are there more basic pieces to the motor, alignment of the rotor between the two stators becomes a key issue(**Figure 1.4**). It has been shown in reference[6] that the motor performance is sensitive to even a small rotor misalignment. Secondly, axial-field motors suffer from larger torque ripple than equally sized radial-field motors. This torque ripple can have both an axial and tangential component in axial-field motors whereas traditional radial-field motors only have a tangential component. (This phenomena will discussed in Section 2.3.) There is a need for torque

ripple reducing techniques to realize the benefits of an axial-field configuration.

1.4 Existing Torque Ripple Reduction Methods

Torque ripple is considered a parasitic component in most motor systems. Electric machines are constructed in such a way to minimize the torque ripple component for the intended operational speed. This is done through the skewing of slots along the stator or other geometric variations in the motors construction(references [6], [9], and [14]). In vehicle drive applications, however, the requirements for high power and high efficiency make torque ripple minimization through motor design difficult. Drive systems are often required to operate over a wide speed range, making torque ripple minimization for the entire operational range nearly impossible through a fixed geometry design.

Research into torque ripple reduction through the shaping of the phase current waveforms has shown promise. Reference[2] includes an analysis of the physics of torque ripple in brushless DC motors and shows that the "optimal" phase current waveforms for ripple-free operation can be computed, in theory, given the motor's back electro-motive force (EMF) shapes. This work is extended in reference[3] in which an open-loop current controller was proposed and shown through computer simulation to produce ripple-free operation. Although this work provided insight into the origins of torque ripple in machines and provided motivation to the possibility of using control of phase currents to reduce torque ripple, the open-loop scheme did not address the issues of system stability, transient response, and robustness to parameter variations and assumes precise a priori knowledge of the motor's parameters.

A controls oriented approach to the problem of torque ripple cancellation is pursued in references [4] and [5] where an adaptive feedback controller is proposed that cancels torque ripple harmonics through the controlled addition of harmonics to the phase current waveform. Position and velocity feedback are used to "adapt" the magnitude of the applied current harmonics in real-time. System stability and robustness can be proven, and the controller requires nearly no knowledge of the motor's

parameters. There are some draw-backs to the approach. It is assumed that the current commands generated by the controller can be exactly followed by the power electronics; there are no limits on the amplitude or rate of change of the commanded phase currents. In addition, there is no clear relationship between applied current harmonics and the physical parameters of the motor. As such, it is not clear the current waveforms generated by the controller are "optimal" in the same sense shown by reference[3].

Most of the literature on torque ripple reduction has focused on radial-field machines. This is no doubtfully due to the large popularity of the radial-field topology. References [6] and [7] provide a detailed analysis of the sources of torque ripple in dual-stator axial-field motors and suggest some construction techniques to reduce the ripple. Little or no research, however, has been published on active torque ripple reduction techniques in axial-field motors. It is the goal of this thesis document to apply some of the existing knowledge and techniques concerning active torque ripple reduction to this promising yet under-utilized motor configuration.

2 System Modeling

Proper modeling of the dynamics of the permanent-magnetic motor is key to understanding the source of torque ripple. The following analysis will begin with the generic three phase electric machine equations which can be found in reference [27] and will develop a specific model for a dual-stator, permanent-magnet motor including tangential torque ripple. Some sources of axial torque ripple will also be discussed. Following the model development, specific conditions for torque ripple free operation will be derived.

2.1 The Three-Phase Permanent-Magnet AC Motor (PMAC)

A fifth-order dynamic model is used to model the three-phase permanent-magnet motor used in this study. There are two natural choices for the three electrical state-variables-- either the stator fluxes, λ_a, λ_b, and λ_c, or the stator currents, i_a, i_b, and i_c. Since current control power electronics will be used to drive the stator windings, the phase currents will be chosen as the state-variables. The two mechanical states are ω and θ representing the rotational velocity and position of the shaft, respectfully. By choosing the states in this manner, the motor may be viewed as two coupled subsystems-- one electrical, and the other mechanical. This is illustrated in **Figure 2.1**. Assuming an ideal flux/current relation and constant speed operation, the two subsystems are linear. This property has been exploited by a number of motor speed control schemes[4], [5], [21], and [26].

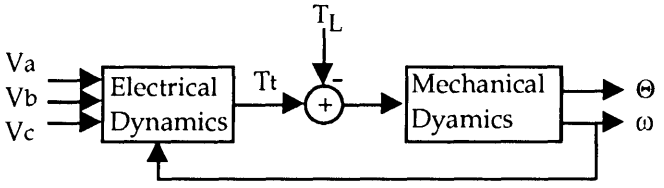

Figure 2.1: Motor System Block Diagram

The inputs V_a, V_b, and V_c are the phase winding voltages applied to the electrical subsystem via the stator. The outputs are the mechanical state-variables θ and ω. Other variables of interest include the tangential component of the electrical torque T_t, and the load torque T_L.

The electrical parameters of the motor include the phase winding resistance R_s and self-inductance L_s for each of three stator phases, and the mutual inductance L_m linking each of the phases to the magnetic rotor and to each other. The rate of change these inductance terms produces a voltage known as the excitation voltage whose amplitude is proportional to the shaft velocity ω. **Figure 2.2** is a linear circuit model for the electrical dynamics of a single motor phase.

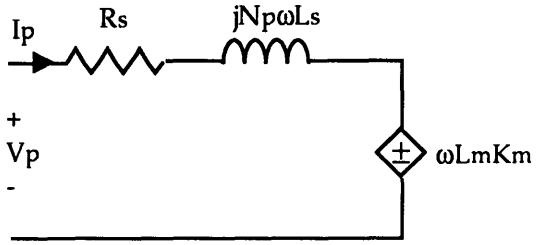

Figure 2.2: Phase Winding Model

For a symmetric three-phase machine, each winding may be modeled equivalently[38].

One may model the permanent-magnet rotor as another phase winding carrying constant current[27]. This increases the number of states in the system by one, however this *artificial* state can be discarded after using it to compute the form of the electrical torque equation, reducing the final model to a fifth-order model.

The vectors corresponding to the flux-linkages, applied voltages, and generated currents are given by Equations **(2.1)**, **(2.2)**, and **(2.3)**.

$$\Lambda = \begin{bmatrix} \lambda_a \\ \lambda_b \\ \lambda_c \\ \lambda_m \end{bmatrix} \quad (2.1) \qquad \mathbf{V} = \begin{bmatrix} V_a \\ V_b \\ V_c \\ 0 \end{bmatrix} \quad (2.2) \qquad \mathbf{i} = \begin{bmatrix} i_a \\ i_b \\ i_c \\ K_m \end{bmatrix} \quad (2.3)$$

The top three elements of each vector are the state and input variables for the three stator phases, labeled a, b, and c. The bottom entries represent the variables associated with the rotor phase. As is done in reference[27], the permanent-magnet is modeled as a *shorted* winding carrying a constant

current. This implies an applied voltage of zero(*i.e.* the bottom entry in Equation **(2.2)**) and a constant current(*i.e.* K_m in Equation **(2.3)**).

The resistance matrix is given by Equation **(2.4)** assuming the machine has similar phase windings, each with equal phase resistance R_S.

$$\mathbf{R} = \begin{bmatrix} R_s & 0 & 0 & 0 \\ 0 & R_s & 0 & 0 \\ 0 & 0 & R_s & 0 \\ 0 & 0 & 0 & 0 \end{bmatrix} \tag{2.4}$$

The fourth row and column of **R** correspond to the artificial rotor winding. Since this winding has a constant current and no applied voltage, it's phase resistant is zero. Equation **(2.5)** shows the form of the machine's inductance matrix.

$$\mathbf{L}(\theta) = \begin{bmatrix} L_{aa}(\theta) & L_{ab}(\theta) & L_{ac}(\theta) & L_{am}(\theta) \\ L_{ab}(\theta) & L_{bb}(\theta) & L_{bc}(\theta) & L_{bm}(\theta) \\ L_{ac}(\theta) & L_{bc}(\theta) & L_{cc}(\theta) & L_{cm}(\theta) \\ L_{am}(\theta) & L_{bm}(\theta) & L_{cm}(\theta) & L_{mm}(\theta) \end{bmatrix} \tag{2.5}$$

The notation L_{xx} refers to the self-inductance for phase x, and L_{xy} is the mutual-inductance between phase x and phase y, where a, b, and c are the three stator phases and m is the rotor phase. Assuming a symmetric machine, the stator self-inductances are equal(*i.e.* $L_{aa}=L_{bb}=L_{cc}$) and all mutual inductance terms are symmetric(*i.e.* $L_{xy}=L_{yx}$ for all x,y = a,b,c,m). In this model, all inductance terms are a function of rotor position θ. This implies that for a rotating motor, $\mathbf{L}(\theta)$ is periodic in θ with period 2π *electrical* radians(*i.e.* $\mathbf{L}(\theta+2\pi)=\mathbf{L}(\theta)$).

There are three fundamental physical equations underlying the motor's dynamics. *Faraday's* and *Ohm's Laws* specify the electrical dynamics,

$$\frac{d\Lambda}{dt} = \mathbf{V} - \mathbf{R}\mathbf{i} \tag{2.6}$$

Newton's Second Law of Motion specifies the mechanical dynamics, [J is the moment of inertia of the rotor, shaft, and load; T_t is the tangential component of the electrically generated torque; and T_L is the load torque].

$$J\frac{d\omega}{dt} = T_t - T_L \tag{2.7}$$

The second mechanical state, position, is the integral of speed.

$$\frac{d\theta}{dt} = \omega \tag{2.8}$$

As shown in Equation **(2.7)**, the net torque applied to the rotor at any given time is the difference between the torque due to the electrical interactions between the stator windings and the magnetic rotor, and the mechanical load torque opposing the movement of the shaft. The tangential component of the electrically generated torque T_t is given by Equation **(2.9)** [27].

$$T_t = \frac{1}{2}\mathbf{i}^T\frac{d\mathbf{L}}{d\theta}\mathbf{i} \tag{2.9}$$

In an axial-field motor, there are two components to the electrical torque--tangential and axial. Only the tangential component T_t contributes to working torque, and therefore, is the only component in Equation **(2.7)**. The axial component T_a contributes only to vibrations of the shaft through excitations of its axial modes. This will be discussed in greater detail in Sections 2.2 and 2.3. The load torque T_L is due to frictional forces which oppose the motion of the shaft in the environment. Since T_L is a manifestation of frictional type forces, it is some function of the rotor's rotational speed ω. For many typical loads, such as a propulsor in a viscous fluid, the load torque is best modeled by a quadratic function.

$$T_L = \mathrm{sgn}(\omega)(K_b\omega + K_p\omega^2) \tag{2.10}$$

The sgn(ω) multiplier insures that the torque always opposes the motion of the shaft.

Since the currents **i** were chosen as the electrical states, it is necessary to eliminate λ from Equation **(2.6)** before assembling the equations of the motor into the standard state-space form. Assuming an ideal flux/current relation, the flux vector λ can be expressed as the product of the inductance matrix **L** and the current vector **i**.

$$\Lambda = \mathbf{L}\mathbf{i} \tag{2.11}$$

Taking the time derivative of Equation **(2.11)** yields Equation **(2.12)**.

$$\begin{aligned}\frac{d\Lambda}{dt} &= \frac{d(\mathbf{L}\mathbf{i})}{dt} \\ &= \mathbf{L}\frac{d\mathbf{i}}{dt} + \frac{d\mathbf{L}}{dt}\mathbf{i} \\ &= \mathbf{L}\frac{d\mathbf{i}}{dt} + \frac{d\mathbf{L}}{d\theta}\frac{d\theta}{dt}\mathbf{i} \\ &= \mathbf{L}\frac{d\mathbf{i}}{dt} + \omega\frac{d\mathbf{L}}{d\theta}\mathbf{i}\end{aligned} \tag{2.12}$$

Finally, substituting Equation **(2.12)** into Equation **(2.6)** and collecting like terms yields Equation **(2.13)**.

$$\mathbf{L}\frac{d\mathbf{i}}{dt} = \mathbf{V} - [\mathbf{R} + \omega\frac{d\mathbf{L}}{d\theta}]\mathbf{i} \tag{2.13}$$

The inductance matrix **L** must be symmetric and positive-definite for any physically realizable machine(see reference[27] for proof). Thus, **L** must be invertible(*i.e.* $\mathbf{L}^{-1}$) exists. Multiplying Equation **(2.13)** by $\mathbf{L}^{-1}$ yields Equation **(2.14)**.

$$\frac{d\mathbf{i}}{dt} = \mathbf{L}^{-1}\mathbf{V} - \mathbf{L}^{-1}[\mathbf{R} + \omega\frac{d\mathbf{L}}{d\theta}]\mathbf{i} \tag{2.14}$$

$$\frac{d}{dt}\begin{bmatrix}\theta \\ \omega\end{bmatrix} = \begin{bmatrix}0 & 1 \\ 0 & 0\end{bmatrix}\begin{bmatrix}\theta \\ \omega\end{bmatrix} + \frac{1}{J}\begin{bmatrix}0 \\ T_t(i,\theta)\end{bmatrix} - \frac{1}{J}\begin{bmatrix}0 \\ T_L(\omega)\end{bmatrix} \tag{2.15}$$

Together, Equations **(2.14)** and **(2.15)** form the state-space model for the three-phase permanent-magnet motor.

2.2 Tangential Torque in PMAC Motors

As mentioned previously, only the tangential component of torque contributes to the desired rotational acceleration of the drive shaft, and thus, produces useful work. In radial-field motors, the torque of electrical origin has only a tangential component. In axial-field motors, the generated torque can have both tangential and axial components; the axial component will be further discussed in Section 2.3.

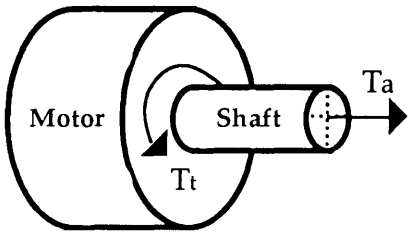

Figure 2.3: Tangential and Axial Torque Components

Equation **(2.9)** is the general equation for the tangential component of the torque of electrical origin. This equation is derived from energy conservation arguments. A detailed formulation can be found in reference[27]. Expanding the vector symbols in Equation **(2.9)** with the full matrix and vector representations yields Equation **(2.16)**.

$$T_t = \tfrac{1}{2}\begin{bmatrix} i_a & i_b & i_c & k_m \end{bmatrix} \begin{bmatrix} \frac{dL_{aa}}{d\theta} & \frac{dL_{ab}}{d\theta} & \frac{dL_{ac}}{d\theta} & \frac{dL_{am}}{d\theta} \\ \frac{dL_{ab}}{d\theta} & \frac{dL_{bb}}{d\theta} & \frac{dL_{bc}}{d\theta} & \frac{dL_{bm}}{d\theta} \\ \frac{dL_{ac}}{d\theta} & \frac{dL_{bc}}{d\theta} & \frac{dL_{cc}}{d\theta} & \frac{dL_{cm}}{d\theta} \\ \frac{dL_{am}}{d\theta} & \frac{dL_{bm}}{d\theta} & \frac{dL_{cm}}{d\theta} & \frac{dL_{mm}}{d\theta} \end{bmatrix} \begin{bmatrix} i_a \\ i_b \\ i_c \\ k_m \end{bmatrix} \qquad (2.16)$$

Performing the appropriate matrix multiplication and grouping common terms gives the scalar Equation **(2.17)**.

$$\begin{aligned} T_t = {} & \tfrac{1}{2}\left(i_a^2 \frac{dL_{aa}}{d\theta} + i_b^2 \frac{dL_{bb}}{d\theta} + i_c^2 \frac{dL_{cc}}{d\theta}\right) + \left(i_a i_b \frac{dL_{ab}}{d\theta} + i_a i_c \frac{dL_{ac}}{d\theta} + i_b i_c \frac{dL_{bc}}{d\theta}\right) \\ & + k_m\left(i_a \frac{dL_{am}}{d\theta} + i_b \frac{dL_{bm}}{d\theta} + i_c \frac{dL_{cm}}{d\theta}\right) \\ & + k_m^2 \frac{dL_{mm}}{d\theta} \end{aligned} \qquad (2.17)$$

In general, every inductance term will be a function of rotor position θ and can contribute to the net generated torque. For a rotating machine, these functions will all be periodic with period 2π *electrical* radians, and therefore, can all contribute to torque ripple. Depending on the motor's construction some terms may be negligible in comparison to others.

The tangential electrical torque T_t has three distinct physical origins. Equation **(2.17)** can be divided into three component, each representing a different source.

$$T_t = T_r + T_\mu + T_c \tag{2.18}$$

The first component T_r is called *reluctance torque.*

$$T_r = \tfrac{1}{2}(i_a^2 \frac{dL_{aa}}{d\theta} + i_b^2 \frac{dL_{bb}}{d\theta} + i_c^2 \frac{dL_{cc}}{d\theta}) + (i_a i_b \frac{dL_{ab}}{d\theta} + i_a i_c \frac{dL_{ac}}{d\theta} + i_b i_c \frac{dL_{bc}}{d\theta}) \tag{2.19}$$

As shown in Equation **(2.19)**, the reluctance torque expression contains products of the electrical state variables (*i.e.* the stator currents), and thus, is highly nonlinear. This torque component is caused by changes in the *stator* self-inductances with rotor position. These changes are induced by a time-varying reluctance path for the stator flux caused by rotor saliency. For switched reluctance motors, this component can be large and is the prime source of working torque. For synchronous PMAC motors, however, the reluctance torque is usually minimized though the use of a smooth rotor construction. This is the case for the dual axial-field motor under study here, and therefore, T_r is assumed to be negligible.

The second component T_μ is known as *mutual torque,* and for PM motors, is the main source of working torque.

$$T_\mu = k_m(i_a \frac{dL_{am}}{d\theta} + i_b \frac{dL_{bm}}{d\theta} + i_c \frac{dL_{cm}}{d\theta}) \tag{2.20}$$

This component is a function of the mutual inductance between each stator phase and the rotor, and is a *linear* function of the stator currents. In an ideal motor, the stator windings would be wound in an exact sinusoidal pattern making each mutual inductance term a pure sinusoidal function as given by,

$$L_{am} = L_m \cos(N_p\theta) \tag{2.21}$$

$$L_{bm} = L_m \cos(N_p\theta - \tfrac{2\pi}{3}) \tag{2.22}$$

$$L_{cm} = L_m \cos(N_p\theta - \tfrac{4\pi}{3}) \tag{2.23}$$

Note that the period of the inductance functions are dependent on the number of pole pairs N_p. Given this, the question of what current waveforms to impose on the stator remains. Assume that pure a sinusoidal excitation is chosen,

$$i_a = I_p \sin(N_p\theta) \tag{2.24}$$

$$i_b = I_p \sin(N_p\theta - \tfrac{2\pi}{3}) \tag{2.25}$$

$$i_c = I_p \sin(N_p\theta - \tfrac{4\pi}{3}) \tag{2.26}$$

Substituting Equations **(2.21)-(2.26)** into Equation **(2.20)** yields,

$$T_\mu = \frac{3}{2} N_p k_m L_m I_p \tag{2.27}$$

In this case, T_μ is linear with respect to the current amplitude I_p and constant with respect to rotor position θ (*i.e.* no torque ripple).

For *real* motors, the stator windings are only approximately sinusoidal causing the mutual inductance terms to contain higher harmonic terms. A square winding distribution(*i.e.* the worst case) results in a triangle inductance pattern with harmonics at all odd multiples of the fundamental pole frequency. Equations **(2.28)** through **(2.30)** give the Fourier series model for this distribution.

$$L_{am} = L_m \sum_{n=1}^{n\,odd} \frac{1}{n^2} \cos(nN_p\theta) \tag{2.28}$$

$$L_{bm} = L_m \sum_{n=1}^{n\,odd} \frac{1}{n^2} \cos(n(N_p\theta - \tfrac{2\pi}{3})) \tag{2.29}$$

$$L_{ac} = L_m \sum_{n=1}^{n\,odd} \frac{1}{n^2} \cos(n(N_p\theta - \tfrac{4\pi}{3})) \tag{2.30}$$

If the same sinusoidal excitation is applied in this case, the resulting mutual torque expression is not independent of the rotor position θ. To see this, assume that the mutual inductance terms contain the 3rd and 5th harmonics,

$$L_{am} = L_m \cos(N_p\theta) + \frac{1}{9}L_m \cos(3N_p\theta) + \frac{1}{25}L_m \cos(5N_p\theta) \quad (2.31)$$

$$L_{bm} = L_m \cos(N_p\theta - \frac{2\pi}{3}) + \frac{1}{9}L_m \cos(3(N_p\theta - \frac{2\pi}{3})) + \frac{1}{25}L_m \cos(5(N_p\theta - \frac{2\pi}{3})) \quad (2.32)$$

$$L_{cm} = L_m \cos(N_p\theta - \frac{4\pi}{3}) + \frac{1}{9}L_m \cos(3(N_p\theta - \frac{4\pi}{3})) + \frac{1}{25}L_m \cos(5(N_p\theta - \frac{4\pi}{3})) \quad (2.33)$$

Now apply the same stator current waveforms given by Equations **(2.24)**, **(2.25)**, and **(2.26)**. Substituting into Equation **(2.20)** yields the following expression for the mutual torque:

$$T_\mu = \frac{3}{2}N_p k_m L_m I_p - \frac{3}{10}N_p k_m L_m \cos(6N_p\theta) \quad (2.34)$$

The mutual torque T_μ is no longer independent of the rotor position θ. There is a sinusoidal component at six times the input frequency due to the interaction between the higher order inductance harmonic and the input stator currents. This interaction is one source of torque ripple. The natural question to ask now is "does there exist a different stator current waveform which will cause the mutual torque to again be independent of rotor position?". Provided the number of inductance harmonics is finite, the answer to this question is "yes". Again consider the case where the 3rd and 5th inductance harmonics are present(*i.e.* Equations **(2.31)**, **(2.32)**, and **(2.33)**). Assume the stator currents are the following,

$$i_a = I_p \sin(N_p\theta) - \frac{1}{5}I_p \sin(5N_p\theta) \quad (2.35)$$

$$i_b = I_p \sin(N_p\theta - \frac{2\pi}{3}) - \frac{1}{5}I_p \sin(5(N_p\theta - \frac{2\pi}{3})) \quad (2.36)$$

$$i_c = I_p \sin(N_p\theta - \frac{4\pi}{3}) - \frac{1}{5}I_p \sin(5(N_p\theta - \frac{4\pi}{3})) \quad (2.37)$$

Substituting these stator currents into Equation **(2.20)** yield the following mutual torque expression:

$$T_{\mu} = \frac{69}{50} N_p k_m L_m I_p \qquad (2.38)$$

For the augmented stator excitation, the mutual torque T_{μ} is once again independent of the rotor position(*i.e.* the torque ripple has been eliminated). This idea will be used as a basis for a minimum torque ripple control scheme. Although the actual system may contain a very large (possibly infinite) number of inductance harmonics, in practice the small relative amplitude of the higher order terms produce negligible contributions to the torque spectrum. Thus, significant torque ripple reduction can be achieved through the addition of a finite number of stator current harmonics.

The third and final component of the electrical torque is known as *cogging* or *detent* torque. The expression for this component is given by

$$T_c = k_m^2 \frac{dL_{mm}}{d\theta} \qquad (2.39)$$

T_c is due to interactions between the rotor permanent-magnets and the surrounding stator material. If the stator is not smooth, the rotor will *prefer* to align its magnets with the *teeth* of the stator. This preference creates a rotor position dependent force on the rotor which adds to the overall torque. The cogging torque is a function of motor construction parameters (*i.e.* the number of stator teeth, the number of rotor magnet poles, the stator/rotor gap width, and the power density of the rotor magnets) and not of applied stator current. Thus, T_c does not contribute any useful working torque and simply adds to the torque ripple. Motor construction techniques to reduce cogging torque such as rotor magnet skewing have been studied extensively in references [6], [7], [9], [11], [14], [16], [17], and [21]. Although the cogging forces can be significantly reduced, construction techniques alone can not completely eliminate cogging and result in a trade-off with overall power density. By adding appropriate harmonics to the stator current waveform, the effects of the cogging torque can be eliminated actively. This again assumes that the cogging torque harmonics to be eliminated are restricted to a finite frequency band. Analysis of the cogging forces in a dual air-gap axial-field

motor through both experiment[7] and finite-element modeling[6] suggest that the torque ripple spectrum including cogging torque effects is effectively band limited.

2.3 Axial Forces in Axial-Field Motors

Reference [6] provides a detailed analysis into the sources of torque ripple in axial-field PMAC motors. There are two components to torque ripple in axial-field type machines, tangential and axial. The *tangential* component is caused by stator/rotor interactions resulting in position dependent mutual and detent torque terms. This is the same torque ripple component found in radial-field motors which was described in Chapter 2.2. The *axial* component, which is only found in the axial-field configuration, is caused by differing flux paths on either side of the rotor. The resulting axial force is also rotor position dependent, and like tangential torque ripple, this force may excite mechanical vibrations in the drive shaft leading to unacceptable noise transmission. Therefore, it is necessary to simultaneously minimize both tangential *and* axial components of torque ripple.

The authors of reference[6] through finite-element analysis techniques found that *both* tangential and axial components of torque ripple are effected by staggering one stator relative to the other (**Figure 2.4**).

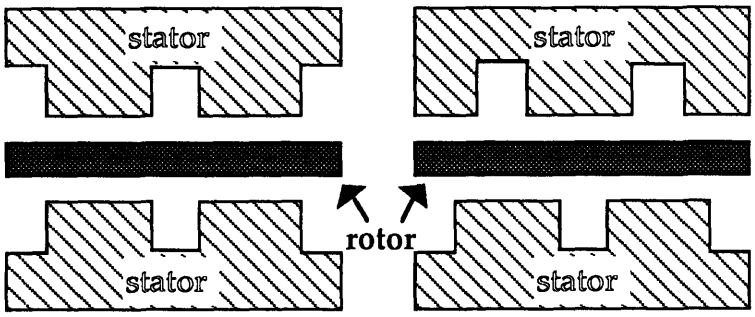

Figure 2.4: Unstaggered vs. Staggered Stators

Staggering the stators was found to greatly reduce the detent torque which resulted in smaller tangential torque ripple. However, staggering was found to cause much larger axial forces on the rotor. Additionally, it was found that axial forces are minimized when the stators are precisely aligned. Therefore, there is a trade-off between tangential and axial torque ripple components

when constructing a dual-stator axial-field motor. Both components can not be simultaneously minimized through construction techniques alone.

It is suggested in reference[6] that one choice is to build the motor with precisely aligned stators to minimize axial torque ripple and then use advanced control of the stator current waveforms to reduce the tangential torque ripple. It may be possible to minimize axial torque ripple through control of stator currents; however, this would required that separate current waveforms be applied to the two stators independently. Separate ports to the two stators are not usually provided making the latter suggestion impossible. Therefore, the active reduction of the tangential component of torque ripple only will be considered. It will be assumed from here on that the axial forces of the motor have been minimized through alignment of the two stators.

3 Active Torque Ripple Reduction Part I: Current Selection

It was shown in Chapter 2 that unavoidable parasitics in stator and rotor construction result in position dependent terms(*i.e.* torque ripple) when the stator excitation is a pure sinusoidal waveform. However, altering the stator excitation with harmonics at the appropriate frequency, amplitude, and phase can reduce the effect of the motor imperfections. The reduction of torque ripple through specific shaping of the stator excitation is termed *Active Torque Ripple Reduction* (ATRR).

Assuming current mode control of the stator excitation essentially removes the need to consider the stator or electrical dynamics when analyzing the mechanical motor variables, it is beneficial to think of ATRR as the active shaping of the stator *current* waveforms. Implicit in the current shaping is the application of the appropriate stator voltages to generate the desired currents. This separation of variables suggests that there are two parts to ATRR-- selection of the appropriate current excitation to minimize the torque ripple for the given motor at the given operating speed, and enforcement of the selected current excitation through the application of the appropriate stator voltages to force the current to *track* the commanded waveform. For many motors, including the dual air-gap axial-field PMAC motor considered here, there is a significant time-scale separation between the electrical and mechanical dynamics(*i.e.* the electrical time-constants are much shorter than the mechanical). As a result, the controllers for each section can be designed separately and independently of each other. The remainder of Chapter 3 will consider the current selection problem. The current enforcement problem will be studied in Chapter 4.

3.1 Harmonic System Analysis

In order to select the appropriate stator current waveform to minimize torque ripple, it is first necessary to understand how a change in the stator current waveform affects the electrical torque waveform. A detailed motor model including source of torque ripple was developed in Chapter 2, however the model in its present form does not provide the necessary insight

to develop a systematic methodology for selecting the appropriate current waveform. As demonstrated by the simple example in Section 2.2, the appropriate selection of current harmonics to cancel even a single inductance harmonic term required a *clever* guess for the form of the stator current. To solve the more general problem, a more precise analysis technique will be required.

The reduction of torque ripple essentially means reduction of the non DC terms in the frequency spectrum of the electrical torque waveform. The pure time domain model derived in Chapter 2 does not provide the necessary insight into the frequency response of the system. One method to gain this insight is to introduce a transformation of variables in which the state-variables of the transformed system represent the frequency content of the system's physical state-variables. Consider the following nonlinear system

$$\frac{d\mathbf{x}}{dt} = f(\mathbf{x},\mathbf{u}) \tag{3.1}$$

where $\mathbf{x}$ is the state-vector and $\mathbf{u}$ is the input vector, and whose state trajectories exhibit periodic oscillations around their ideal(*i.e.* desired) trajectories. Let the fundamental frequency of these periodic oscillations be ω and define the following variable transformation.

$$\mathbf{x}(t-T+s) = \sum_{n=-\infty}^{\infty} \mathbf{X}_n(t) e^{jn\omega(t-T+s)} \tag{3.2}$$

$$\mathbf{u}(t-T+s) = \sum_{n=-\infty}^{\infty} \mathbf{U}_n(t) e^{jn\omega(t-T+s)} \tag{3.3}$$

where $T = 2\pi/\omega$ and $s \in (0,T]$. This transformation is in effect a time-varying Fourier Series expansion over the interval (t-T,t]. This expansion was used in reference [25] for use in the analysis of resonant power converters. A similar analysis will be applied here to the periodic oscillations of a rotating electric machine. The only assumption which need hold true is that the state-variable oscillations be periodic with the same fundamental frequency ω, which is true for the PMAC motor application. The transformed state-vector $\mathbf{X}_k(t)$ and input-vector $\mathbf{U}_k(t)$ are complex functions of time. The original time functions $\mathbf{x}(t)$ and $\mathbf{u}(t)$ are real functions(*i.e.* a pure real number at each point in time)

which imposes the following constraints on the transformed state and input variables,

$$\mathbf{X}_{-n}(t) = \mathbf{X}_n^*(t) \qquad \forall n, t \tag{3.4}$$

$$\mathbf{U}_{-n}(t) = \mathbf{U}_n^*(t) \qquad \forall n, t \tag{3.5}$$

where $X^*(U^*)$ is the complex conjugate of X(U). In the steady-state, the transformed variables $\mathbf{X}_k(t)$ and $\mathbf{U}_k(t)$ simply become the standard Fourier Series coefficients $\mathbf{X}_k$ and $\mathbf{U}_k$,

$$\mathbf{x}(t) = \sum_{n=-\infty}^{\infty} \mathbf{X}_n e^{jn\omega t} \tag{3.6}$$

$$\mathbf{u}(t) = \sum_{n=-\infty}^{\infty} \mathbf{U}_n e^{jn\omega t} \tag{3.7}$$

of the physical variables.

In many control schemes for rotating electrical machines, the control inputs are computed as functions of the rotor position θ instead of time. This approach is used because most state-variables in a rotating machine are periodic in θ with period 2π, and θ is a measurable quantity. The transformation of variables defined above can be modified to

$$\mathbf{x}(\theta) = \sum_{n=-\infty}^{\infty} \mathbf{X}_n(t) e^{jn\theta} \tag{3.8}$$

$$\mathbf{u}(\theta) = \sum_{n=-\infty}^{\infty} \mathbf{U}_n(t) e^{jn\theta} \tag{3.9}$$

In the steady-state, the rotor position θ is proportional to time(*i.e.* $\theta=\omega t$). Thus, the modified Equations **(3.8)** and **(3.9)** revert back to the original transformation given by Equations **(3.6)** and **(3.7)** in steady-state operation. The physical variables $\mathbf{x}(\theta)$ and $\mathbf{u}(\theta)$ are functions of position θ, but the Fourier coefficients $\mathbf{X}_n(t)$ and $\mathbf{U}_n(t)$ in equations **(3.8)** and **(3.9)** are still functions of time. This implies that the control algorithm which will compute the appropriate $\mathbf{U}_n$ will be based on time. It is interesting to note that these Fourier coefficients could be taken to be functions of rotor position as

well(*i.e.* $\mathbf{X}_n(\theta)$ and $\mathbf{U}_n(\theta)$), leading to a completely time independent controller.

The transformation of variables given by Equations **(3.8)** and **(3.9)** provides the type of system decomposition needed for the ATRR problem. Note however that this transformation increases the order of the plant to infinity. Even a simple first order system will require an infinite number of state-variables in the transformed state-space. For the PMAC motor application and most *real* systems, the bulk of the energy associated with the state oscillations reside appears in a limited frequency band. For PMAC motors, the torque ripple energy is concentrated around the fundamental pole frequency of the machine. Thus, the number of Fourier coefficients required by the transformed system can be reduced by limiting frequency band of oscillations which will be considered. In this case, the transformation defined by Equations **(3.8)** and **(3.9)** changes to

$$\mathbf{x}(\theta) = \sum_{n=-N}^{N} \mathbf{X}_n(t) e^{jn\theta} \tag{3.10}$$

$$\mathbf{u}(\theta) = \sum_{n=-N}^{N} \mathbf{U}_n(t) e^{jn\theta} \tag{3.11}$$

which limits the order of the transformed system to 2N(*i.e.* the sum of the upper and lower summation limits from Equations **(3.10)** and **(3.11)**) and the highest considered oscillation frequency component to N times the rotor's rotational frequency ω.

A second modeling problem exists with the transformation defined above. Consider the state of the system at time zero(*i.e.* t=0 and θ=0),

$$\mathbf{x}(0) = \mathbf{X}_{-N}(0)+\ldots+\mathbf{X}_{-1}(0) + \mathbf{X}_0(0) + \mathbf{X}_1(0)+\ldots+\mathbf{X}_N(0) \tag{3.12}$$

The initial state vector is easily converted to the transformed state-space, however, the mapping of the initial conditions to the new space is under-constrained. This problem of mapping initial conditions through a variable transformation is termed the *initial condition problem*. In general, the initial condition problem may be over-constrained, one-to-one, or under-constrained. In the under-constrained case, as in the PMAC motor

application, the problem becomes choosing the appropriate starting point to best represent the behavior of the physical system.

For a general system, the initial condition problem is non-trivial and does not have a specific solution. However, for the synchronous motor application, there is a solution which is better than the others. For an *ideal* sinusoidal wound motor, the electrical states of the system(*i.e.* the stator currents) are pure sinusoidal waveforms with the stator pole frequency(*i.e.* $N_p\omega$). Thus, one way to map the initial conditions on the electrical state-variables is to set the N_p component equal to the given initial state with all other frequency components set to zero. This idea could be extended to an ideal square wound machine by setting the initial conditions at the frequency components of the ideal input square wave currents. Also, in an ideal motor, the rotor speed ω will have only a DC component in the steady-state(*i.e.* no ripple). Thus, it would make sense to map any initial rotor speed solely to its DC component in the transformed system. The second mechanical state, the rotor position θ, can be chosen to be zero initially. To summarize,

$$\mathbf{x}(0) = \mathbf{X}_0(0) + \mathbf{X}_{N_p}(0) \tag{3.13}$$

$$\begin{bmatrix} i_0 \\ \omega_0 \\ \theta_0 \end{bmatrix} = \begin{bmatrix} 0 \\ \omega_0 \\ 0 \end{bmatrix}_0 + \begin{bmatrix} i_0 \\ 0 \\ 0 \end{bmatrix}_{N_p} \tag{3.14}$$

where i_0, ω_0, θ_0 are the initial stator currents, rotor speed, and rotor position respectfully. In essence, the system is modeled as an ideal PMAC motor which is periodically disturbed by a secondary system causing the parasitic oscillations at the overall system output(**Figure 3.1**).

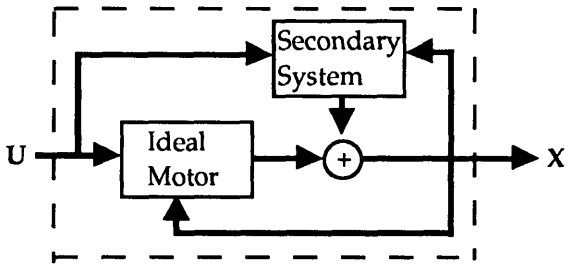

Figure 3.1: TransformedSystem Block Diagram

The initial conditions of the secondary system are assumed to be zero for modeling convenience which is justified provided the contribution of secondary system is much smaller than the ideal component(*i.e.* the motor is constructed well).

3.2 Harmonic Analysis of PMAC Motor

Using the background previously developed, the variable transformation given by Equations **(3.8)** and **(3.9)** can be applied to the time domain state-space model for the PMAC motor developed in Chapter 2. The current control inner-loop that will be used to enforce the appropriate current waveform will be detailed in Chapter 4. Thus, it is justified at this level to consider the stator currents(*i.e.* i_a, i_b, and i_c) as the control inputs, ignoring any stator electrical dynamics. It is necessary to choose current waveforms with enough degrees of freedom to eliminate torque ripple due to both inductance and cogging harmonics. The following choice provides the needed freedom.

$$i_a(\theta) = \sum_{m=-N}^{N} \sum_{n=-N}^{N} I_{m,n} e^{jnN_p\theta} \tag{3.15}$$

$$i_b(\theta) = \sum_{m=-N}^{N} \sum_{n=-N}^{N} I_{m,n} e^{j(nN_p\theta - m\frac{2\pi}{3})} \tag{3.16}$$

$$i_c(\theta) = \sum_{m=-N}^{N} \sum_{n=-N}^{N} I_{m,n} e^{j(nN_p\theta - m\frac{4\pi}{3})} \tag{3.17}$$

where the $I_{m,n}$'s are the new control variables. In the steady-state, $I_{m,n}$ represents the complex amplitude of the n^{th} stator current harmonic with phase offset multiple m where the fundamental frequency is the rotor's pole frequency, N_p. The reasoning behind this choice of current excitation will be discussed further in this section.

The load torque Equation **(2.10)** of the motor also needs to be transformed to the harmonic state-space since it is the load harmonic terms which need to be attenuated. Applying the variable transformation,

$$T_L(\theta) = \sum_{n=-2N}^{2N} T_n e^{jnN_p\theta} \tag{3.18}$$

where T_n is the complex amplitude of the n^{th} torque ripple harmonic. The summation limits in Equation **(3.18)** are correctly written as 2N (not N). It will be shown shortly that N mutual inductance harmonics interacting with N current harmonics can result in 2N torque harmonics.

The next step is to apply the harmonic variable transformation to the mutual inductance parameters of the motor as defined in Section 2.1(*i.e.* L_{am}, L_{bm}, and L_{cm}).

$$L_{am}(\theta) = \sum_{n=-N}^{N} L_n e^{jnN_p\theta} \tag{3.19}$$

$$L_{bm}(\theta) = \sum_{n=-N}^{N} L_n e^{jn(N_p\theta - \frac{2\pi}{3})} \tag{3.20}$$

$$L_{cm}(\theta) = \sum_{n=-N}^{N} L_n e^{jn(N_p\theta - \frac{4\pi}{3})} \tag{3.21}$$

L_n represents the complex amplitude for the n^{th} inductance harmonic. For the ideal motor, the inductance terms will be pure sinusoids at the stator pole frequency, *i.e.*

$$L_n = \begin{cases} L_m & n = 1 \\ 0 & \text{else} \end{cases} \tag{3.22}$$

For *real* motors, the inductance terms will contain higher order harmonics which is one source of torque ripple, as mentioned in Section 2.2. In the worst case, all odd harmonics will be present with amplitudes decreasing inversely as the harmonic squared, *i.e.*

$$L_n = \begin{cases} \frac{L_m}{n^2} & n \text{ odd} \\ 0 & \text{else} \end{cases} \tag{3.23}$$

For symmetry reasons, it will be assumed here that the harmonic content is the same for each phase(*i.e.* L_n is the same for L_{am}, L_{bm}, and L_{cm}). The variable transformation can also be applied to the cogging term L_{mm},

$$L_{mm}(\theta) = \sum_{n=-2N}^{2N} C_n e^{jnN_p\theta} \tag{3.24}$$

where C_n is the complex amplitude of the n^{th} cogging harmonic. Keeping with the symmetry assumption, the cogging is modeled as three equal components, each contributing to a single stator phase. The fundamental cogging harmonic will appear as the product of the stator and rotor pole frequencies. It is assumed here for simplicity that the stator and rotor pole frequencies are equal, however this is not required to perform this analysis. The higher order cogging harmonics will be a function of the motor's construction(teeth width, skewing angle, etc.) and may be estimated for a specific motor either through experimental methods or finite element numerical analysis techniques, see references [6] and [7].

Using the above computations, we can find the form of the electrical torque, Equation **(2.17)**, in the transformed state-space. Since the electrical torque is a function of the derivatives of the inductance functions, the first step is to take the derivatives of Equations **(3.19)**, **(3.20)**, **(3.21)**, and **(3.24)** with respect to θ.

$$\frac{dL_{am}}{d\theta} = \sum_{n=-N}^{N} jnN_p L_n e^{jnN_p\theta} \tag{3.25}$$

$$\frac{dL_{bm}}{d\theta} = \sum_{n=-N}^{N} jnN_p L_n e^{jn(N_p\theta - \frac{2\pi}{3})} \tag{3.26}$$

$$\frac{dL_{cm}}{d\theta} = \sum_{n=-N}^{N} jnN_p L_n e^{jn(N_p\theta - \frac{4\pi}{3})} \tag{3.27}$$

$$\frac{dL_{mm}}{d\theta} = \sum_{n=-2N}^{2N} jnN_p C_n e^{jnN_p\theta} \tag{3.28}$$

Substituting the stator currents, Equations **(3.15)**, **(3.16)**, and **(3.17)**, and the mutual inductance derivatives, Equations **(3.25)**, **(3.26)**, and **(3.27)**, into the mutual torque expression, Equation **(2.20)**.

$$\begin{aligned} T_\mu(\theta) = k_m &\left(\sum_{m=-N}^{N} \sum_{n=-N}^{N} I_{m,n} e^{jnN_p\theta} \right) \left(\sum_{q=-N}^{N} jqN_p L_q e^{jqN_p\theta} \right) \\ +k_m &\left(\sum_{m=-N}^{N} \sum_{n=-N}^{N} I_{m,n} e^{j(nN_p\theta - m\frac{2\pi}{3})} \right) \left(\sum_{q=-N}^{N} jqN_p L_q e^{jq(N_p\theta - \frac{2\pi}{3})} \right) \\ +k_m &\left(\sum_{m=-N}^{N} \sum_{n=-N}^{N} I_{m,n} e^{j(nN_p\theta - m\frac{4\pi}{3})} \right) \left(\sum_{q=-N}^{N} jqN_p L_q e^{jq(N_p\theta - \frac{4\pi}{3})} \right) \end{aligned} \tag{3.29}$$

This expression can be simplified by replacing the summation of summations terms by double summations.

$$T_\mu(\theta) = k_m \sum_{m=-N}^{N} \sum_{n=-N}^{N} \sum_{q=-N}^{N} jqN_p L_q I_{m,n} e^{j(n+q)N_p\theta} (1 + e^{-j(m+n)\frac{2\pi}{3}} + e^{-j(m+n)\frac{4\pi}{3}}) \tag{3.30}$$

A closer look at Equation **(3.30)**, reveals that the mutual torque is simply a weighted convolution sum of the current and inductance harmonics. Notice from Equation **(3.31)** that the mutual torque harmonics are zero except when m+n is a multiple of three. The choice of n selects the frequency of the rotating magnetic stator field in the motor. The rotational frequency of the stator magnetic field is equal to $nN_p\omega$. The choice of m selects the direction of the rotating magnetic field. Choosing m to be in the set {1, 4, 7, ...} results in a positive rotating magnet stator field. Choosing m to be in the set {2, 5, 8, ...} results in a negative multiple of three results in a negative rotating stator field. Thus, this choice of input currents (*i.e.* Equations **(3.15)**, **(3.16)**, and **(3.17)**) generates a linear combination of both positive and negative rotating fields at any desired frequency. By choosing the appropriate set of (m,n) [under the constraint that m+n is a multiple of three], it should be possible to generate rotating field components which cancel the rotating fields due to the parasitic inductance and cogging effects. This will result in torque ripple reduction.

Consider again the current waveforms, Equations **(3.15)**, **(3.16)**, and **(3.17)**. Notice that, under the constraint that m+n is a multiple of three, these three-phase currents sum to zero for all θ, *i.e.*

$$i_a(\theta)+i_b(\theta)+i_c(\theta)=0 \qquad \forall\theta \tag{3.31}$$

Thus, this choice of current excitation may be applied to the Y-connected motor configurations. A four wire or isolated winding configuration is not required.

Substituting the cogging inductance derivative, Equation **(3.28)**, into the cogging torque expression, Equation **(2.39)**, yields

$$T_c(\theta)=k_m^2\sum_{n=-2N}^{2N} jnN_pC_ne^{jnN_p\theta} \tag{3.32}$$

The sum of the mutual torque, Equation **(3.30)**, and the cogging, Equation **(3.32)**, is the total torque of electrical origin. In the steady-state, the total electrical torque must equal the load torque, *i.e.*

$$T_t(\theta)=T_\mu(\theta)+T_c(\theta)=T_L(\theta) \tag{3.33}$$

Using the above results, the complete torque balance equations in the harmonic state-space become

$$\begin{aligned} &k_m\sum_{m=-N}^{N}\sum_{n=-N}^{N}\sum_{q=-N}^{N} jqN_pL_qI_{m,n}e^{j(n+q)N_p\theta}\left(1+e^{-j(m+n)\frac{2\pi}{3}}+e^{-j(m+n)\frac{4\pi}{3}}\right) \\ &+k_m^2\sum_{n=-2N}^{2N} jnN_pC_ne^{jnN_p\theta}=\sum_{n=-2N}^{2N}T_ne^{jN_p\theta} \end{aligned} \tag{3.34}$$

This equations contains a large quantity of information. It shows how the inductance, current, and cogging harmonics combine to create torque harmonics. In addition, Equation **(3.34)** shows explicitly how to compute the complex weighting factors which when combined determine the magnitude and phase of the torque ripple.

To gain further insight, the torque balance relation, Equation **(3.34)**, can be written in a matrix form.

$$LI + C = T \tag{3.35}$$

where L, I, C, and T take on the following forms.

$$L = \begin{bmatrix} \dots & n+q=0 & \dots \\ \dots & n+q=1 & \dots \\ \dots & n+q=2 & \dots \\ \dots & \dots & \dots \\ \dots & n+q=2N & \dots \end{bmatrix} \tag{3.36}$$

$$I = \begin{bmatrix} I_{-N,-N} \\ \dots \\ I_{-m,-n} \\ \dots \\ I_{m,n} \\ \dots \\ I_{N,N} \end{bmatrix} \quad \begin{cases} -N \le m \le N \\ -N \le n \le N \\ m+n \text{ is a a multiple of 3.} \end{cases} \tag{3.37}$$

$$C = \begin{bmatrix} 0 \\ C_1 \\ \dots \\ C_{2N} \end{bmatrix} \tag{3.38}$$

$$T = \begin{bmatrix} T_0 \\ T_1 \\ \dots \\ T_{2N} \end{bmatrix} \tag{3.39}$$

The dimension of L is 2N+1 by $(2N)^2/3$, I is $(2N)^2/3$ by 1, C is 2N+1 by 1, and T is 2N+1 by 1, thus Equation **(3.35)** is dimensionally correct. Notice that N current harmonics and N mutual inductance harmonics can produce 2N torque harmonics. This is due to the convolution relationships, and in general, the total number of torque harmonics will be the sum of the number of current harmonics and mutual inductance harmonics. Since m+n needs to be a multiple of three to produce an effect on the torque harmonics(see Equation **(3.34)**), current harmonics in which m+n is not a multiple of three should be set to zero. They do not contribute to torque ripple reduction and result in resistive losses. As such, N should be chosen to be a multiple of 3 to insure that $I_{-N,-N}$ and $I_{N,N}$ (i.e. the first and last terms in Equation **(3.37)**) effect torque ripple.

If the mutual inductance matrix L and the cogging spectrum C for a motor is known precisely, the minimum torque ripple current excitation can be computed by solving the linear system of equations(*i.e.* Equation **(3.35)**). The mutual inductance L will contain more columns than rows for any choice of N (integer). Therefore, the system of equations is under-constrained (*i.e.* there exists many current vector I which satisfy the matrix equation). We

are free to choose any solution we wish. It makes sense to choose the solution which minimizes the I^2R losses in the motor windings, and thus, maximizes efficiency. Minimizing I^2R losses is equivalent to minimizing the norm of the vector I (see reference [3]). The minimum norm solution of Equation **(3.35)** is given by the following,

$$I = (L^* L)^{-1} L^* (u - C) \tag{3.40}$$

where L^* is the complex conjugate of the matrix L and u contains the Fourier coefficients of the *desired* torque spectrum.

$$u = \begin{bmatrix} T_0 \\ T_1 \\ \cdots \\ T_n \end{bmatrix} \tag{3.41}$$

To eliminate torque ripple, the commanded torque spectrum should only contain a DC component, *i.e.*

$$u = \begin{bmatrix} T_0 \\ 0 \\ \cdots \\ 0 \end{bmatrix} \tag{3.42}$$

where T_0 is the commanded torque which may be set by an outer speed control loop.

The above discussion shows the value of using this harmonic decomposition analysis. Given a motor's mutual inductance and cogging coefficients, the L matrix and C vector can be computed, and the optimal current coefficients I to eliminate torque ripple can be found. Unfortunately, this is not the end of the problem. The inductance and cogging parameters are not easily measurable off-line. In addition, they may change slightly over the operational life-time of the motor. Therefore, a fixed implementation of Equation **(3.40)** does not constitute a reliable solution to the problem. An adaptive control approach which uses Equation **(3.40)** as a basis and provides a more robust solution will be presented in Section 3.3.

3.3 Minimum Torque Ripple Current Controller

The analysis in Section 3.2 provides insight into the source of tangential torque in PMAC motors. It shows that torque harmonics can, theoretically, be controlled (or eliminated) through the careful addition of harmonic terms to the stator current waveforms. Equation **(3.40)** shows how to compute the amplitude and phase of the required current harmonics to impose a desired torque spectrum with maximum efficiency. This computation requires explicit knowledge of motor parameters(*i.e.* the matrices **L** and **C**). Unfortunately, the control calculation is sensitive to errors in these parameters. To use this control scheme in a practical motor drive, it would necessary to correct for these errors. One method for dealing with the sensitivity issue is to use *adaptive control.*

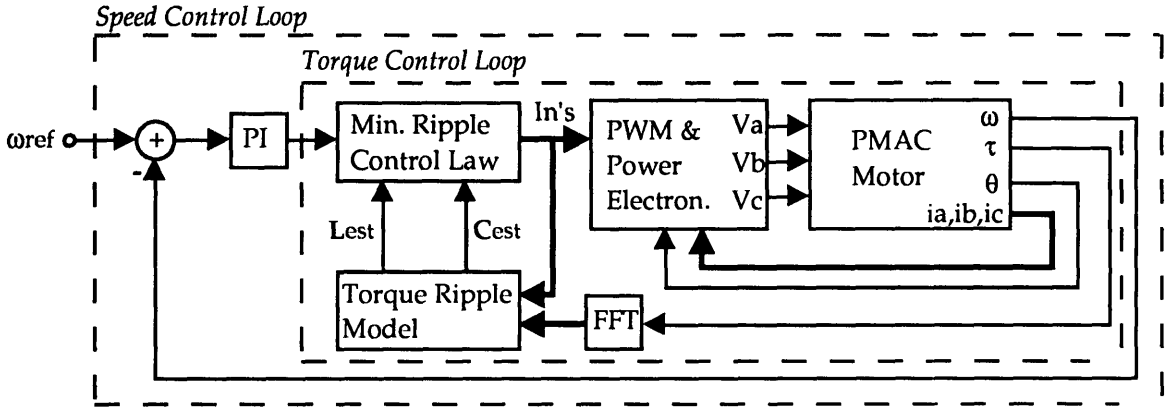

Figure 3.2: Controller Block Diagram

Figure 3.2 shows a *Model Reference Adaptive System* (MRAS)[28]. The control system is composed of two loops. The outer speed loop controls the commanded torque to regulate the shaft's rotational speed. The inner torque loop controls the applied current waveform to impose the desired working torque without ripple harmonics. The essential idea of the torque control loop is to use measurements of the torque ripple spectrum to recursively estimate the inductance and cogging harmonic terms(*i.e.* **L** and **C** from Equation **(3.40)**). The estimates of these parameters will be referred to as $\mathbf{L}_{est}$ and $\mathbf{C}_{est}$. Using these estimates, the appropriate current harmonics required to impose the desired DC torque with minimal ripple terms can be computed.

The first step to implementing the MRAS system shown in **Figure 3.2** is to derive an parameter estimation process. The model given by Equation **(3.34)** provides the necessary basis. It is a given that the cogging torque can not have a DC component(*i.e.* C_0=0). Therefore, it is guaranteed that the DC equation of **(3.34)** is can be written as the inner product of vectors containing the mutual inductance and current coefficients, *i.e.*

$$T_0 = \begin{bmatrix} I_{-N,-N} & \cdots & I_{0,0} & \cdots & I_{N,N} \end{bmatrix} \begin{bmatrix} L_N \\ \cdots \\ L_0 \\ \cdots \\ L_{-N} \end{bmatrix} \tag{3.43}$$

Given that the DC inductance component L_0 must also be zero, and all other Fourier coefficients must appear as complex conjugates, Equation **(3.43)** can be reduced to

$$\frac{T_0}{2} = \begin{bmatrix} I_{-N,-N} & \cdots & I_{1,-1} \end{bmatrix} \begin{bmatrix} L_N \\ \cdots \\ L_1 \end{bmatrix} \tag{3.44}$$

Since Equation **(3.44)** is linear, it is possible to apply least-squares (LS) techniques[28] to provide estimates of the inductance parameters given measurements of the DC torque which can be computed from a shaft speed measurement(see Equation **(2.28)**). To describe the LS update law, it is first necessary to define the following quantities:

$$\theta(t) = \begin{bmatrix} L_N \\ \cdots \\ L_1 \end{bmatrix} \tag{3.45}$$

$$\varphi(t) = \begin{bmatrix} I_{-N,-N} \\ \cdots \\ I_{1,-1} \end{bmatrix} \tag{3.46}$$

$$y(t) = \frac{T_0}{2} \tag{3.47}$$

where t is an index representing the current time step. One method for recursively computing a least-squares parameter estimate is Kaczmarz's algorithm[28]. Using the parameter definitions given by Equations **(3.45)**, **(3.46)**, and **(3.47)**, an estimate of the inductance parameters $\theta(t)$ may be computed as follows

$$\theta(t) = \theta(t-1) + \frac{\gamma\varphi}{\alpha + \varphi^T\varphi}[y(t) - \varphi^T\theta(t-1)] \tag{3.48}$$

where $\theta(t)$ is the best least-squares estimate of the inductance parameters given the previous estimate $\theta(t-1)$ and the most recent output measurement $y(t)$. Motor back EMF measurements may be used to provide an initial parameter estimate θ_0 which assumes no parasitic inductance harmonics,

$$\theta_0 = \begin{bmatrix} 0 \\ \cdots \\ 0 \\ L_1 \end{bmatrix} \tag{3.49}$$

where,

$$L_1 = \frac{E_b}{N_p} \tag{3.50}$$

If back EMF data is not available, the estimate may be initialized to zero. The later case will result in a slower parameter convergence. The variables α and γ in Equation **(3.48)** are estimator design parameters. α should be a small positive number whose purpose is to prevent the estimate from diverging when the input vector φ becomes very small. γ is the estimator's gain whose value represents a trade-off between convergence rate and stability. A large gain will result in fast parameter convergence, however, for a large enough gain the estimator will become unstable. As indicated in reference[28], the gain should be chosen between 0 and a maximum of 2 to prevent instability.

The Kaczmarz algorithm is a good estimator choice for motor drive applications due to its simplicity of implementation and speed of computation. Both are important constraints in motor drive implementations. Other least-square algorithms, such as Gauss[28], boast faster convergence rates, however at the expense of greater computational complexity.

One caution should be mention concerning the use of any recursive least-squares algorithm. In order to estimate a system parameter from the output measurements, it is necessary that the mode associated with that system parameter is excited by the input and observable in the output. This constraint is called the *Excitation Condition*. For the Kaczmarz estimator described above, the excitation condition can be described as follows. Define the matrix Φ such that,

$$\Phi = \varphi\varphi^T \tag{3.51}$$

where φ was defined in Equation **(3.46)**. The excitation condition is satisfied provided the matrix Φ has full rank. This result has an physically intuitive interpretation for the motor application. Considering Equation **(3.44)**, the DC electrical torque component is the result of each inductance harmonic multiplied by its corresponding current harmonic. To estimate the n^{th} inductance harmonic L_n, the input current waveform must include the n^{th} current harmonic I_n. To make sure that all desired inductance harmonics are present in the output, it is recommended that all current harmonics be initialized to some non-zero quantity. This is equivalent to forcing the input matrix(*i.e.* Equation **(3.51)**) to have full rank.

Given the parameter estimate $\theta(t)$, the inductance matrix estimate, L_{est}, can be constructed and used to estimate the cogging spectrum C_{est}.

$$C_{est} = T - L_{est}I \tag{3.52}$$

With the inductance and cogging harmonic estimates, L_{est} and C_{est}, the current control law which results in minimum torque ripple can be defined as follows.

$$I = (L_{est}^* L_{est})^{-1} L_{est}^* (u - C_{est}) \tag{3.53}$$

One beneficial feature of the MRAS system shown in **Figure 3.2** is that the inner torque control loop may be considered as transparent to the outer speed loop. Thus, the gains of the speed tracking PI compensator may be designed independent of the inner current control law.

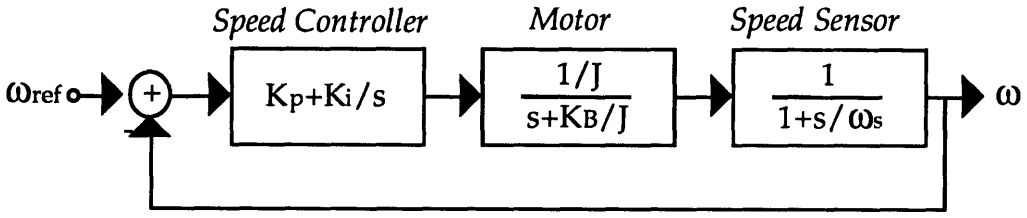

Figure 3.3: Speed Controller Transfer Function Diagram

where J and K_B are the moment of inertia and load damping coefficient for the motor and propulsor respectively, K_p and K_i are the speed controller gains, ω_s is the 3 dB bandwidth of the speed sensor. Using **Figure 3.3**, the speed input-output transfer function can be derived.

$$\frac{\omega}{\omega_{ref}} = \frac{1}{J} \frac{K_p s + K_i}{s(s + \frac{K_B}{J})(\frac{s}{\omega_s} + 1)} \tag{3.54}$$

Thus, the poles and zeros of the motor's speed dynamics are simply functions the motor's parameters, speed loop controller gains, and speed sensor characteristics. They do not influence torque ripple with the given setup.

The power electronics and FFT subsystems will be discussed further in Chapters 4 and 5 respectively. The next section will provide some computer simulation results of the parameter estimate and current control law subsystems.

3.4 Harmonic System Simulation & Parameter Estimation

The following computer simulations of the motor model and controller described above were constructed using SIMULINK[29]. They are intended to show the validity of the torque ripple model developed in Section 3.2 and demonstrate the performance of the parameter estimator developed in Section 3.3. This simulation deals only with the transformed Fourier state-variables as they are defined by Equations **(3.15)** through **(3.21)**. A more detailed simulation which is based on the motor's physical state-variables will be presented in Chapter 6.

Torque Constant	k0	0.4	NM/A
Cogging Coefficient	Lmm	0.1	H
Max Current Amplitude	Imax	150	A
Moment of Inertia	J	0.2	kg m^2
Damping Coefficient	Bω	0.1	NM/RPM^2
Number of Pole Pairs	Np	24	

Table 3.1: Simulation Parameters

Nominal parameters for a dual stator axial-field PMAC motor were used and are shown in **Table 3.1**[6]. **Graph 3.1** shows the rotor's velocity profile. In this test, the motor was given a 100 RPM step velocity command from rest. As shown, the rotor responded with a slightly under-damped response, a 2 second rise time, and zero steady-state error. As noted previously, the rotor's response is dictated completely by the choice of gains for the outer speed control loop(see **Figure 3.3**) and is does not affect torque ripple.

Graphs 3.2 through **3.7** show the magnitude and phase of the first 6 harmonics of the resulting torque ripple. Only the initial adaptation phase (*i.e.* open-loop system) is demonstrated here.

Graph 3.8 shows the applied current harmonics to the system during this initial adaptation phase. It should be noted that since only the first 6 torque harmonics are considered here, it is necessary to applied up to the third current harmonic.

Graphs 3.9 and **3.10** shows the computed estimates of inductance and cogging harmonics, respectively. The real values are shown as dashed lines on these graphs. As expected, each estimate converged in the steady-state to the true parameter value.

Graph 3.1: Rotor Velocity Profile

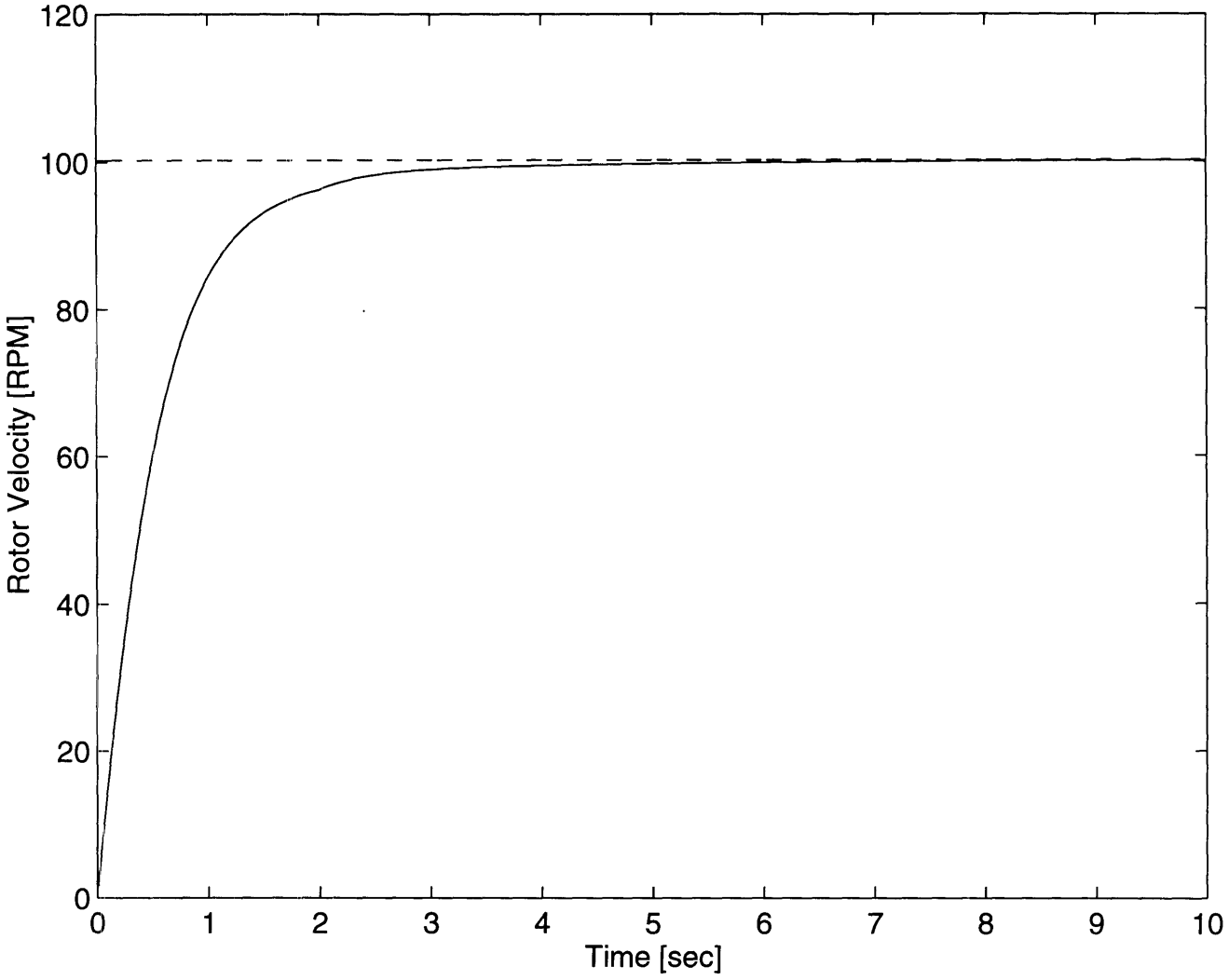

Graph 3.2: 1st Torque Ripple Harmonic, Magnitude and Phase

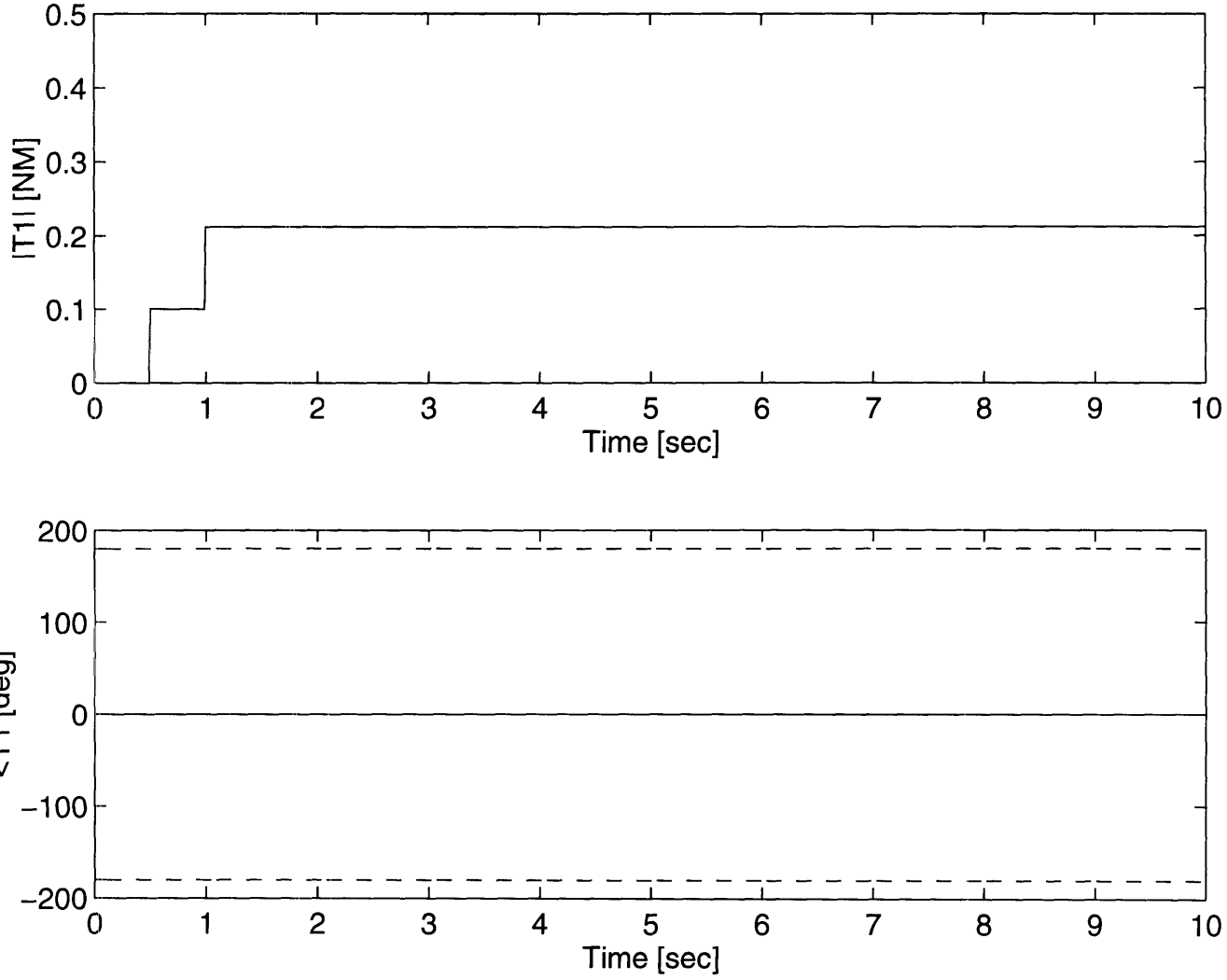

Graph 3.3: 2nd Torque Ripple Harmonic, Magnitude and Phase

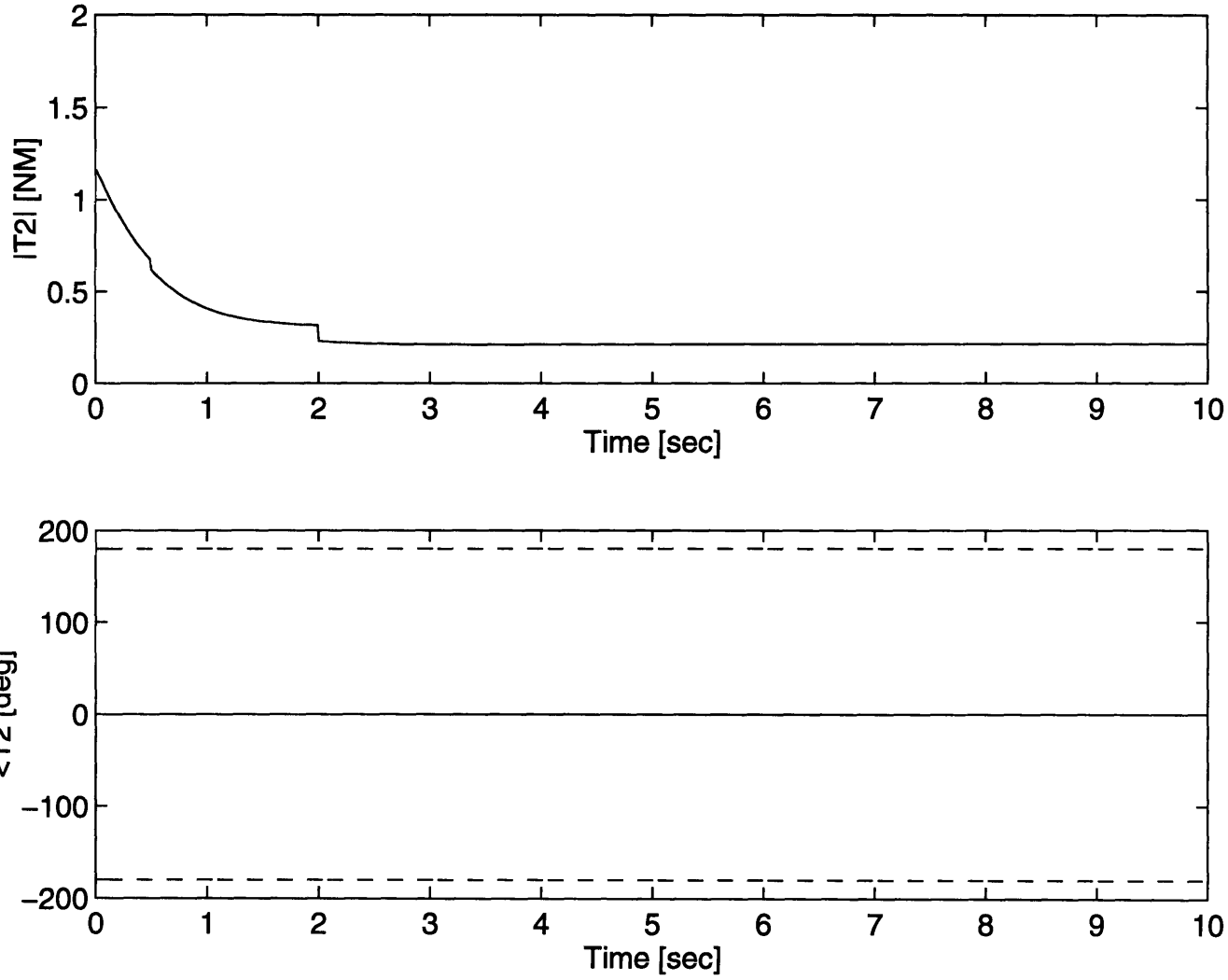

Graph 3.4: 3rd Torque Ripple Harmonic, Magnitude and Phase

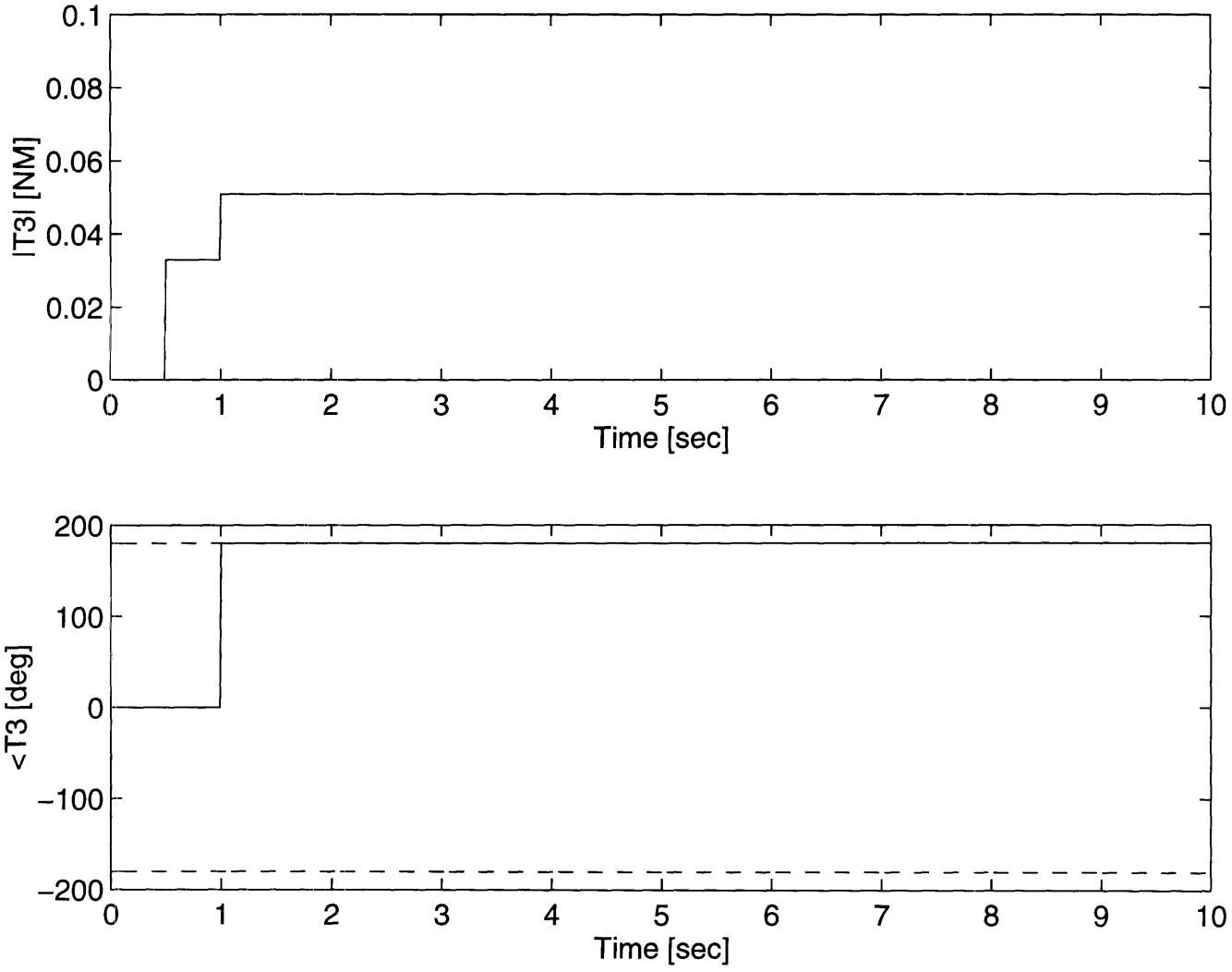

Graph 3.5: 4th Torque Ripple Harmonic, Magnitude and Phase

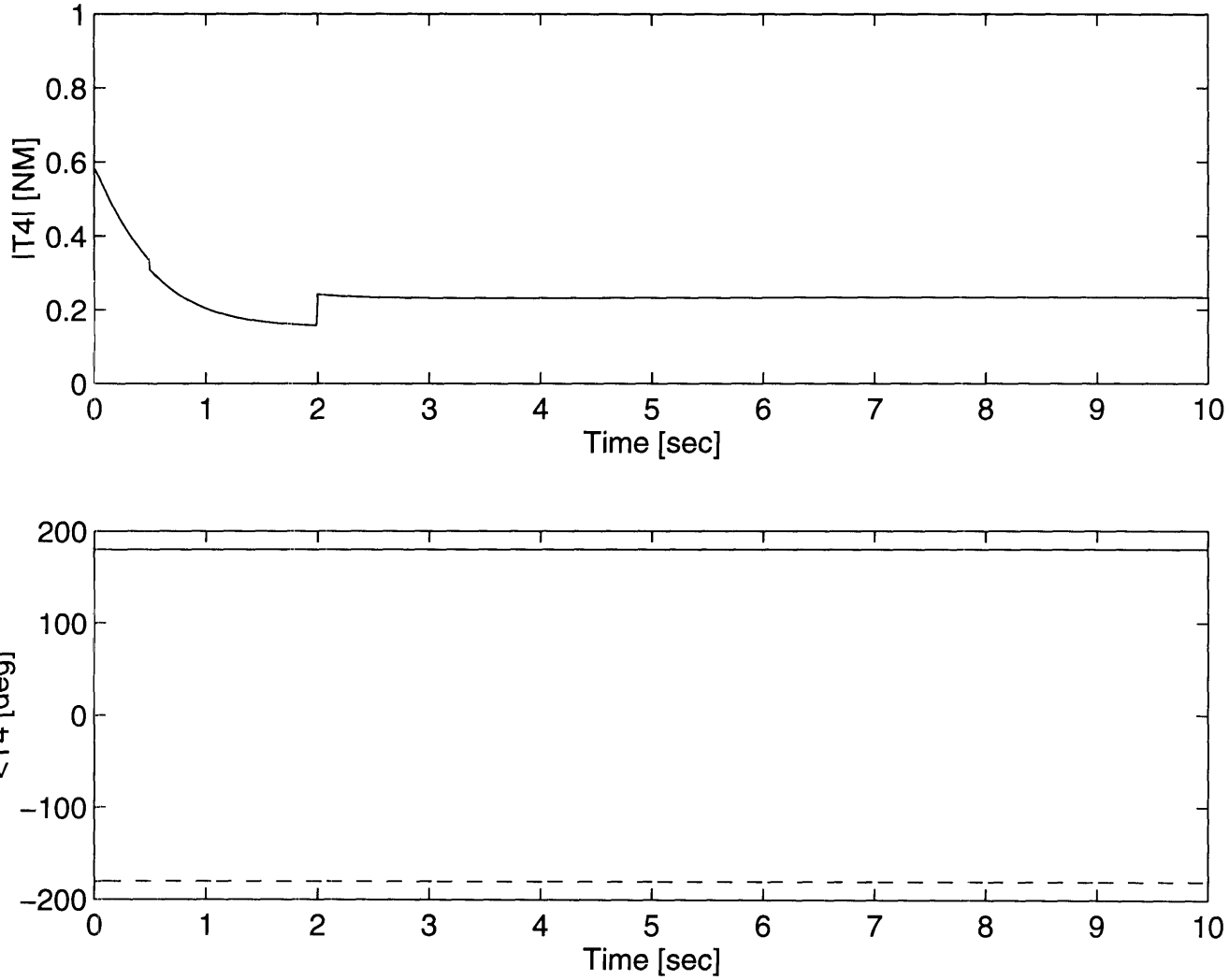

Graph 3.6: 5th Torque Ripple Harmonic, Magnitude and Phase

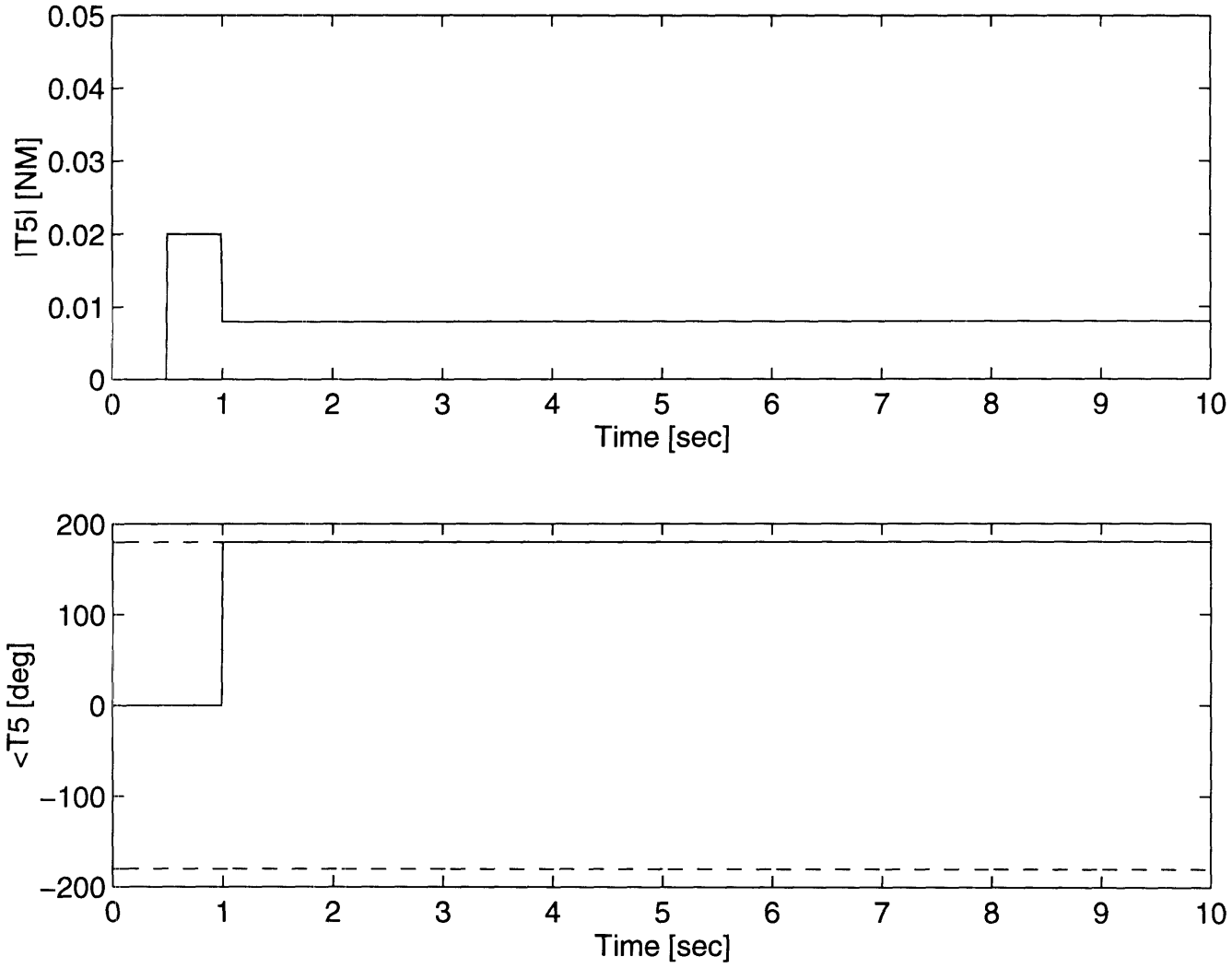

Graph 3.7: 6th Torque Ripple Harmonic, Magnitude and Phase

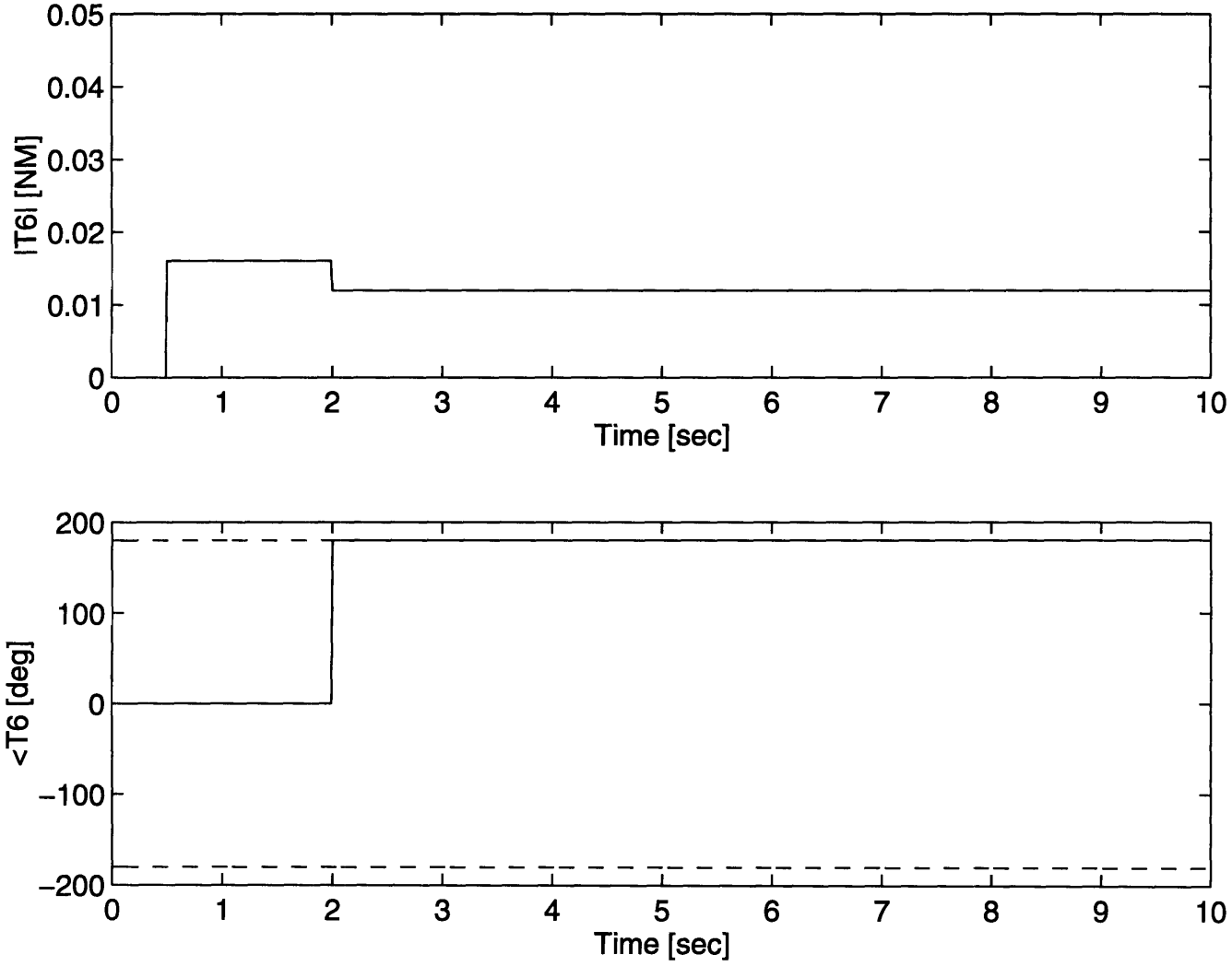

Graph 3.8: Applied Current Harmonics, Magnitudes Only

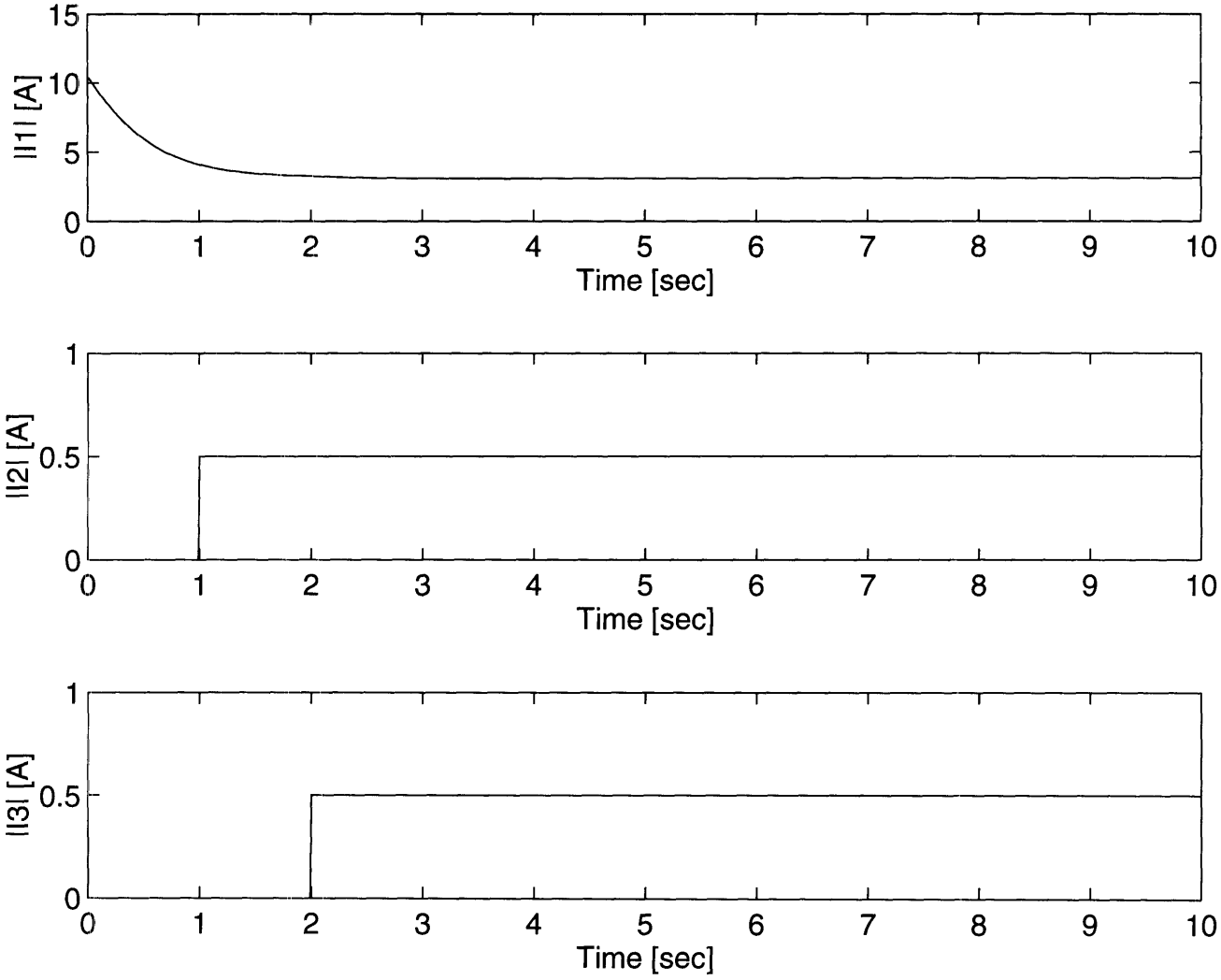

Graph 3.9: Inductance Spectral Estimation

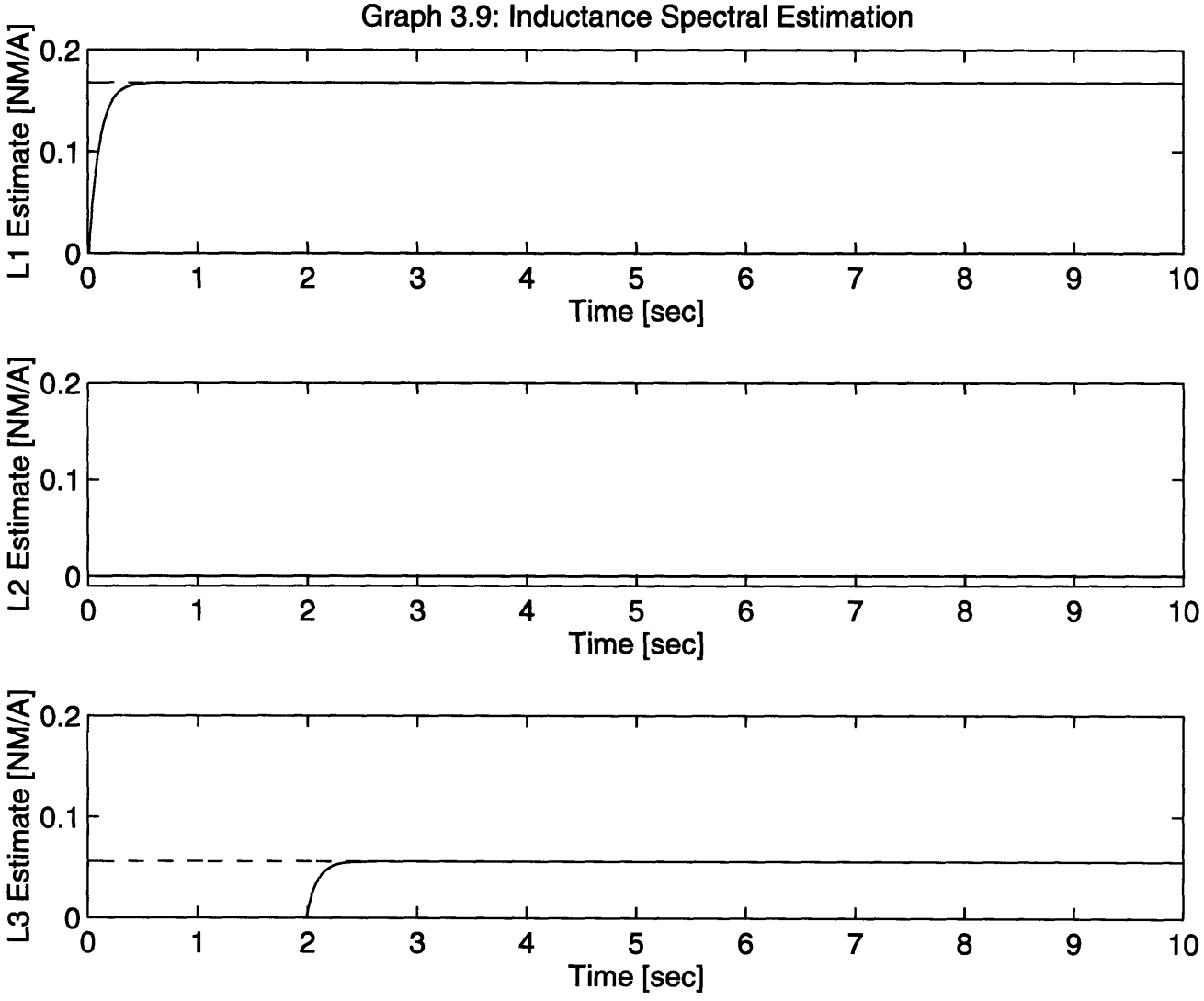

Graph 3.10: Cogging Spectral Estimation

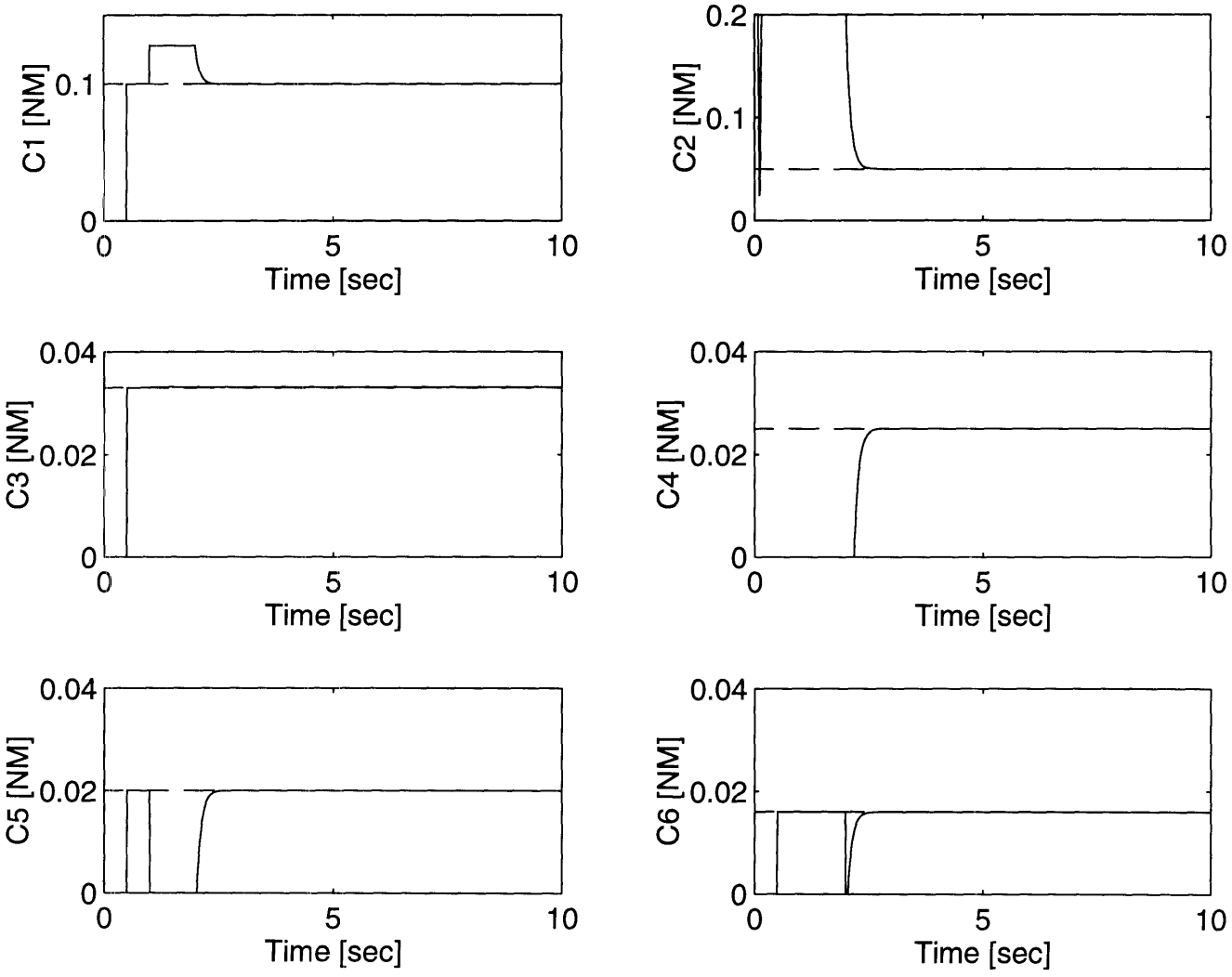

4 Active Torque Ripple Reduction Part II: Current Enforcement

The development of an active torque ripple reduction controller in Chapter 3 has assumed that the stator current waveforms commanded by the controller are followed without errors in amplitude, phase, or frequency content. No discussion, thus far, has been given to the power electronics required to track the current commands and the limits that are imposed. In this chapter, these issues will be addressed. A circuit topology designed to meet the specifications of an ATRR system will be presented along with both simulation and experimental test results.

4.1 The Current Controlled Voltage Source Inverter (CCVSI)

It is useful in many applications, including this one, to think of the inputs to the motor as the stator currents instead of stator voltages. However, the winding currents are not independent of the stator voltage. There are important electrical dynamics in the stator windings which limit the rate of change of the stator currents. A lumped parameter model for the winding dynamics is shown in **Figure 2.2**. At some point, these dynamics must be considered and controlled which is the responsibility of the inverter.

It is the job of the current controlled voltage source inverter (CCVSI) to apply the appropriate stator voltages to force the currents to track the desired waveform in the presence of the winding dynamics. There are many power electronic circuit topologies capable of performing this task. The H-Bridge configuration, shown in **Figure 4.1**, is one of the most common. This configuration will be considered here since it can apply bipolar voltages to stator(*i.e.* V_{bus} and $-V_{bus}$) while operating from a single polarity supply bus, which is the type of bus commonly found in AUVs. Detailed explanation of other power electronic inverters can be found in reference[31].

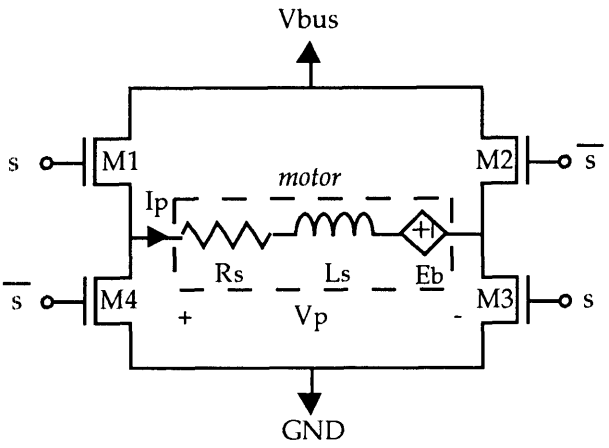

Figure 4.1: H-Bridge Circuit

Figure 4.1 represents only a single phase. The circuitry is repeated once for each stator phase.

The H-Bridge inverter works by alternately opening and closing pairs of semiconductor switches (M1,M3) and (M2,M4). The quantity s in **Figure 4.1** is a Boolean variable with "1" indicating a closed switch and "0" indicating an open switch. With s equal to "1", the switches M1 and M3 are closed, and M2 and M4 are open. The bus voltage is applied with positive polarity to the winding(*i.e.* $V_p = +V_{bus}$). With s equal to "0", the state of each switch is reversed. The bus voltage is now applied with negative polarity to the winding(*i.e.* $V_p = -V_{bus}$). The duty ratio, d_x, is defined as the fraction of the time s is equal to "1". By controlling the duty ratio, the *average* voltage applied to the windings can range from $-V_{bus}$ to V_{bus}.

$$V_p = (2d_x - 1)V_{bus} \tag{4.1}$$

Note that for the H-Bridge configuration, a 50% duty ratio(*i.e.* $d_x = 0.5$) means zero average voltage applied to the winding. Similarly, the *average* value of the generated current will be a function of the applied average voltages. Thus, the duty ratio can be used to control the average value of the currents in the winding.

The stator current waveform will also contain a ripple component. **Figure 4.2** shows typical winding voltage and current waveforms. There is a concern that the current ripple caused by the inverter switching may generate unacceptable torque ripple components. Since the ATRR controller relies on

the inverter to generate current waveforms, torque ripple caused by the inverter itself can not be canceled by the controller. Therefore, it is necessary to design the circuitry of the inverter such that current ripple and the resulting torque ripple is minimized.

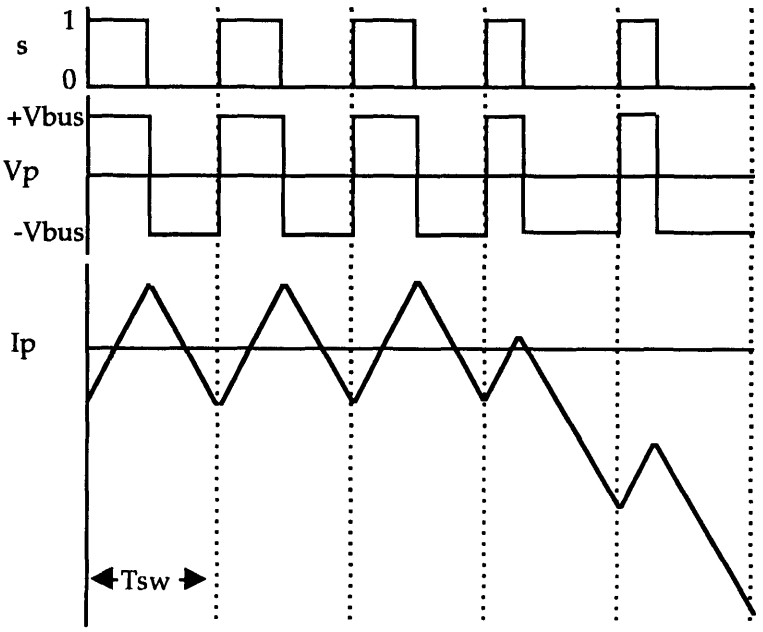

Figure 4.2: Typical Voltage and Current Waveforms

Provided the switching frequency is much faster than the time constant of the winding(*i.e.* L_S/R_S) and the bus voltage is much greater than the back EMF voltage, then the amplitude of the ripple current can be approximated by the following equation.

$$I_{ripple} \approx \frac{1}{4}\frac{V_{bus}}{L_s}\frac{1}{f_{sw}} \tag{4.2}$$

where f_{sw} is the switching frequency of the inverter. The ripple component of the current is inversely related to the inverter switching frequency, and thus, can be made small by increasing the switching speed. Additionally, the mechanical damping of the motor and load will behave as a low pass filter, attenuating the high frequency components of torque ripple. Thus, increasing the switching frequency not only reduces the current ripple it also helps to attenuate the resulting torque ripple.

Unfortunately, the inverter switching frequency can not increased without bounds. The semiconductor switches will have a maximum frequency, and higher switching speeds will result in higher losses due to heat. Thus, switching noise and efficiency must be traded-off in the design of the drive's power electronics.

The inverter switching frequency also places a limit on the highest current harmonic that can be generated by the inverter. The theoretical limit is given by the Nyquist Sampling Frequency or half of the switching frequency. In practice, a lower limit should be placed on the maximum commanded frequency to account for non-idealities. As a rule of thumb, five samples per period is usually required to sufficiently capture a sinusoidal waveform. Therefore, the highest commanded current harmonic should have a frequency less than f_{sw} / 5. **Table 4.1** lists the highest attainable current harmonic versus shaft speed for a typical motor.

Rotor Speed [RPM]	Fundamental Electrical Frequency [Hz]	Highest Harmonic Number / Frequency [Hz]
1	0.4	12,500 / 5000
5	2.0	2,500 / 5000
10	4.0	1,250 / 5000
50	20.0	250 / 5000
100	40.0	125 / 5000
500	200.0	25 / 5000
1000	400.0	12 / 4800
5000	2000.0	2 / 4000

Table 4.1: Highest Current Harmonic vs. Rotor Speed

The values in **Table 4.1** were computed assuming an inverter switching frequency of 25 kHz and a motor with 24 pole pairs, which are typical values for an AUV drive system, see reference[6]. The number of available harmonics decreases quickly as the shaft's rotational speed increases. Above 5000 RPM, the motor is moving too quickly to impose any current harmonics. Thus, ATRR is not applicable to very high speed motors. Fortunately, torque ripple suppression for the AUV application is most needed in the low to mid speed regime(*i.e.* under 1000 RPM). At higher speeds, the high load torque(Equation **(2.10)**) filters out the majority of the ripple.

4.2 Standard Pulse-Width Modulation (PWM) Schemes

The control signal to the H-Bridge(*i.e.* the switching signal s) must encode the shape of the desired current waveform. This is usually accomplished by storing the information in the width of the switching pulses known as pulse-width modulation (PWM). It is the burden of the PWM scheme to compute the optimal switching pattern to best track a reference current command. Standard PWM schemes fall into one of three classes[33]: bang-bang hysteresis control, triangle comparison, and voltage prediction. The selection of the appropriate PWM scheme for a given application usually involves a tradeoff in simplicity of implementation versus tracking performance.

High gain hysteresis control provides a simple, low cost PWM solution, see **Figure 4.3**. In the Bang-Bang Hysteresis scheme, the measured winding current is compared to the reference. If the winding current is too low, the stator voltage is switched positive to raise the current. If the current is too high, the voltage is switched negative to lower it. A small hysteresis band is introduced between the switching thresholds to limit the inverter switching frequency.

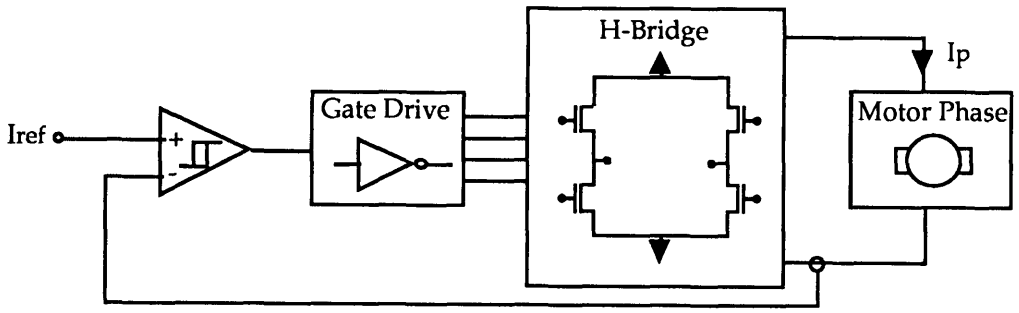

Figure 4.3: Bang-Bang Hysteresis PWM Scheme

Graph 4.1 presents a simulation of this scheme showing a typical current waveform. The width of the hysteresis band is the main design consideration. A narrower band will result in a smaller ripple current and more frequent inverter switching. One benefit of this scheme is that the hysteresis controller can be implemented using a single operational amplifier for each phase. The main drawback is that the inverter switching is variable and uncontrolled. This is unacceptable for high performance motor systems.

The triangle comparison method is a slightly more complicated PWM scheme(see **Figure 4.4**). The error between the reference and the measured winding current is compared to a fixed frequency triangle wave to generate the inverter switching signal. Current tracking is done by a proportional-plus-integral controller.

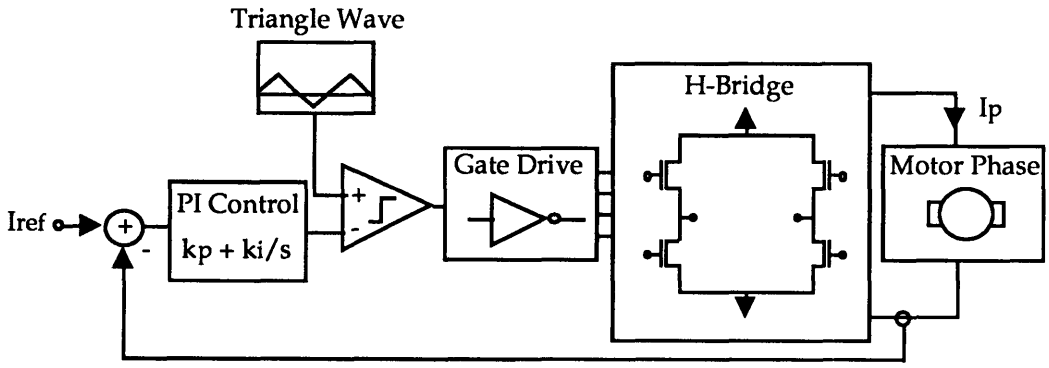

Figure 4.4: Triangle Comparison PWM Scheme

Graph 4.2 presents simulated waveforms generated by this scheme. In this scheme, the inverter switching frequency is constant and equal to the triangle wave frequency which is an improvement over the previous scheme. The problem here is that the PI controller introduces a frequency dependent phase lag between the reference and actual current waveforms. For a system which requires arbitrary current waveform generation such as the torque ripple controller described in Chapter 3, this phase lag will introduce harmonic distortion degrading the effectiveness of the controller. Modified versions of the triangle comparison method such as clock turn on and turn off[34] can remove phase delay but introduce unacceptable low frequency distortion by tracking either an upper or lower edge of the reference current waveform.

Voltage Prediction PWM methods offer the best performance at the expense of complexity. In VP schemes, a mathematical algorithm for computing the optimal switching pattern is developed and implemented using a microprocessor. This type of PWM scheme is the most flexible and the most expensive to implement, and therefore, is only used when extreme high performance is required. VP algorithms are usually optimized for a specific application(*e.g.* see references [35], [36], and [37]). In the next section, a VP scheme designed specifically for arbitrary current waveform generation and torque ripple reduction is proposed.

4.3 Model Reference PWM Scheme

A novel PWM scheme which is optimized for generating arbitrary current waveforms with minimal harmonic distortion is shown in **Figure 4.5**. This scheme uses a combination of voltage prediction and triangle comparison with PI tracking concepts. Frequency dependent winding models

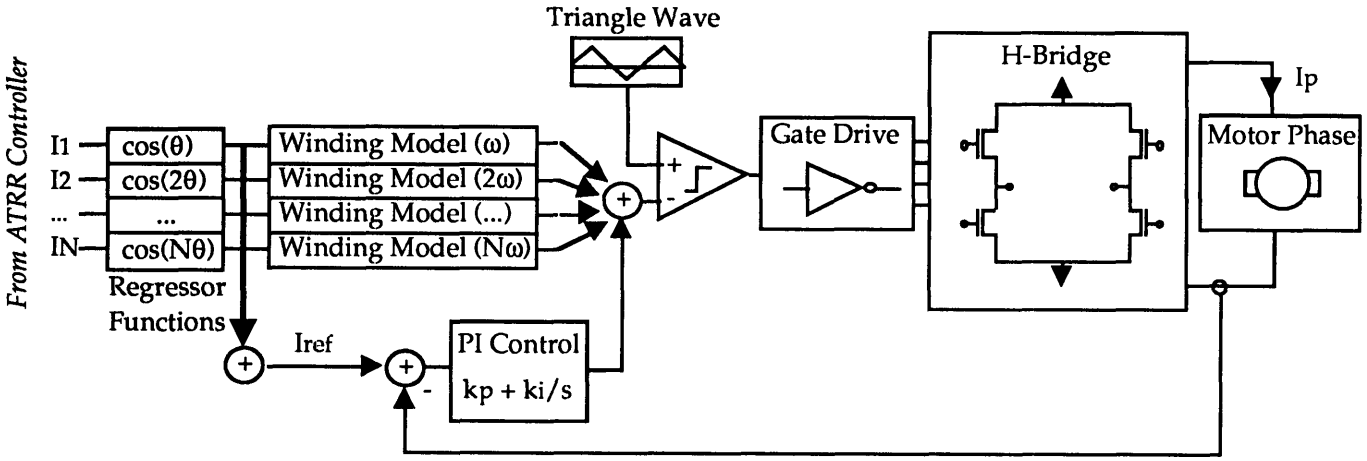

Figure 4.5: Model Reference PWM Scheme

are used to predict the voltage required to generate each commanded current harmonic. A current tracking PI controller is used to compensate for errors in the winding models. Although some phase-lag is still present due to errors in the winding model, it is minimized since the feedback controller is tracking a smaller error between the actual and predicted waveforms.

A single-phase model for the stator windings is shown in **Figure 2.2**. Assuming the mutual inductance between the phases is negligible,

$$V_s(\omega) = L_s(\omega)\frac{di_s}{dt} + R_s(\omega)i_s + E(\omega) \qquad (4.3)$$

where V_s is the applied stator voltage; i_s is the stator current; L_s and R_s are the stator's self-inductance and resistance respectively; and E is the excitation voltage. This model is the basis for many voltage prediction PWM schemes, see references [33], [35], [36], and [37].

In general, L_s, R_s, and E are all functions of the excitation frequency ω. Saturation in the stator core causes a change in the self-inductance at low frequencies. At high frequencies, the mutual inductance between stator phases changes the effective inductance seen at the stator terminals. The skin effects cause the stator resistance to increase as the excitation frequency is increased. Slot harmonics distort the shape of the excitation voltage waveform giving E some frequency content. All these effects mean that each current harmonic sees a *different* stator which is one source of harmonic distortion. Using a frequency dependent model, the appropriate voltage waveform to eliminate this distortion can be computed.

Using physical arguments with some assumptions, models for each of these effects can be derived. The stator inductance is only effected at extreme low and high frequencies. For the limited current spectrum required here, it is acceptable to approximate the stator inductance as a constant. The change in the stator resistance can be modeled by the following equations,

$$R_s(\omega) = \rho_{cu} \frac{L}{A_{eff}(\omega)} \tag{4.4}$$

$$A_{eff}(\omega) = \frac{k_{cu}}{\omega} \tag{4.5}$$

where ρ_{cu} is the resistivity of copper, L is the length of the winding, A_{eff} is the *effective* area of the winding, and k_{cu} is the skin effect constant for copper. The excitation voltage shape is a complicated function of the motor's specific geometry. However, it can be measured by externally driving the shaft. The harmonic content of the waveform can be analysis providing a model for the given motor.

One concern in the implementation of the winding model is the sensitivity of the differentiator(*i.e.* di/dt) to parasitic signals. To reduce this problem, the pure differentiator can be approximated by a lead filter, limiting the gain of high frequency noise. This solution also limits the operational bandwidth of the circuit; however, this is acceptable for motor drive applications because of the separation between the electrical frequency of the motor and the PWM frequency. **Figure 4.6** shows the implementation the

winding model. For the AUV application, a lead cut-off frequency of 10 kHz was found to be acceptable(*i.e.* ω_0= 63 krad/sec).

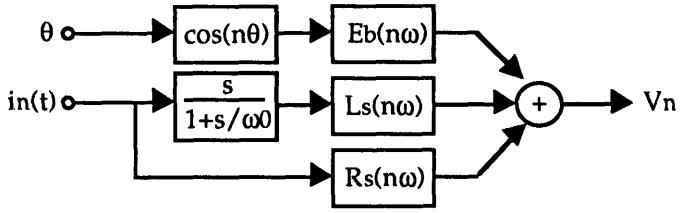

Figure 4.6: Winding Model

A second concern is sensitivity to parameter uncertainties in the winding model. This is an issue for any model reference scheme[37]. For each current harmonic, the stator voltage component V_n can be broken into two terms- the model predicted term and a parameter error term.

$$V_n + v_n = (L_s + l_s)\frac{di_s}{dt} + (R_s + r_s)i_s + (E + e) \tag{4.6}$$

$$v_n = l_s\frac{di_s}{dt} + r_s i_s + e \tag{4.7}$$

The uppercase variables are the model predicted terms, and the lowercase variables are the error components. As shown by Equations **(4.6)** and **(4.7)**, the error voltage v_n appears as an *additive* disturbance to the modeled plant.

To minimize the error voltage, v_n in Equation **(4.7)**, a PI compensator is used with current feedback. The tracking performance of *each harmonic* can be analyzed by averaging all variables over the PWM switching period and deriving the transfer function realization shown in **Figure 4.7**.

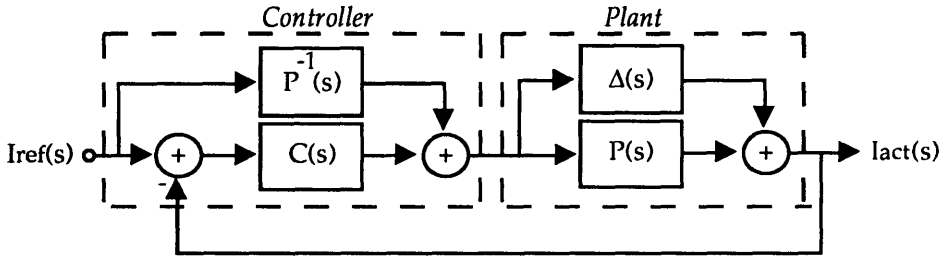

Figure 4.7: Transfer Function Representation

P(s) is the transfer function associated with the winding model. Δ(s) represent the error dynamics. C(s) is the transfer function of the PI compensator.

Ignoring the back EMF terms (i.e. E and e) for simplicity, these transfer functions are:

$$P(s) = \frac{1}{sL_s + R_s} \tag{4.8}$$

$$\Delta(s) = \frac{1}{sl_s + r_s} \tag{4.9}$$

$$C(s) = \frac{k_p s + k_i}{s} \tag{4.10}$$

Including the back EMF terms make P(s) and $\Delta(s)$ unnecessarily more complicated and does not add insight into the analysis. Using this background, the following output/input transfer function can be derived,

$$\frac{I_{act}(s)}{I_{ref}(s)} = \frac{1 + (P + \Delta)C + \Delta P^{-1}}{1 + (P + \Delta)C} \tag{4.11}$$

Provided the gain of the compensator, C(s), is designed to be much greater than the error term $\Delta(s)P^{-1}(s)$ over the frequencies of interest, then the transfer function simplifies to

$$\frac{I_{act}(s)}{I_{ref}(s)} \approx 1 \tag{4.12}$$

Thus, the winding current tracks the reference as desired.

4.4 Model Reference PWM CCVSI Simulation

Computer simulations were done using SIMULINK[29]. The proposed PWM scheme was tested in three scenarios: open-loop with exact parameter knowledge, open-loop with a 50% inductance model error, closed-loop with a 50% inductance model error. In addition, comparison simulation were done for two other popular PWM schemes. System for parameters for all simulation runs are shown in **Table 4.2**. Results are shown in **Graphs 4.1** through **4.5**.

Stator Inductance	Ls	103	μH
Stator Resistance	Rs	20	mΩ
Bus Voltage	Vbus	10	Volt
Back EMF Coefficient	Eb	0.5	Volt/RPM
Switching Frequency	Fsw	25	kHz

Table 4.2: Test Motor Parameters

The first two simulations illustrate the problems with Bang-Bang Hysteresis Control and Triangle Comparison with PI Tracking. **Graph 4.1** shows unregulated switching patterns exhibited by high gain hysteresis feedback. **Graph 4.2** shows the inherent phase-lag of a simple PI tracking controller. The remaining simulations demonstrate the performance the model reference PWM scheme. **Graph 4.3** shows the behavior of the system using the winding model open-loop, assuming exact motor parameter knowledge. As expected, the current tracks the command with no phase lag. The current error is dominated by switching ripple. A 50% error in the inductance estimate results in a degradation of the control, see **Graph 4.4**. A negative inductance error(*i.e.* l_s) causes a negative voltage error(*i.e.* v_s) during rising portions of the reference current waveform(*i.e.* $di_{ref}/dt > 0$) and a positive error during the falling portions. Thus, the actual current should track beneath the rising reference and above the falling reference which is clearly shown on **Graph 4.4**. The current error now has a significant component at the input frequency in addition to the ripple term. The feedback compensator, when enabled, will use this component of the current error signal to correct the applied stator voltage. **Graph 4.5** shows the performance of the system closed-loop in the presence of the 50% inductance error. As expected, the current error has been corrected.

Graph 4.1: Bang–Bang Hysteresis PWM Scheme

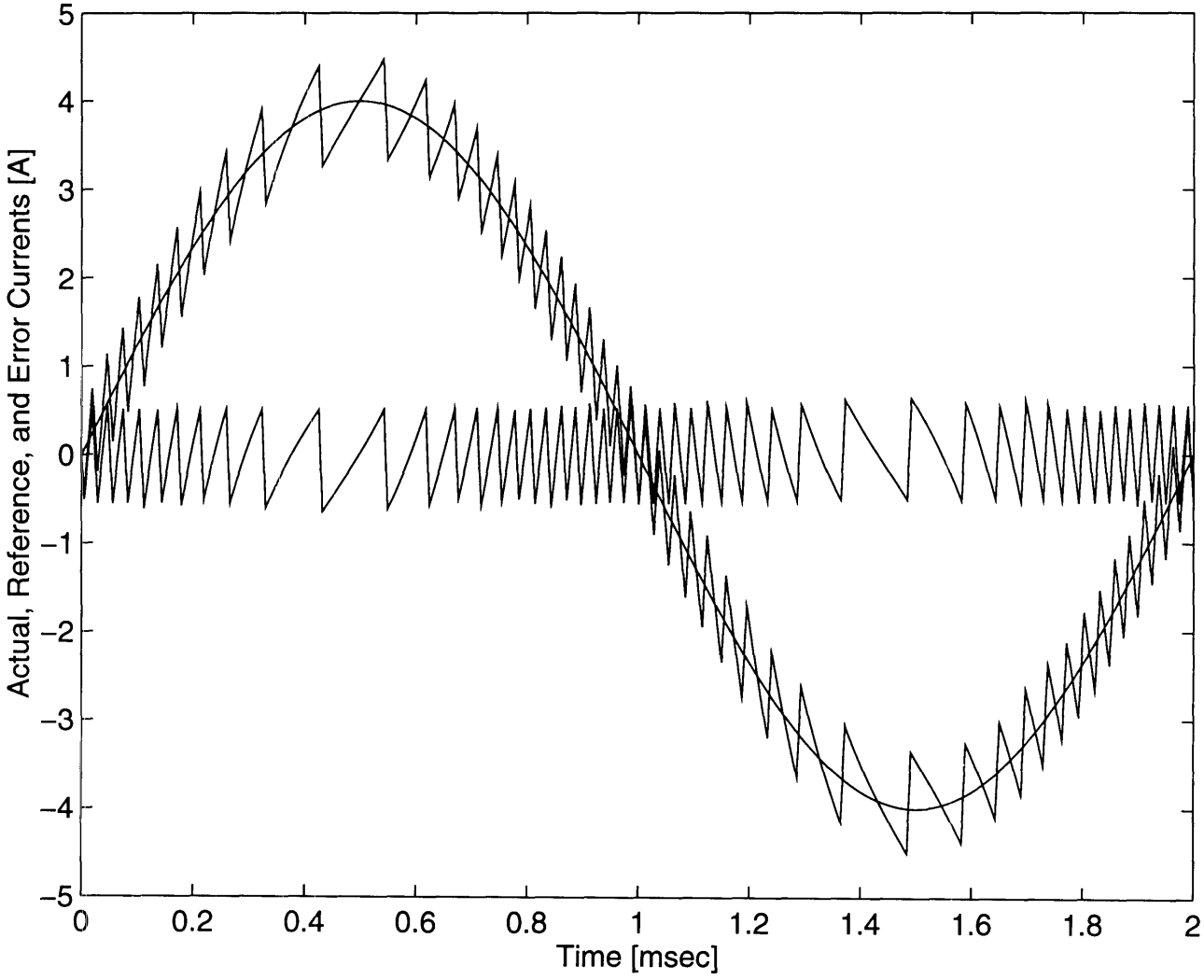

Graph 4.2: Triangle Comparison with PI Tracking PWM Scheme

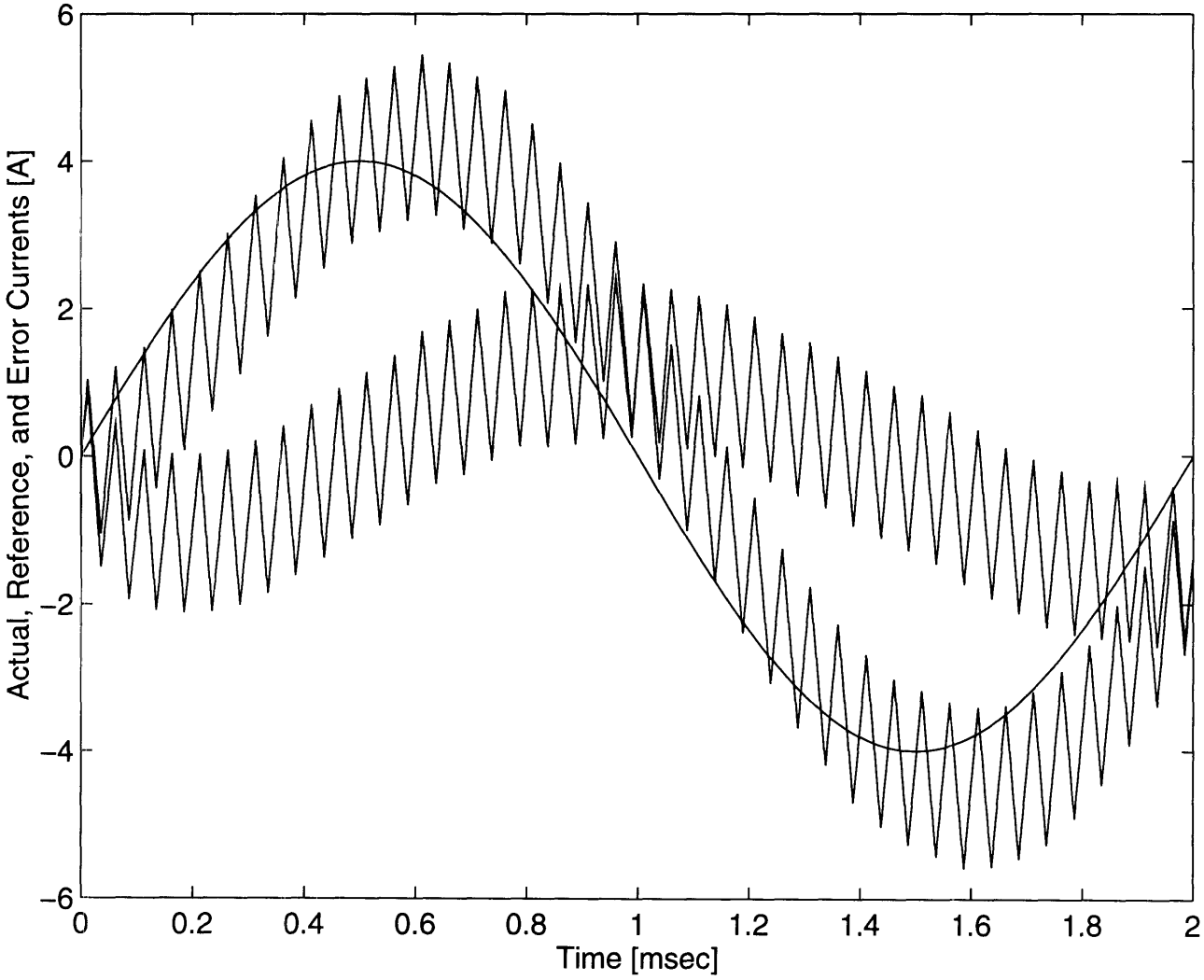

Graph 4.3: Model Reference PWM Scheme-- Open Loop, Exact Model Parameters

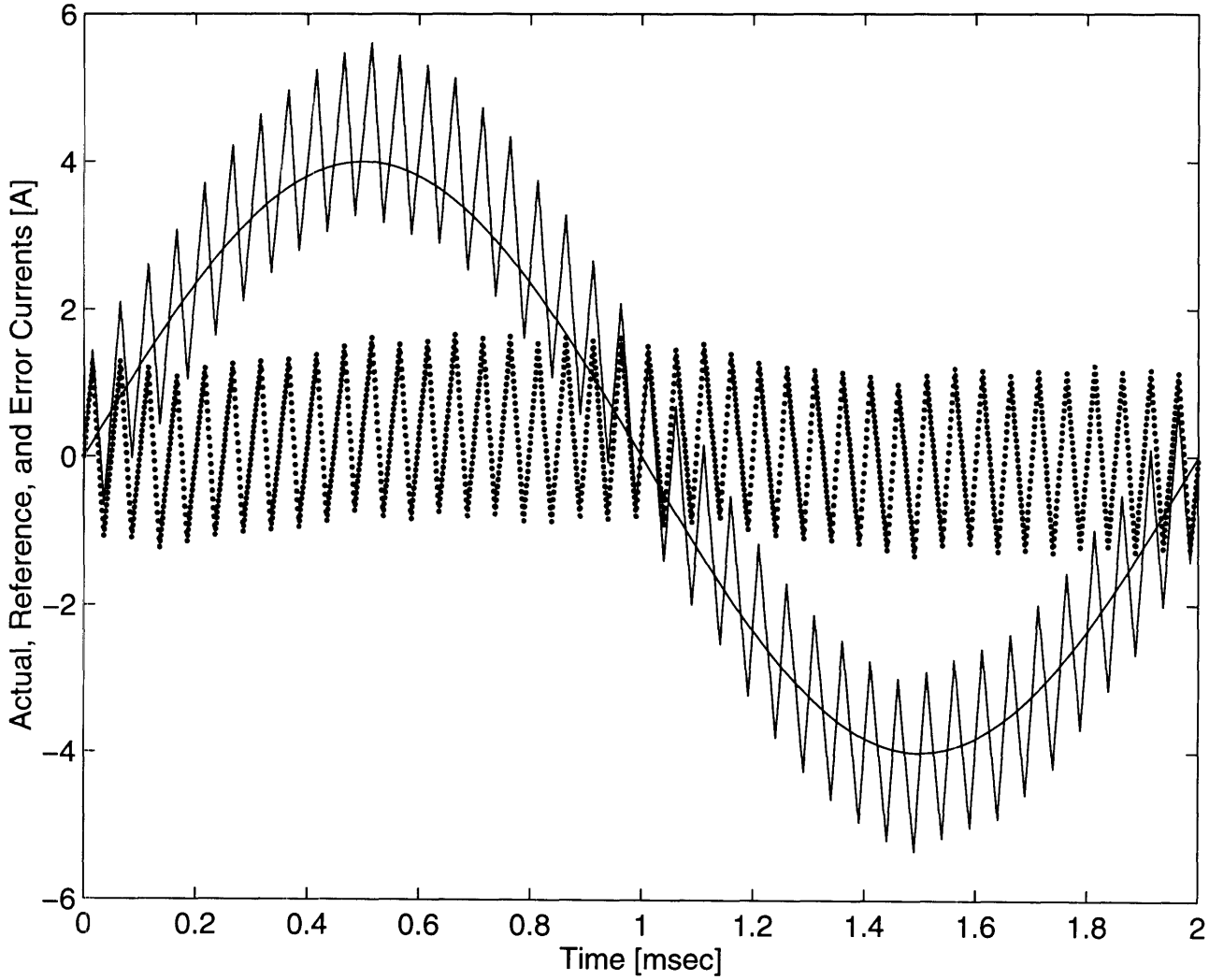

Graph 4.4: Model Reference PWM Scheme-– Open Loop, 50% Model Inductance Error

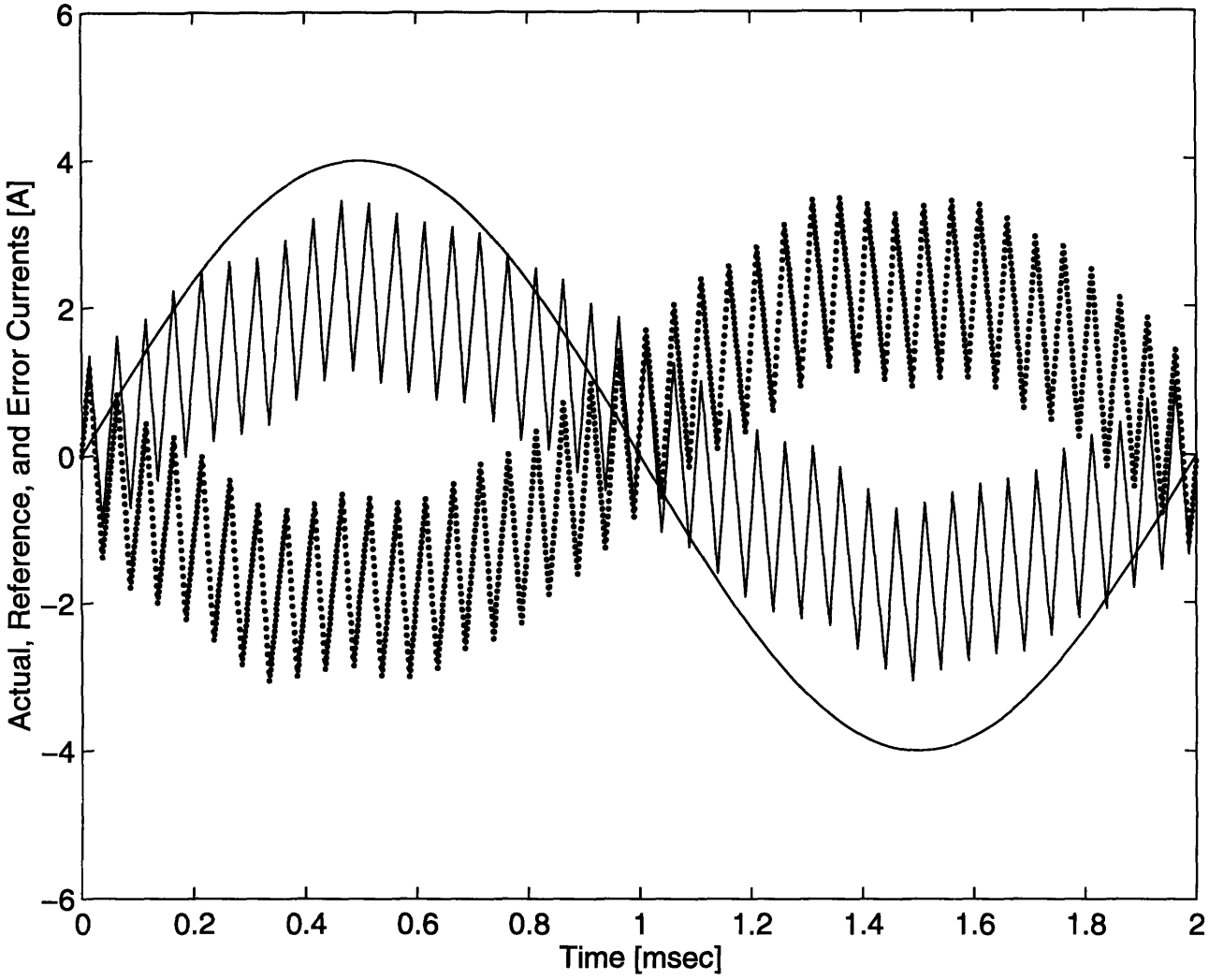

Graph 4.5: Model Reference PWM Scheme-- Closed Loop, 50% Model Inductance Error

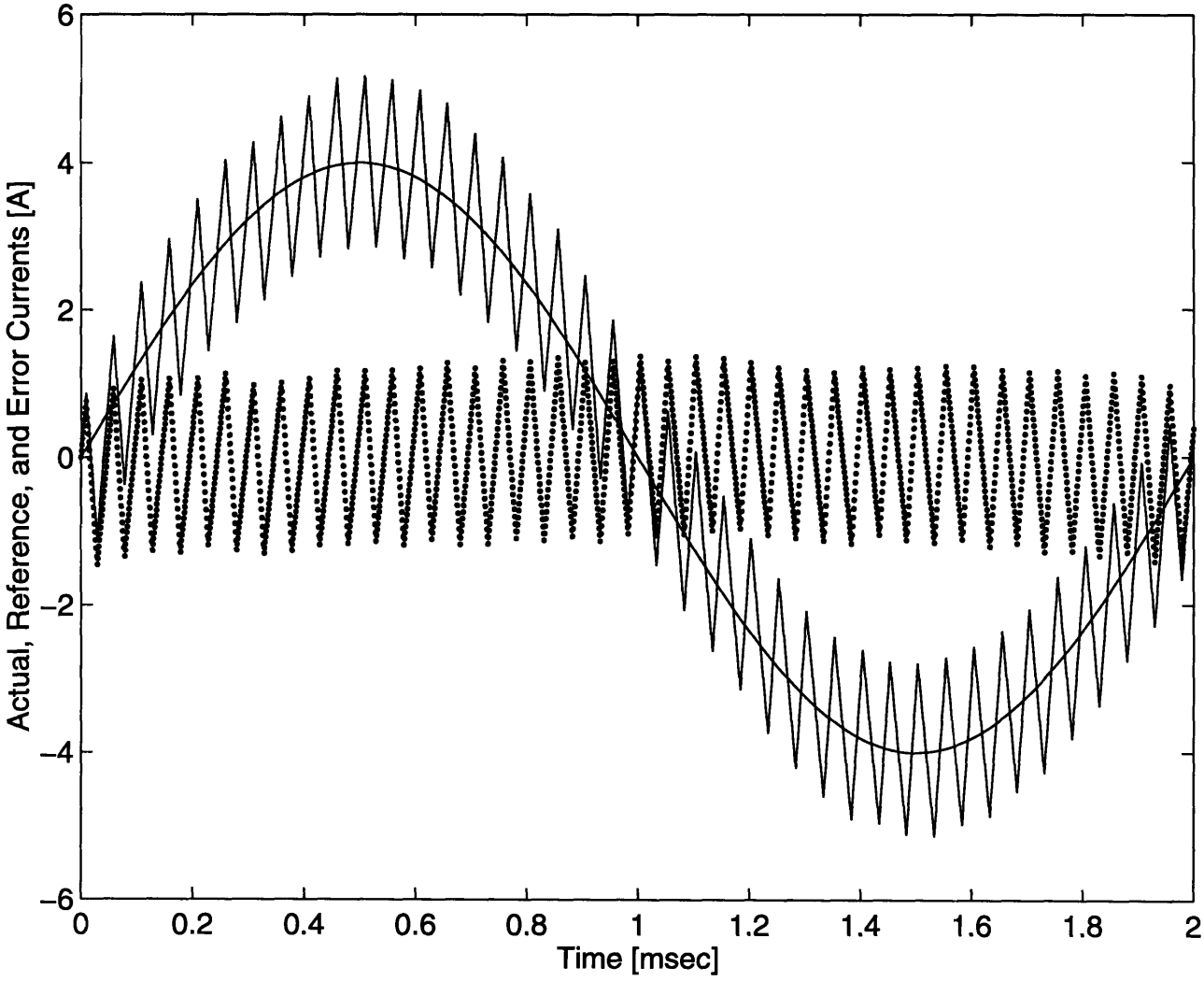

4.5 Model Reference PWM CCVSI Experimental Results

A single harmonic implementation of the model reference PWM scheme using low cost analog components was experimentally tested as a proof of concept. The circuit was constructed on a breadboard and tested on a "dummy" stator(*i.e.* the rotor had been removed). The electrical parameters of the stator are the same as the one's used for the simulation runs, see **Table 4.2**. However, since the rotor had been removed, the back EMF is zero.

The current tracking behavior of the circuit was studied through a number of open-loop and closed-loop tests. The reference, actual, and error current waveforms for these tests are given in **Graphs 4.6** through **4.11**. The commanded current for all tests was a 4A, 600 Hz sinusoid. To evaluate parameter robustness, an intentional inductance error was added to the winding model for some tests.

Graph 4.6 shows the reference, actual, and error current waveforms with the circuit running open-loop. For this test, the model parameters were set as close as possible to the measured values. The graph shows the actual current waveform slightly leading the reference in phase and a small amplitude offset. There are three possible reasons for these errors. First, 10% resistors were used in the construction of the winding model circuitry which lead to small modeling errors. Second, an error could have been introduced in the measurement of the stator's electrical parameters. Name plate values were used. Third, the assumptions in the underlying winding model also introduced errors. The effects of inductive coupling *between* phases was not modeled. These errors are the reason why current feedback is employed to improve the overall performance. **Graph 4.7** shows the same test with the PI compensator enabled. The small phase and amplitude offsets have been eliminated. **Graph 4.8** shows the contribution of the feed-forward and feedback terms to the control command. As expected, the feed-forward component dominates the control with the feedback providing small corrections.

Graphs 4.9, 4.10, and **4.11** are intended to demonstrate the robustness of the system. A 50% error was subtracted from the inductance estimate. The

open-loop performance of the system degraded significantly (**Graph 4.9**). With the PI compensator enabled, the current errors are eliminated (**Graph 4.10**). **Graph 4.11** shows the two components of the control waveform for this test. As expected, the feedback component has increased to compensate for the lack of a good parameter estimate.

Graph 4.6: Reference, Actual, and Error Current Waveforms; Open-Loop

Vertical Scale: 1 A/div
Horizontal Scale: 500 μsec/div

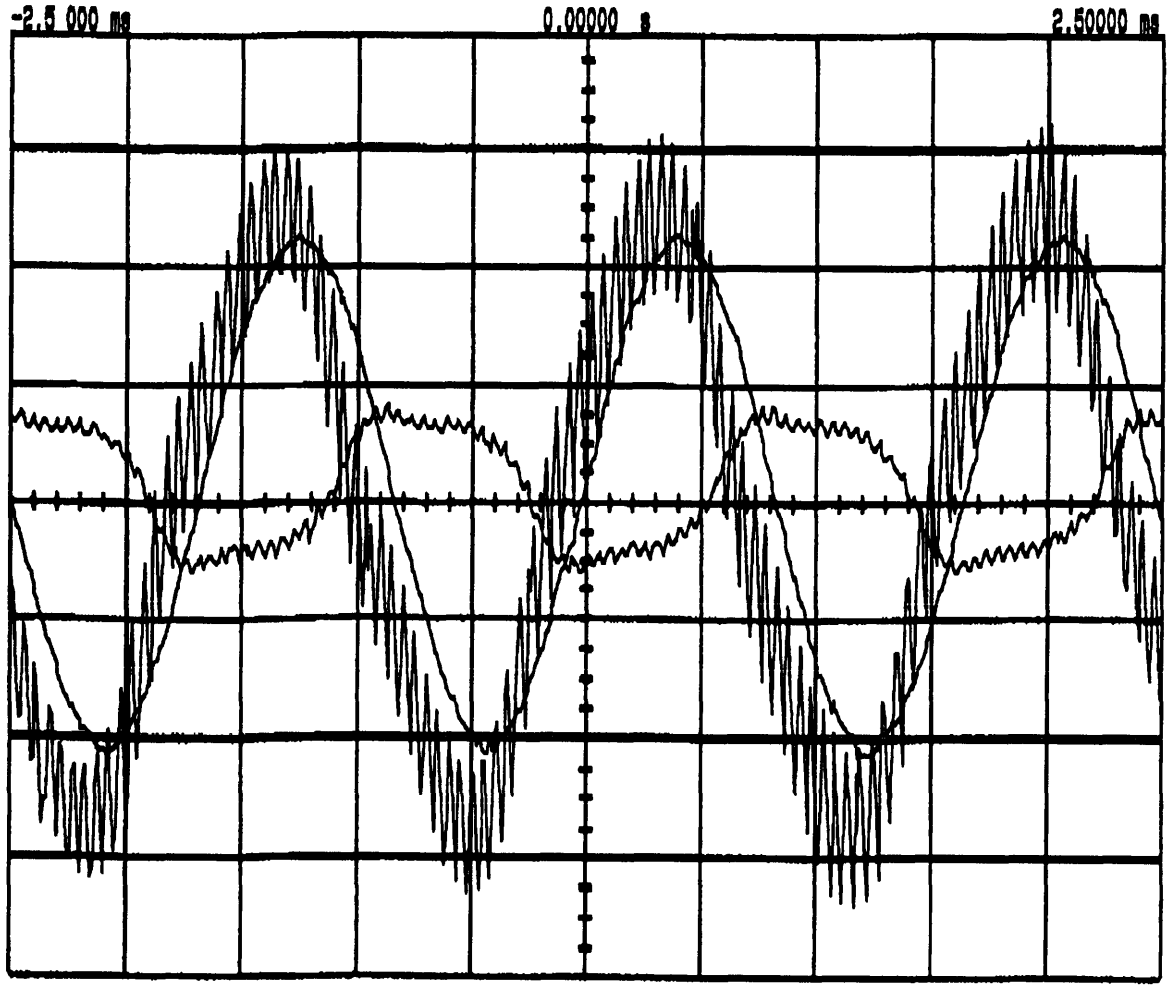

Graph 4.7: Reference, Actual, and Error Current Waveforms; Closed-Loop

Vertical Scale: 1 A/div
Horizontal Scale: 500 μsec/div

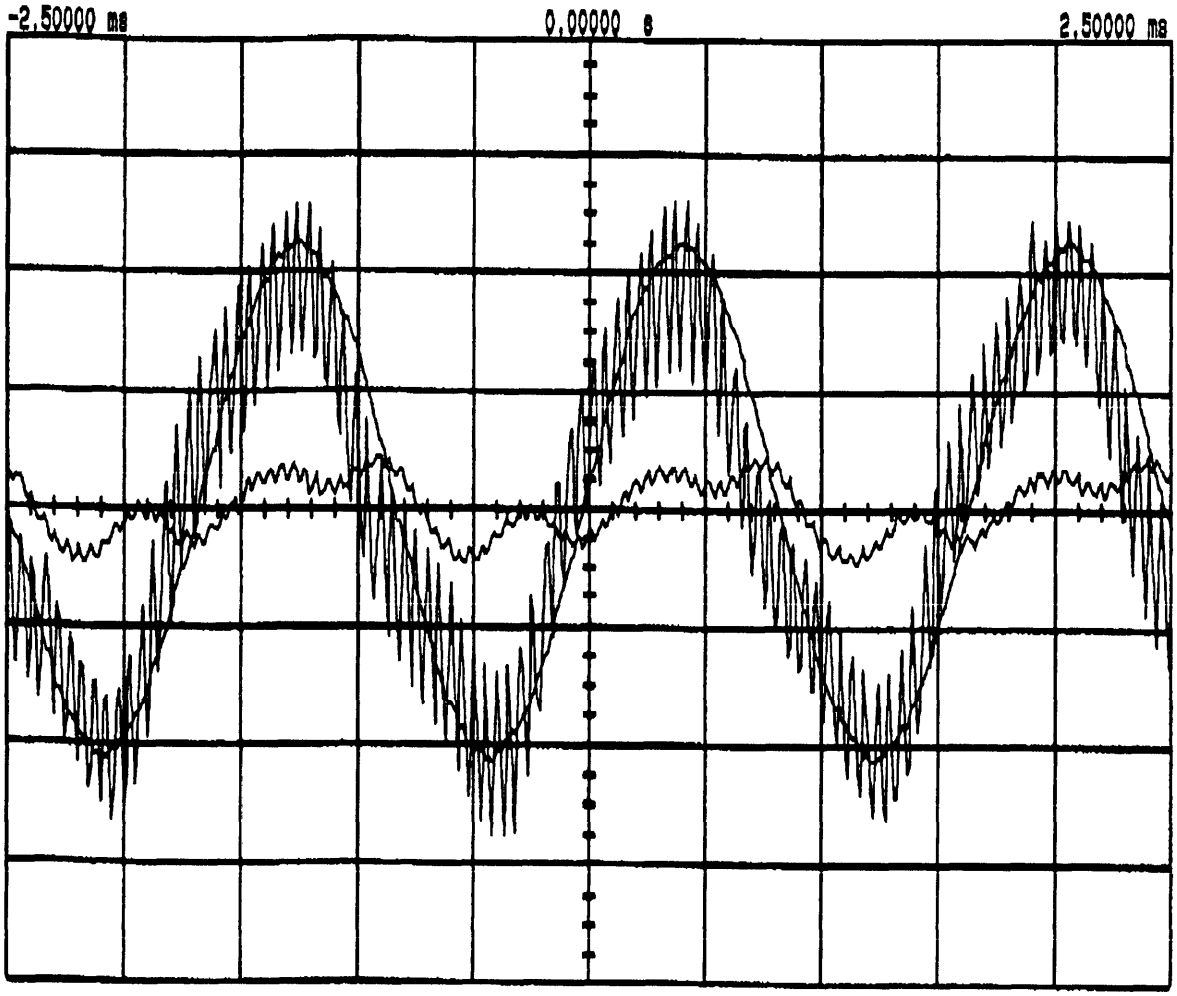

Graph 4.8: Voltage Predictor and PI Compensator Duty Cycle Commands

Vertical Scale: 1 V/div
Horizontal Scale: 500 μsec/div

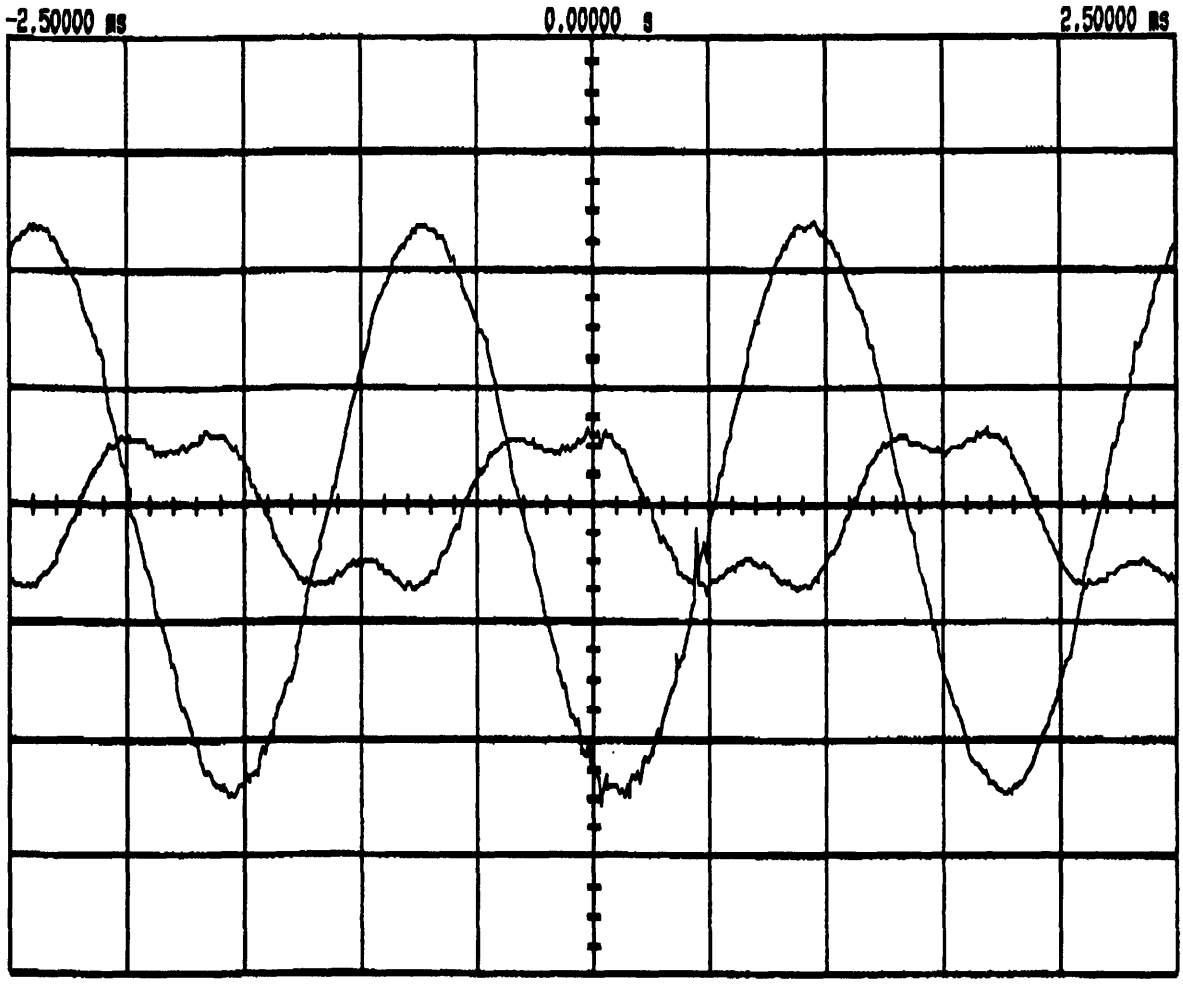

Graph 4.9: Reference, Actual, and Error Current Waveforms;
Open-Loop with Gross Inductance Error

Vertical Scale: 1 A/div
Horizontal Scale: 500 μsec/div

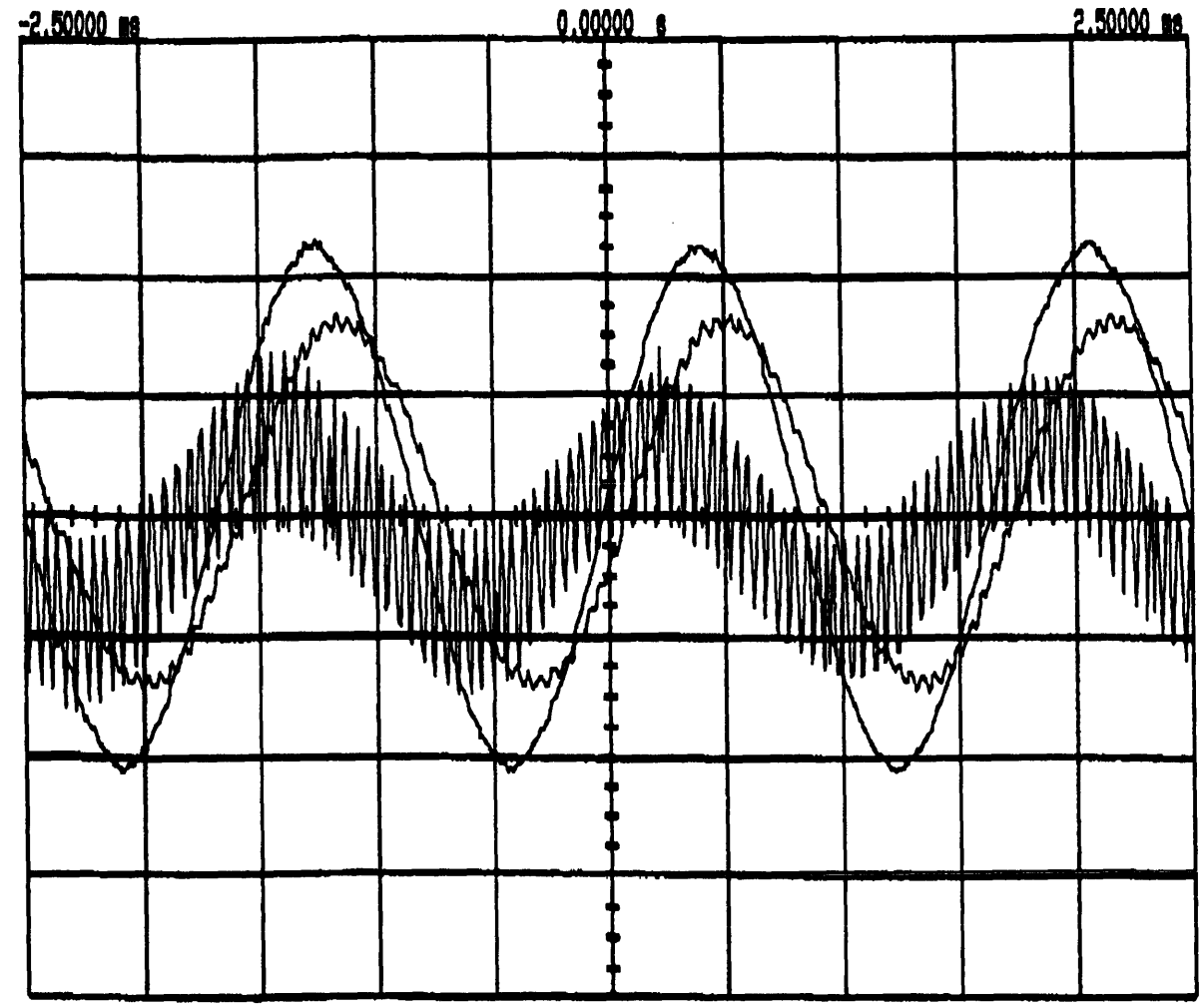

Graph 4.10: Reference, Actual, and Error Current Waveforms;
Closed-Loop with Gross Inductance Error

Vertical Scale: 1 A/div
Horizontal Scale: 500 μsec/div

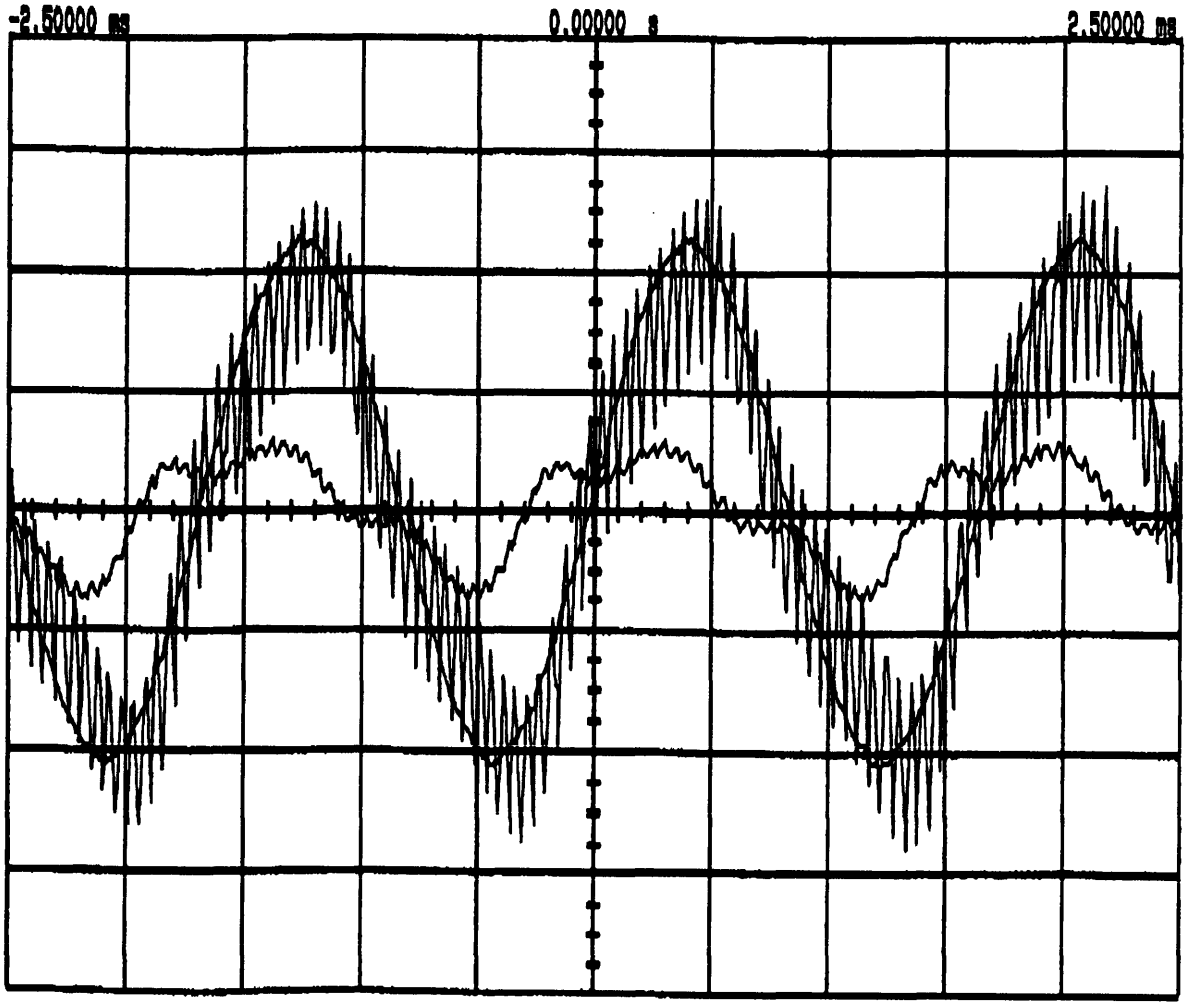

Graph 4.11: Voltage Predictor and PI Compensator Duty Cycle Commands; Closed-Loop with Gross Inductance Error

Vertical Scale: 1 V/div
Horizontal Scale: 500 μsec/div

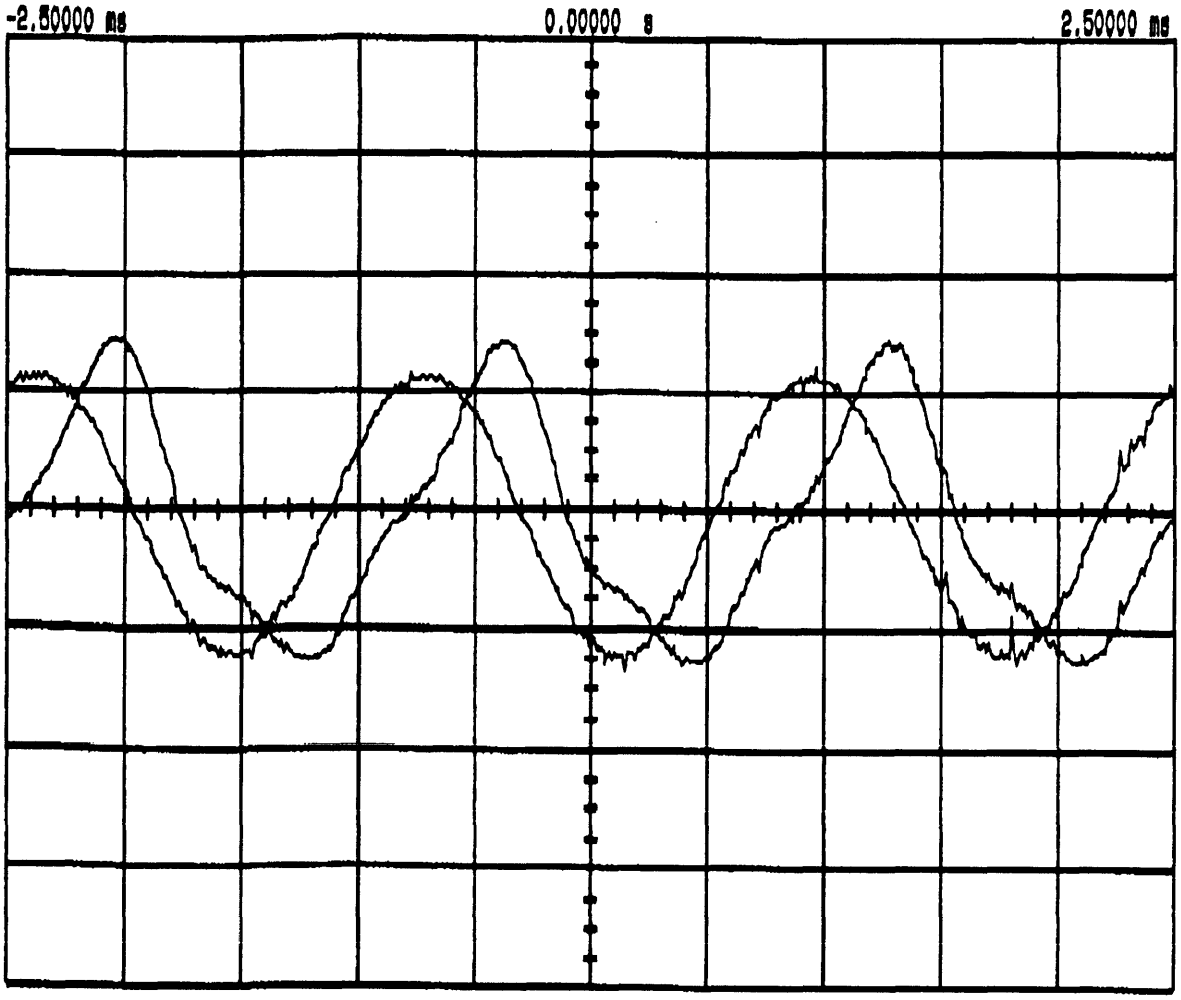

5 Practical Issues

There are a number of issues which must be considered before implementing the torque ripple reduction scheme described previously. These include limits imposed by the current controlled voltage source inverter(CCVSI), measurement of the torque ripple and identification of its frequency components, and discretization errors introduced by the speed sensor. Each issue will have an impact the system's performance, and therefore, should influence relevant design choices.

5.1 Power Electronics Limitations

The power electronic subsystem was described in detail previously. In addition to the PWM issues discussed in Chapter 4, the VSI is limited in its ability to generate current waveforms. Key among these limitations is the inverter's slew rate.

The slew rate is defined here as the maximum rate of change of the stator's current. The complete dynamics of the stator current waveforms are given by Equation **(4.3)**. To reduce heat losses, the stator resistance will be minimal for many machines; thus, the $R_s i_s$ voltage will be small in comparison to the other terms. Equation **(4.3)** can be simplified to the following,

$$V_s \approx L_s \frac{di_s}{dt} + E \tag{5.1}$$

Solving for the current's rate of change,

$$\frac{di_s}{dt} = \frac{1}{L_s}(V_s - E) \tag{5.2}$$

where L_s is the stator's self-inductance, V_s is the applied stator voltage, and E is the back EMF waveform. Assuming the "ON" voltage of the semiconductor switches uses in the inverter(see **Figure 4.1**) are small compared to the bus voltage, the magnitude of the applied stator voltage will be equal to the bus voltage, *i.e.*

$$|V_s| = V_{bus} \tag{5.3}$$

The back EMF , E(t), will be a periodic waveform with some peak value $|E|$. For example, a sinusoidal back EMF would have the following form:

$$E(t) = |E|\cos(N_p\theta) \tag{5.4}$$

where N_p is the number of pole pairs and θ is the rotor's position. The back EMF *subtracts* away from the applied stator voltage in its ability to change the current. Therefore, the *effective* stator voltage is difference between the applied voltage V_s and the back EMF E(t).

$$V_{eff} = V_s - E \tag{5.5}$$

The effective voltage, and therefore the current slope, is smallest when the back EMF waveform is at an extreme. Thus, the maximum enforceable current change is limited to

$$\left|\frac{di_s}{dt}\right|_{max} = \frac{1}{L_s}(V_{bus} - |E|) \tag{5.6}$$

The current waveform commanded by the torque ripple reduction controller will be the sum of N harmonics, *i.e.*

$$i_s(t) = I_1 e^{jN_p\theta(t)} + I_2 e^{j2N_p\theta(t)} + \ldots + I_n e^{jnN_p\theta(t)} \tag{5.7}$$

The rate of change of the stator current waveform required to generate this waveform has contributions from each harmonic, *i.e.*

$$\frac{di_s}{dt} = jN_p\omega I_1 e^{jN_p\theta} + j2N_p\omega I_2 e^{j2N_p\theta} + \ldots + jnN_p\omega I_n e^{jnN_p\theta} \tag{5.8}$$

In the worst case scenario, each of the harmonic terms are in phase resulting in the following maximum required current slope,

$$\left|\frac{di_s}{dt}\right|_{max} = N_p\omega|I_1| + 2N_p\omega|I_2| + \ldots + nN_p\omega|I_n| \tag{5.9}$$

The limit of the power electronics to change the stator current was given previously by Equation **(5.6)**. Comparing Equations **(5.6)** and **(5.9)**, it is clear

that a limit must be imposed the amplitude of each current harmonic to insure that the rate of change of the commanded waveform does not exceed the ability of the power electronics. Assuming that equal weighting is given to each harmonic component, the following amplitude limit should be place on the k^{th} commanded harmonic,

$$|I_k| \leq \frac{1}{k} \frac{V_{bus} - |E|}{nN_p \omega L_s} \tag{5.10}$$

where n is the number of current harmonics.

5.2 Torque Spectrum Measurement

A key input to the adaptive controller described in Chapter 3 is the torque ripple spectrum. To actively control (minimize in this case) the ripple spectrum, it is necessary to precisely measure the torque ripple and quickly compute its frequency components. The torque ripple measurement can be done using a *torque transducer*. This device is composed of material whose electrical characteristics (usually resistivity) change as a function of applied stress. when place on the drive shaft, the transducer produces an electrical signal which provides a measure of the tangential torque being applied to the load. The transducer is more accurate than mechanical accelerometers and has a higher bandwidth than ripple measurements computed from rotor speed changes.

The torque transducer mentioned above provides a time domain signal of the torque ripple. The adaptive control algorithm described in Chapter 3 needs the harmonics, magnitude and phase, of the load torque signal. One method for extracting the frequency content of this signal is the complex Fourier expansion. The load torque signal can be written as the following series,

$$T_L(t) = \sum_{n=-N}^{N} T_n e^{jnN_p\theta} \tag{5.11}$$

where T_k is the complex Fourier coefficient of the k^{th} torque ripple harmonic. Given that the torque ripple is periodic in θ, $T_L(t)$ over one full rotation

period is required to compute the fouler coefficients of all ripple harmonics, *i.e.*

$$T_n = \frac{1}{2\pi}\int_0^{2\pi} T_L e^{jnN_P\theta} d\theta \qquad -N \le n \le N \qquad (5.12)$$

Unfortunately, the continuous load torque function $T_L(t)$ over a full revolution is not available. The controller will only receive discrete update at fixed sampling instants. Additionally, the controller needs to work continuously and in real-time. Given these facts, it would be useful to compute the Fourier coefficients in a recursive manner instead of direct application of Equation **(5.12)**. One method for performing this recursive computation is to store an estimate of each Fourier coefficient, and update each coefficient at each sampling instant using the latest torque ripple sample, *i.e.*

$$T_k[n] = T_{k,re}[n] + jT_{k,im}[n] \qquad (5.13)$$

$$T_{k,re}[n] = T_{k,re}[n-1] + T_L[n]\cos(k\theta[n]) \qquad (5.14)$$

$$T_{k,im}[n] = T_{k,im}[n-1] + T_L[n]\sin(k\theta[n]) \qquad (5.15)$$

where $T_L[n]$ and $\theta[n]$ are samples of the torque ripple signal and rotor position, respectively, at the n^{th} sampling instant. The estimates may be initialized to zero, *i.e.*

$$T_{k,re}[0] = 0 \qquad (5.16)$$

$$T_{k,im}[0] = 0 \qquad (5.17)$$

6 Detailed System Simulation

The following results are from a detailed SIMULINK[29] simulation of the motor model (*i.e.* Equation **(2.15)**) and ATRR controller (*i.e.* Equation **(3.40)**) described in Chapters 2 and 3. The simulation was constructed in the time domain using the true physical state-variables. Therefore, the waveforms generated by the simulation represent the true signals which would appear on a physical experimental setup. Sensor effects on measured signals are also modeled. The purpose of the simulation is to show the performance the proposed ATRR controller and provide a design tool to assist in the future implementation of system.

6.1 Simulation Parameters

The simulated motor is a three-phase, dual-stator, axial-field permanent-magnet motor. It is assumed that the three phase windings are symmetrical, and the two stators have been precisely aligned. **Table 6.1** lists the motor parameters used in the simulation.

Torque Constant	k0	0.4	NM/A
Cogging Coefficient	Lmm	0.1	H
Max Current Amplitude	Imax	150	A
Moment of Inertia	J	0.2	$kg\ m^2$
Damping Coefficient	Bw	0.1	NM/RPM^2
Number of Pole Pairs	Np	24	

Table 6.1: Simulation Parameters

These values are consistent with parameters for an axial-field PMAC motor currently under study by the NUWC in Newport, R.I. for use in a AUV drive system.

The proportional and integral gains of the speed control loop were set to provide an over-damped step response. All adaptation gains were set to unity.

6.2 Simulation Results

6.2.1 Baseline Simulation

The following set of graphs are from a simulation of the motor with torque ripple reduction scheme disabled. The data are intended to provide a baseline comparison for later simulation results.

In this simulation, the motor is given a 100 revolution per minute (RPM) step command from an initial resting state. **Graph 6.1** shows the rotor's velocity response as a function of time. The response is over-damped, as designed, and torque ripple is clearly evident in the steady-state.

Graph 6.2 shows the rotor's angular position as a function of time. The position sensor modeled here is a 16 bit resolver. Fifteen complete revolutions of the rotor occurred during this simulation.

Graph 6.3 shows the output of the speed sensor which uses periodic samples of the rotor's position to estimate its velocity. The sampling period was set to 20 milliseconds. Due to the limited sampling period, the speed sensor does not provide adequate bandwidth to capture the high frequency ripple components demonstrating the need for a separate torque sensor to measure torque ripple.

Graph 6.4 shows the commanded stator current waveforms. All three phases (a, b, and c) are shown. Since the torque ripple reduction scheme is disabled for this baseline simulation, the waveform appear as pure sinusoids at the fundamental pole frequency of the machine.

Graph 6.5 shows the steady-state torque ripple as measured from the tangential torque sensor. The ripple appears almost triangular in shape indicating the presents of the odd inductance harmonics. **Graph 6.6** indicates the spectrum of the torque ripple. The harmonic signature of the motor is clearly shown. The attenuation of these discrete peaks is the goal of torque ripple reduction.

Graph 6.1: Rotor Velocity Profile, ATRR Off

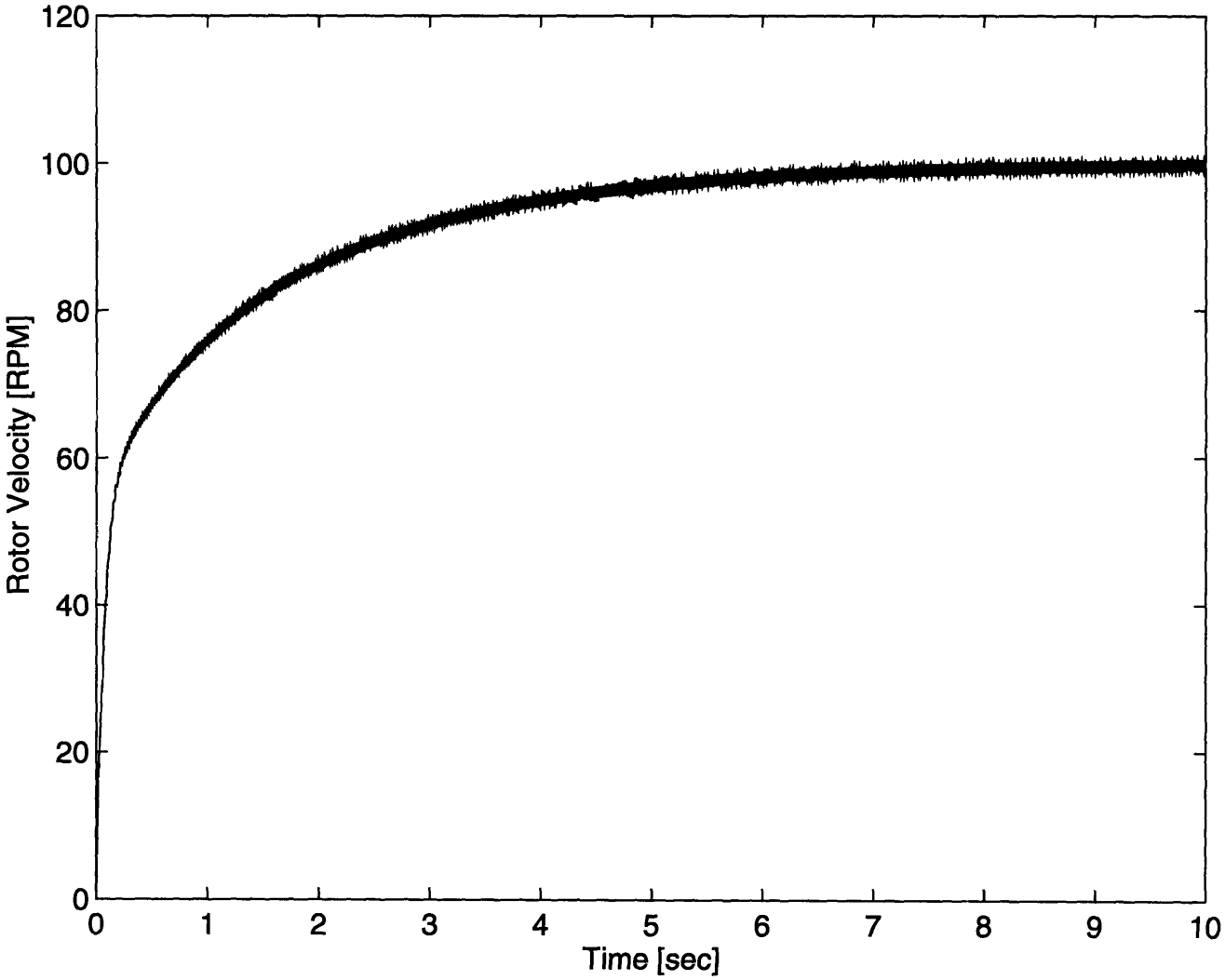

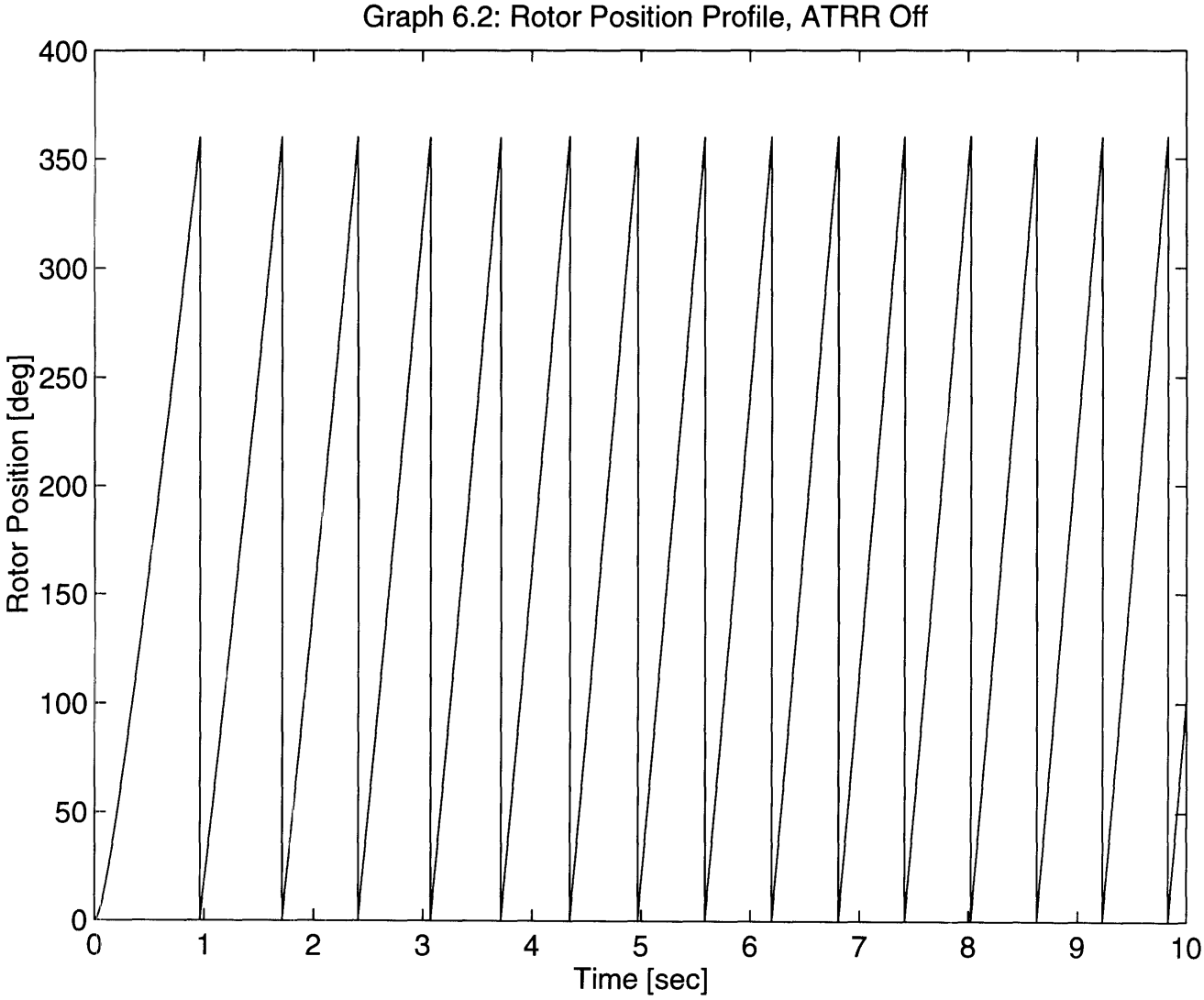
Graph 6.2: Rotor Position Profile, ATRR Off
Rotor Position [deg]
Time [sec]
400
350
300
250
200
150
100
50
0
0
1
2
3
4
5
6
7
8
9
10

Graph 6.3: Position Estimated Rotor Velocity

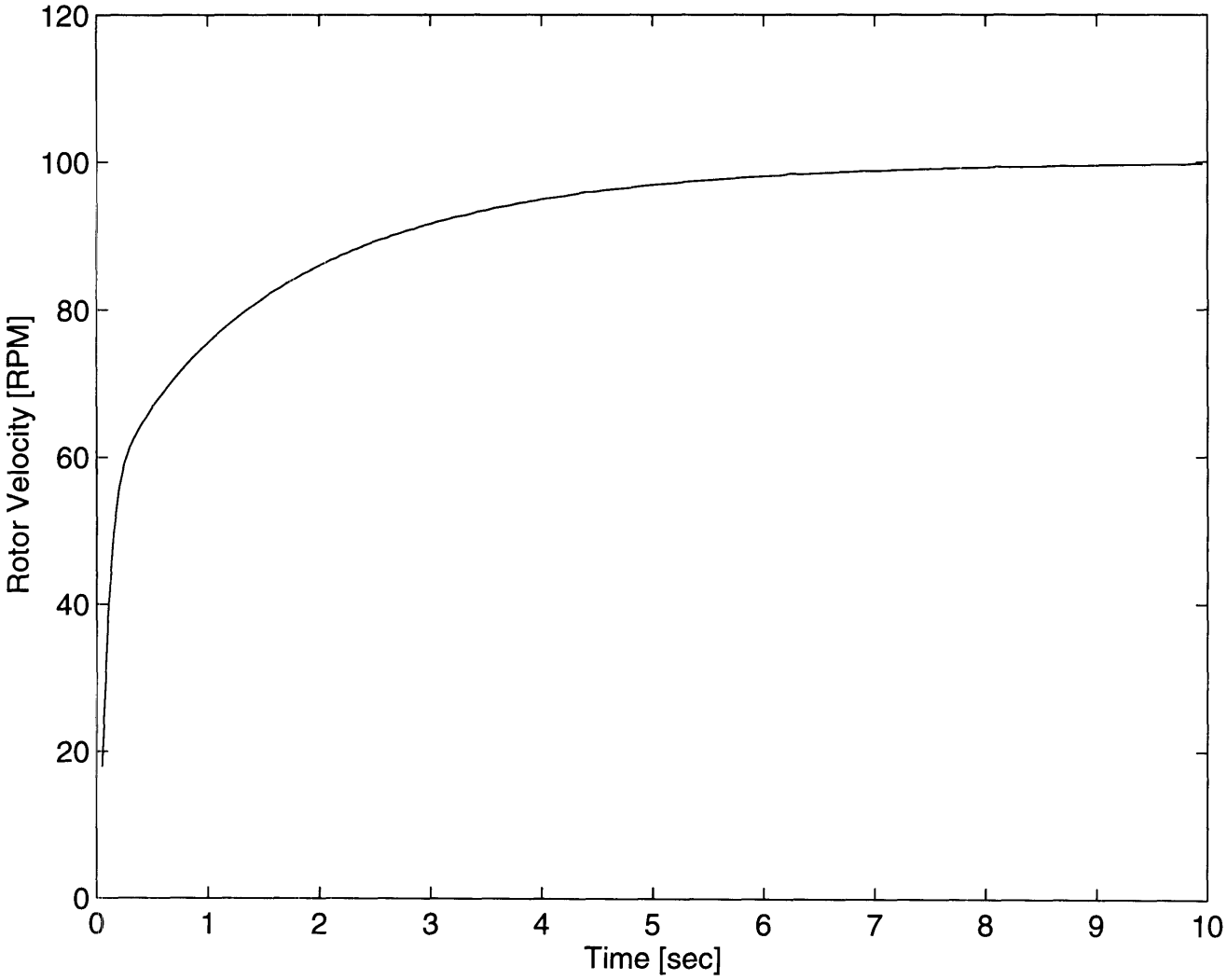

Graph 6.4: Steady–State Stator Current Waveforms, ATRR Off

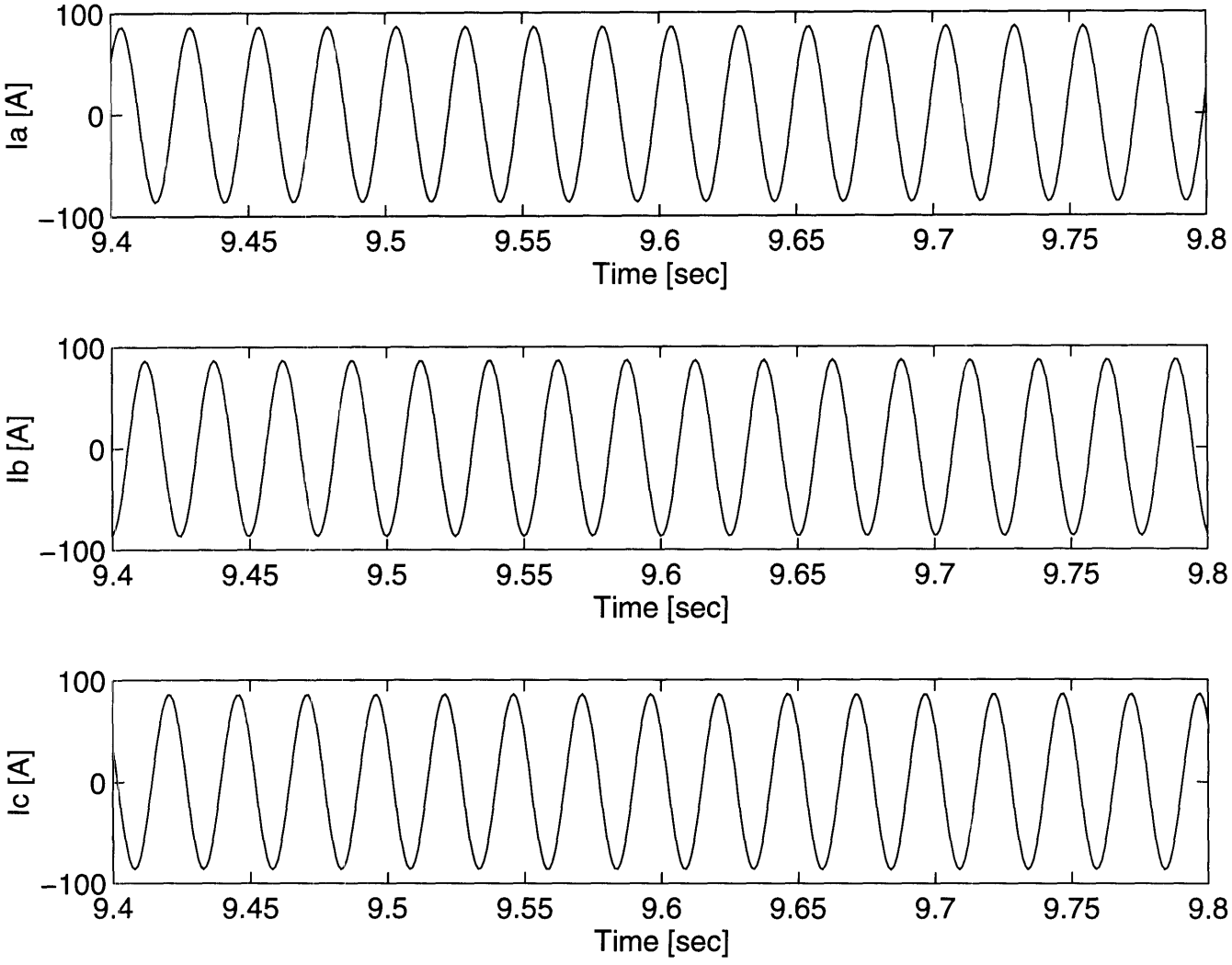

Graph 6.5: Steady–State Torque Ripple, ATRR Off

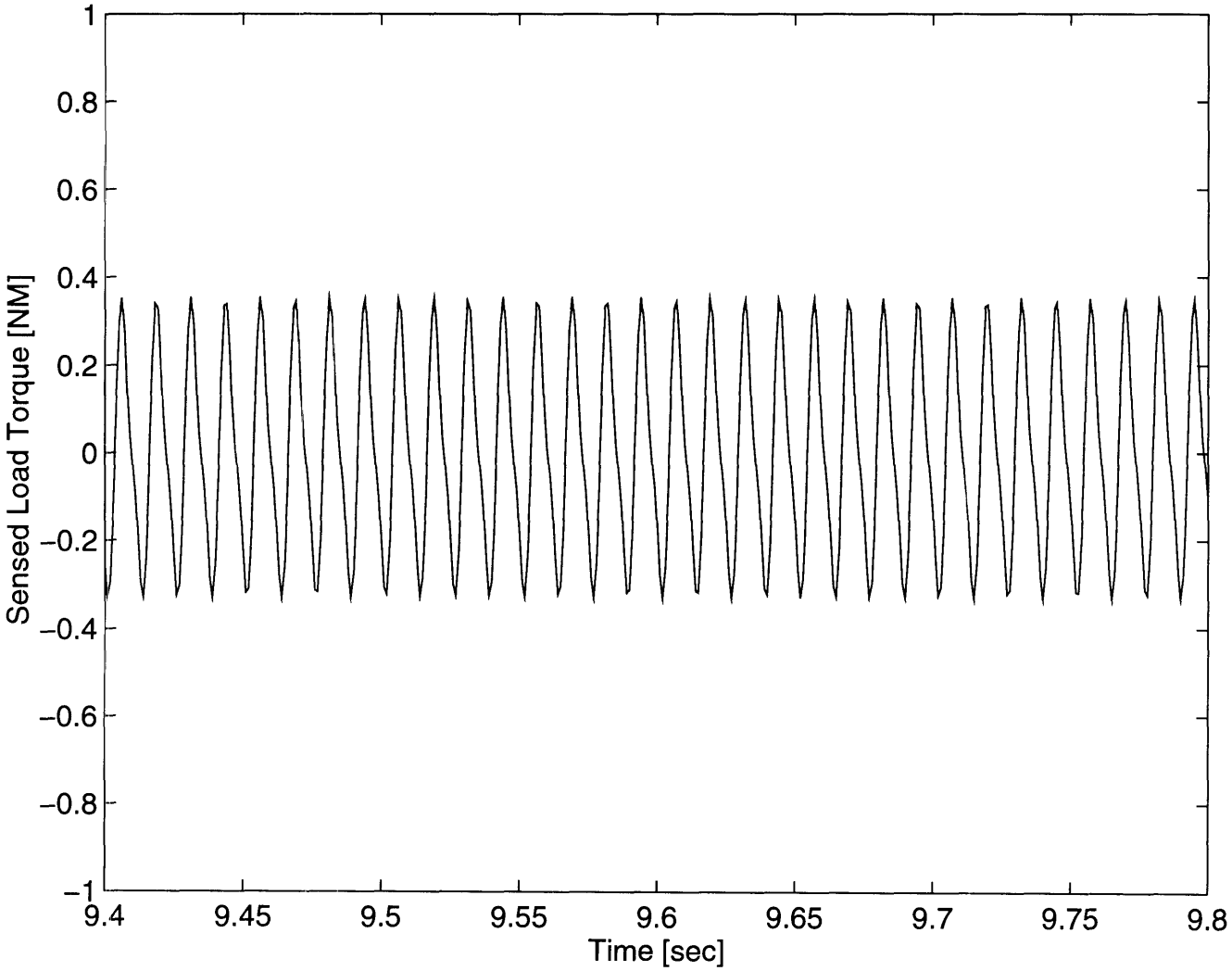

Graph 6.6: Torque Ripple Spectrum, ATRR Off

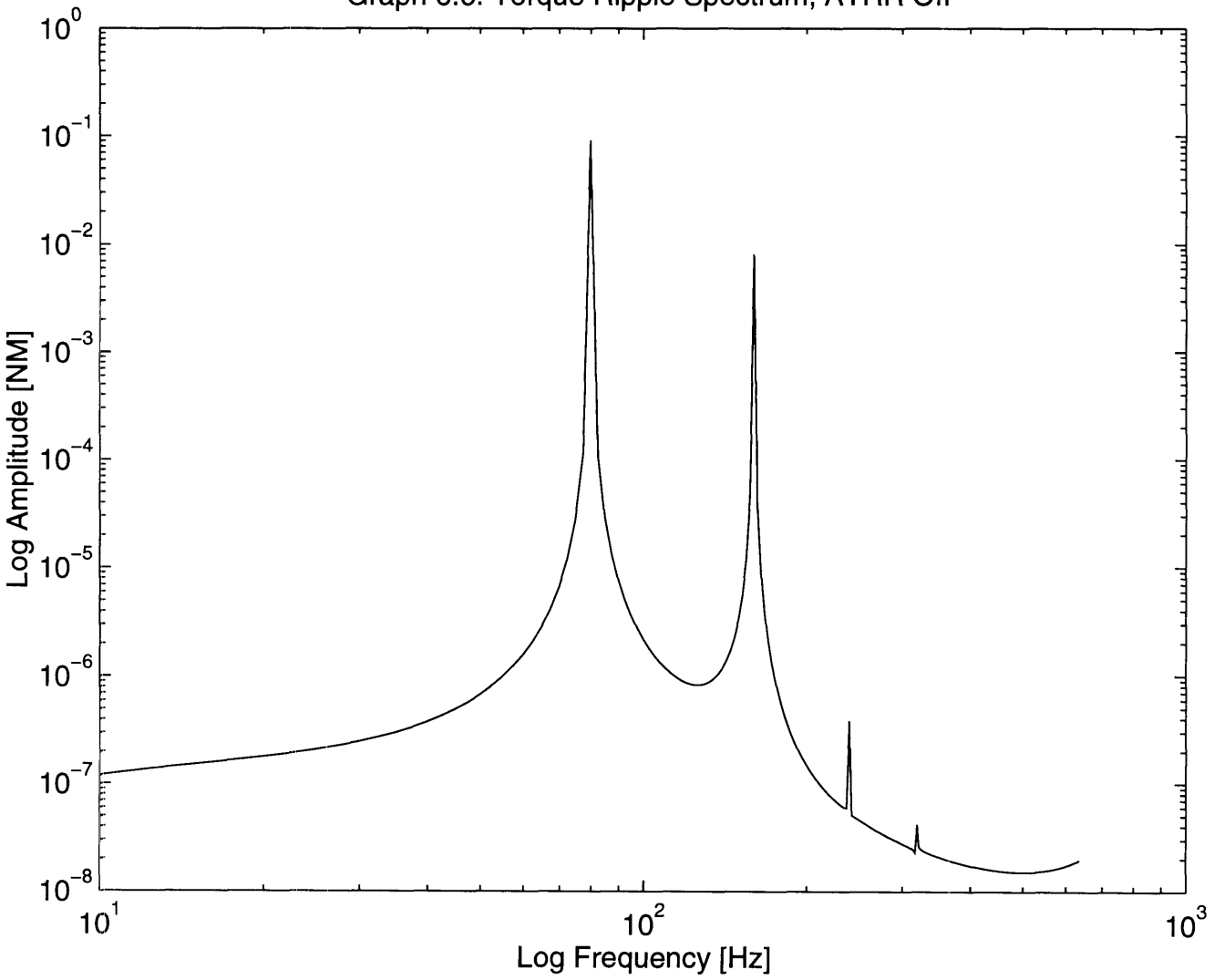

6.2.2 Active Torque Ripple Reduction Simulation

The next simulation run demonstrates the response of the motor with the active torque ripple reduction scheme activated. The same 100 RPM step commanded is used. Thus, the results shown here are directly comparable to the previous run.

Graph 6.7 shows the output of the torque sensor during the adaptation process. The top graph presents the torque signal over the complete run. The bottom two graph show "blow ups" of the torque signal at later time intervals. The torque ripple is clearly reduced as time increases.

Graph 6.8 shows the actual (not estimated) rotor velocity profile. The same over-damped response is apparent, however, the steady-state torque ripple has been virtually eliminated.

Graph 6.9 indicates the shape of the commanded current waveforms post adaptation. Again, all three phases (a, b, and c) are shown. The higher frequency content required to cancel the torque ripple is clearly evident. It is interesting to note that the three phases *do not* appear as phase shifted versions of each other.

Graph 6.10 shows the torque ripple spectrum post adaptation. Comparing this to the previous spectrum (**Graph 6.6**), the harmonic content of the torque signal has been reduced by 100 dB. If the simulation was run for a long duration, the ripple content would be reduced even further as the controller's parameters continued to adapt.

Graph 6.7: Load Torque Waveform During Adaption

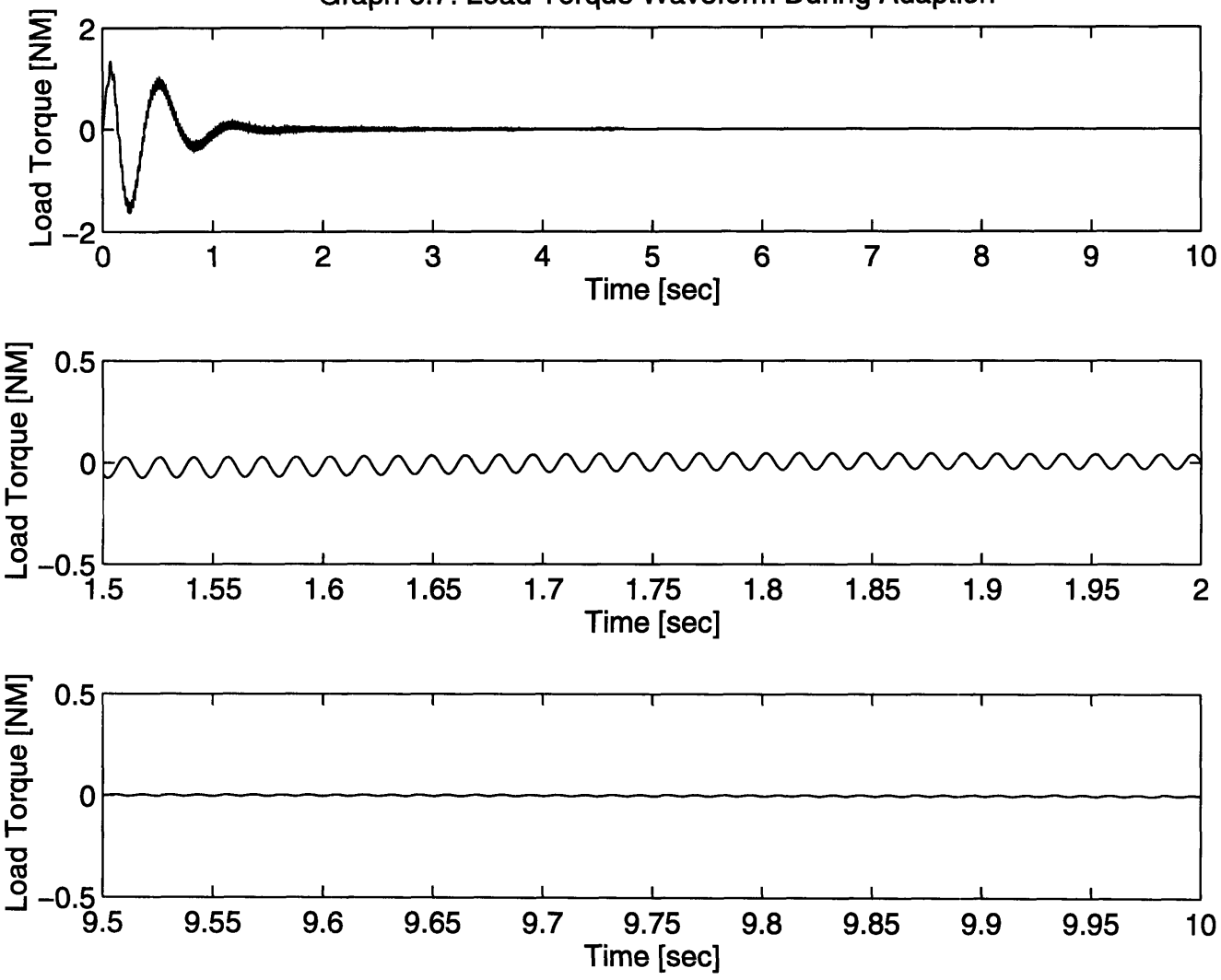

Graph 6.8: Rotor Velocity Profile, ATRR On

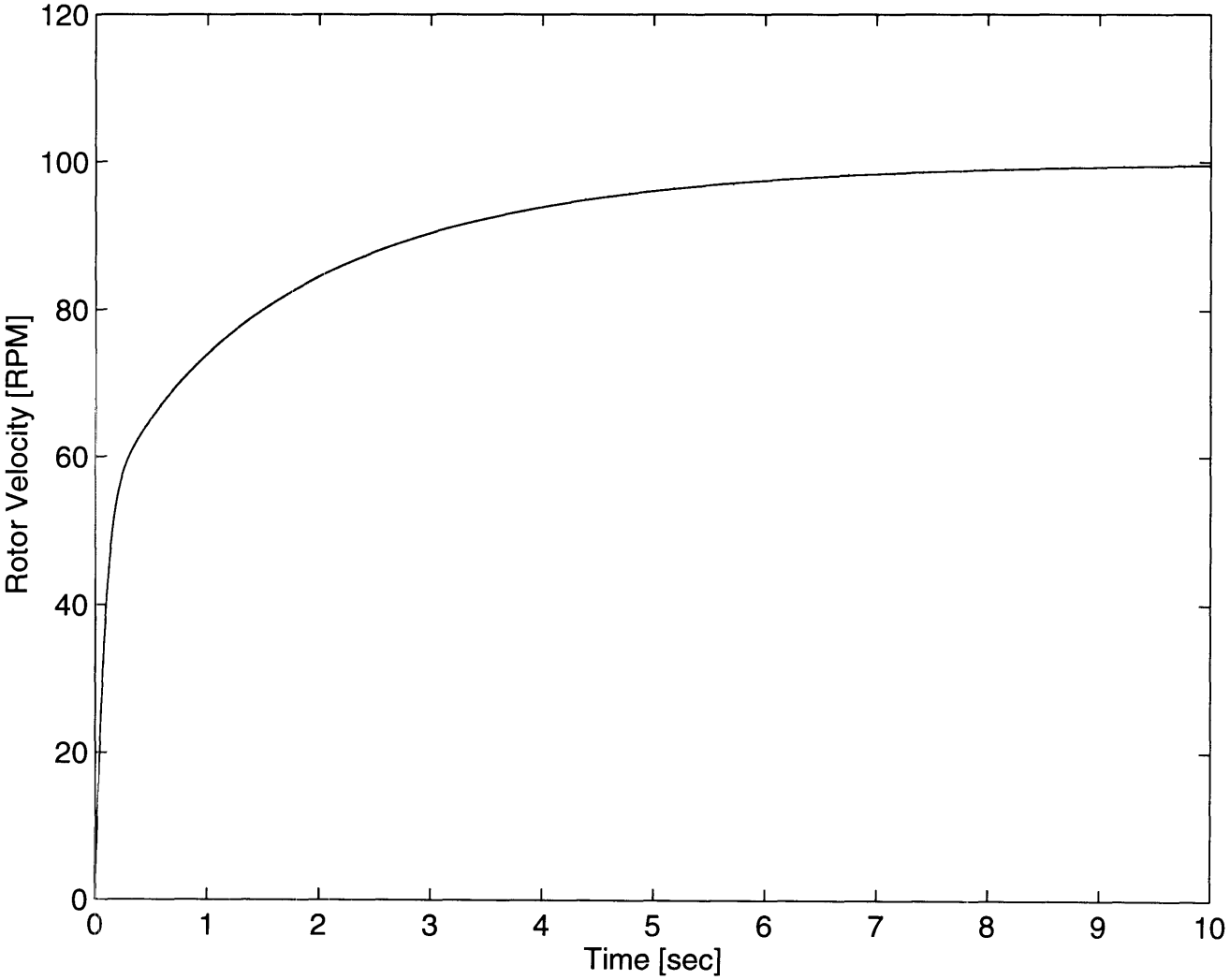

Graph 6.9: Steady–State Stator Current Waveforms, ATRR On

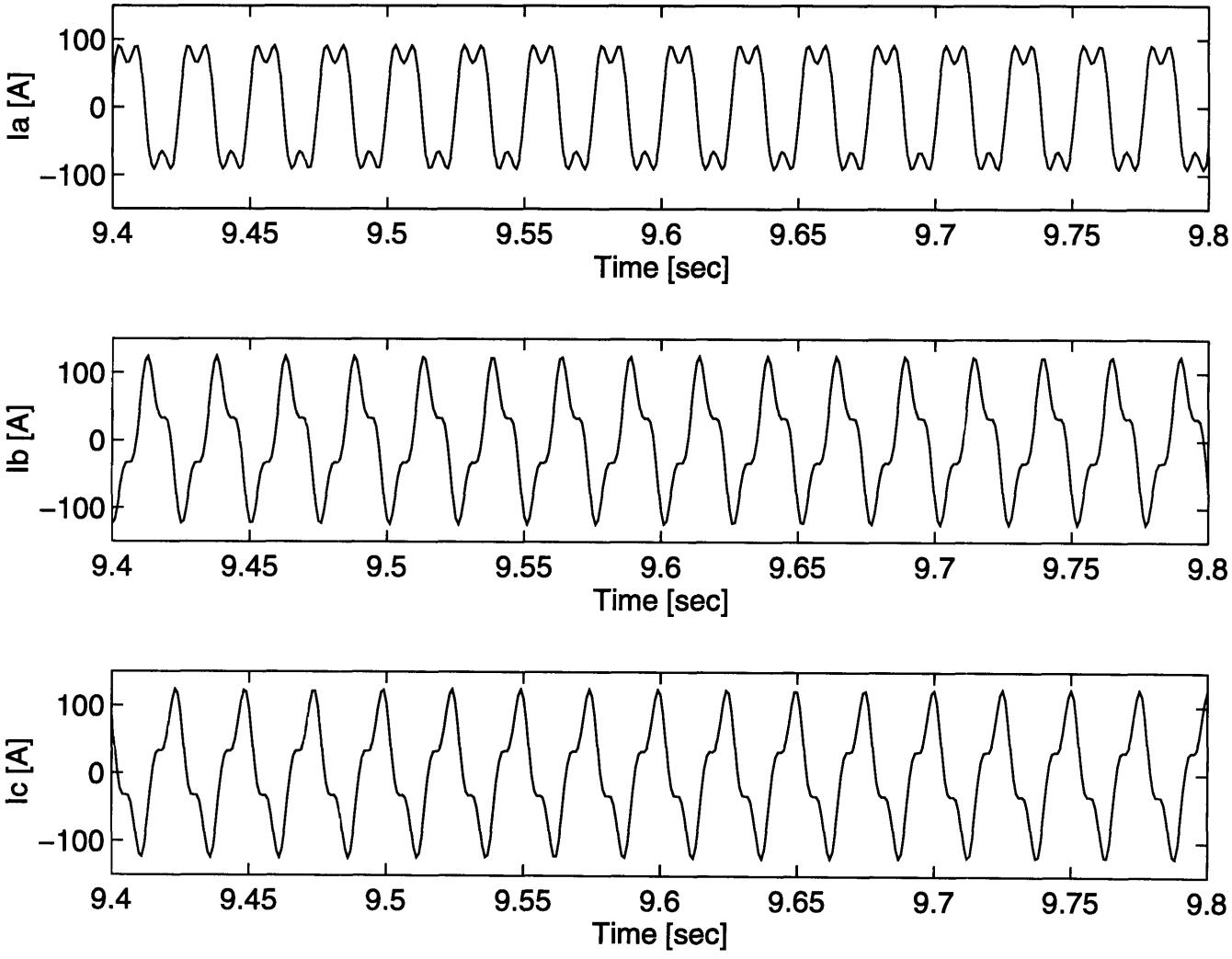

Graph 6.10: Torque Ripple Spectrum, ATRR On

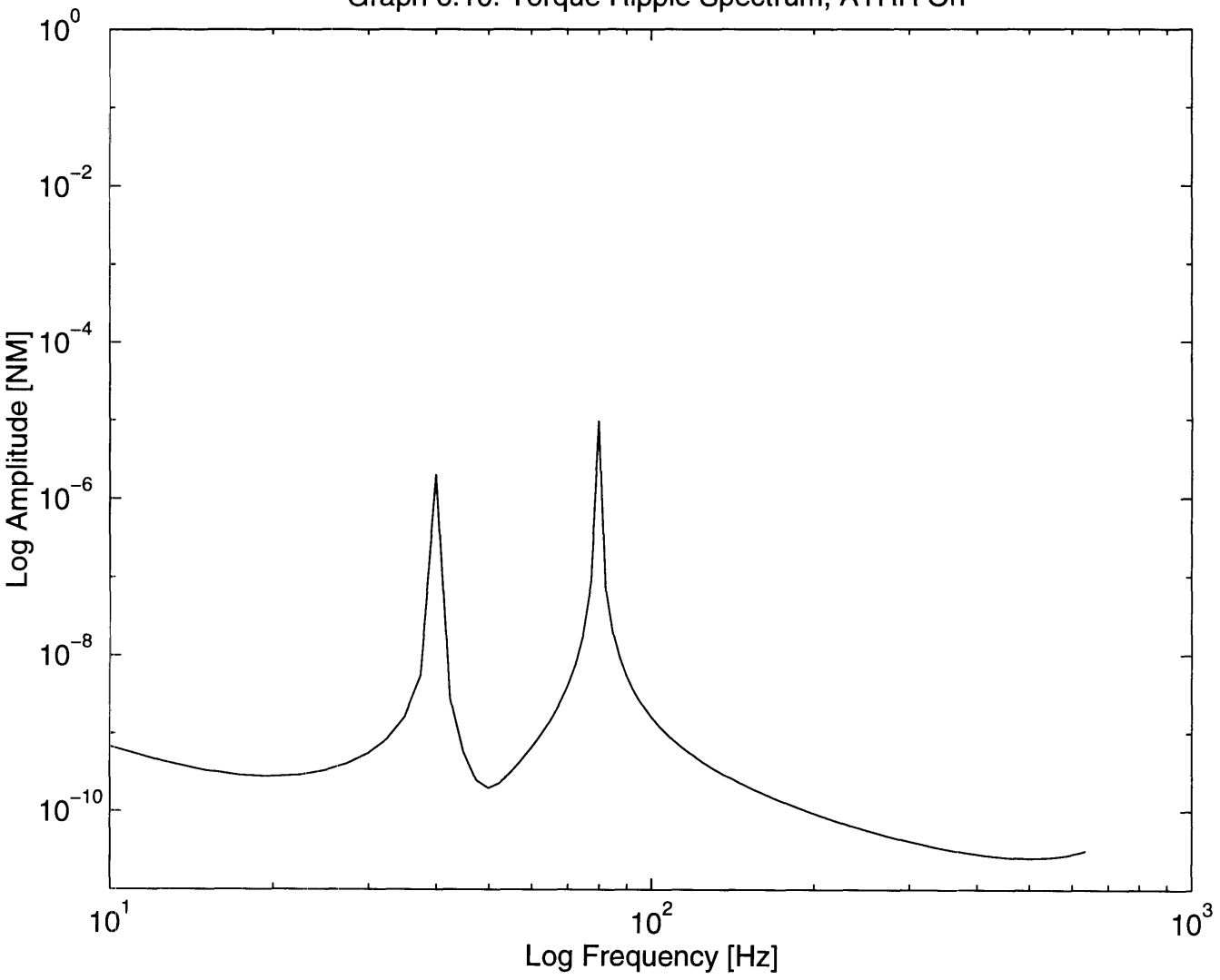

6.2.3 Limited Current Harmonics Cases

The simulation results provided in Section 6.2.3 indicate the ATRR scheme's performance at its *best*. It was assumed that the first 6 current harmonics could be exactly enforced on the stator windings. As described in Chapter 4, a number of power electronic constraints may limit the number of current harmonics which may be used resulting in a reduction in performance. **Graph 6.11** shows the torque spectrum in the case where only the first 3 current harmonics are applied to the stator windings(*i.e.* only half of the required current harmonics are available). Although the torque ripple is still reduced from the baseline case (**Graph 6.6**), the torque harmonics show only a 20 dB attenuation. The performance has clearly been reduced.

Energy efficiency is another system constraint which may effect ATRR performance. As indicated in Chapter 2, the motor's mutual inductance terms will only contain odd harmonics. Therefore, only odd current harmonics will contribute to the DC component of the generated electrical torque, see Equation **(3.48)**. Even current harmonics may be required to cancel torque ripple due to cogging harmonics, but they do not contribute to the useful work. Thus, the energy dissipated these even current harmonics reduce the overall efficiency of the motor. For a battery driven AUV system, energy efficiency is a key performance issue. As such, it may be desirable to restrict the stator current waveform to contain only odd current harmonics in the interest of a higher efficiency. **Graph 6.12** shows the torque spectrum if even current harmonics are suppressed. Although the performance is reduced in comparison to the optimal case (**Graph 6.10**), the ATRR controller still achieved a 80 dB reduction in torque ripple over the baseline. Thus, restriction of the even current harmonics result in only a small reduction in torque ripple performance.

Graph 6.11: Torque Spectrum, Higher Current Harmonics Suppressed

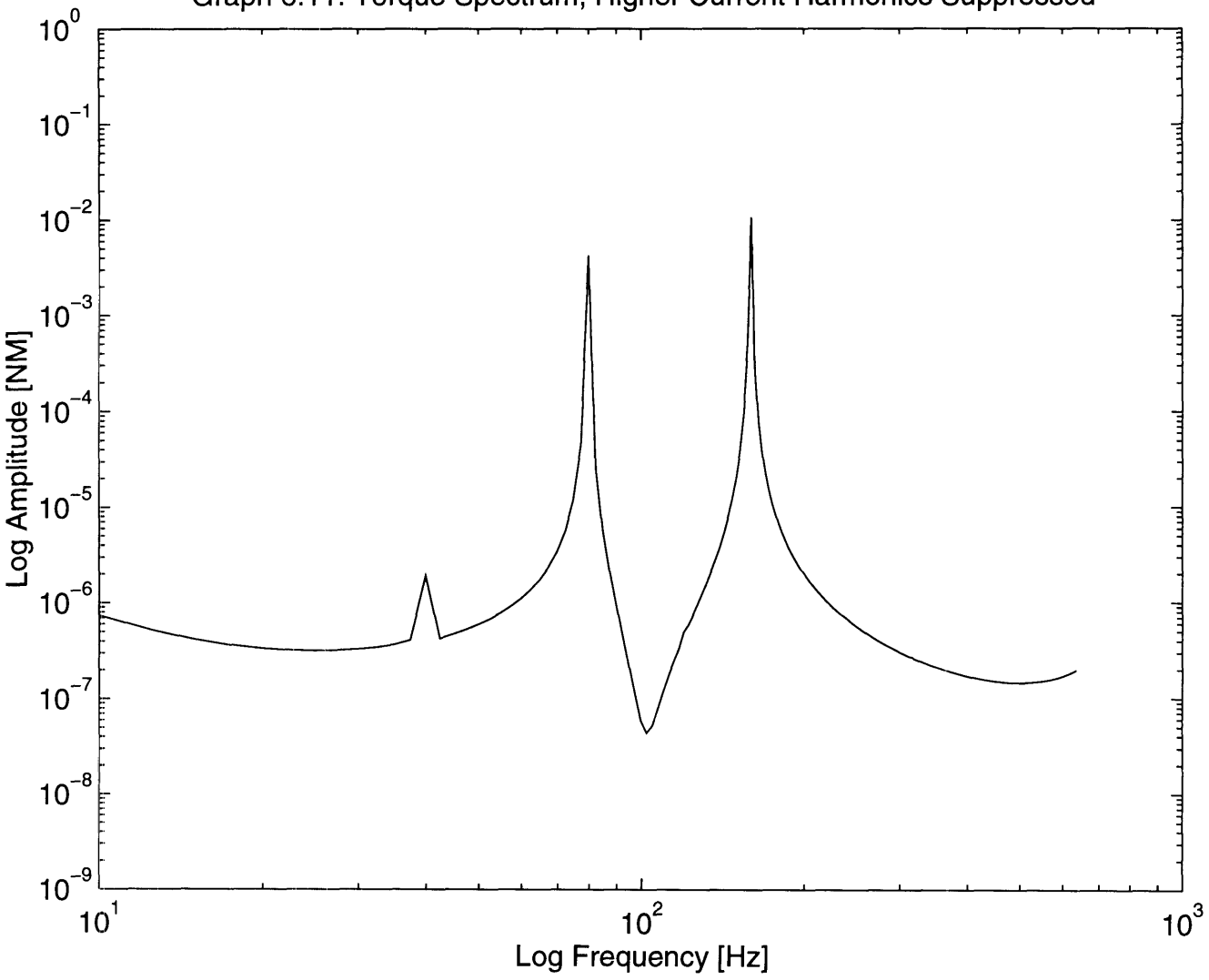

Graph 6.12: Torque Spectrum, Even Current Harmonics Suppressed

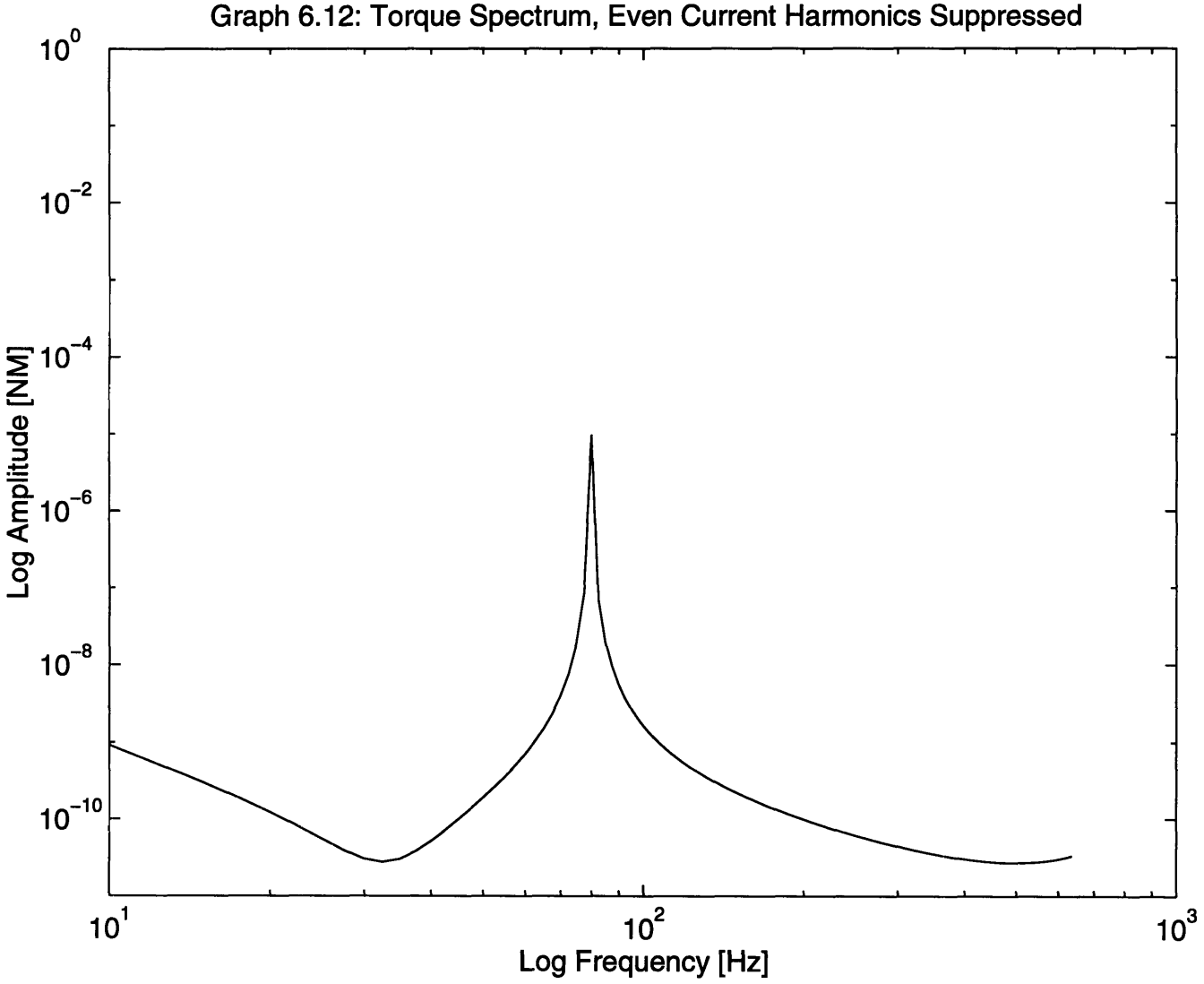

6.2.4 Extended Simulation Run

The fifth and final simulation run is intended to demonstrate the ability of the controller to perform with multiple speed commands over an extended run. **Graph 6.13** shows the commanded and actual rotor velocity profiles for this run. The commanded rotor velocity, shown as a dashed line, make step changes from rest to 100 RPM to 200 RPM. The rotor's velocity response is indicated by the solid line. The response is clearly over-damped as desired.

Graph 6.14 shows a comparison between the resulting torque signal with the ATRR scheme disabled (top) and enabled (bottom). **Graph 6.15** and **Graph 6.16** show the same torque signal comparison "blown up" at different time intervals. **Graph 6.15** shows the time interval while the motor is cruising at 100 RPM. **Graph 6.16** shows the time interval while the motor is spinning faster at 200 RPM. It is clearly indicated by all three graphs that the torque ripple is greatly reduced by the ATRR scheme.

Graph 6.13: Rotor Velocity Profile, Test Run

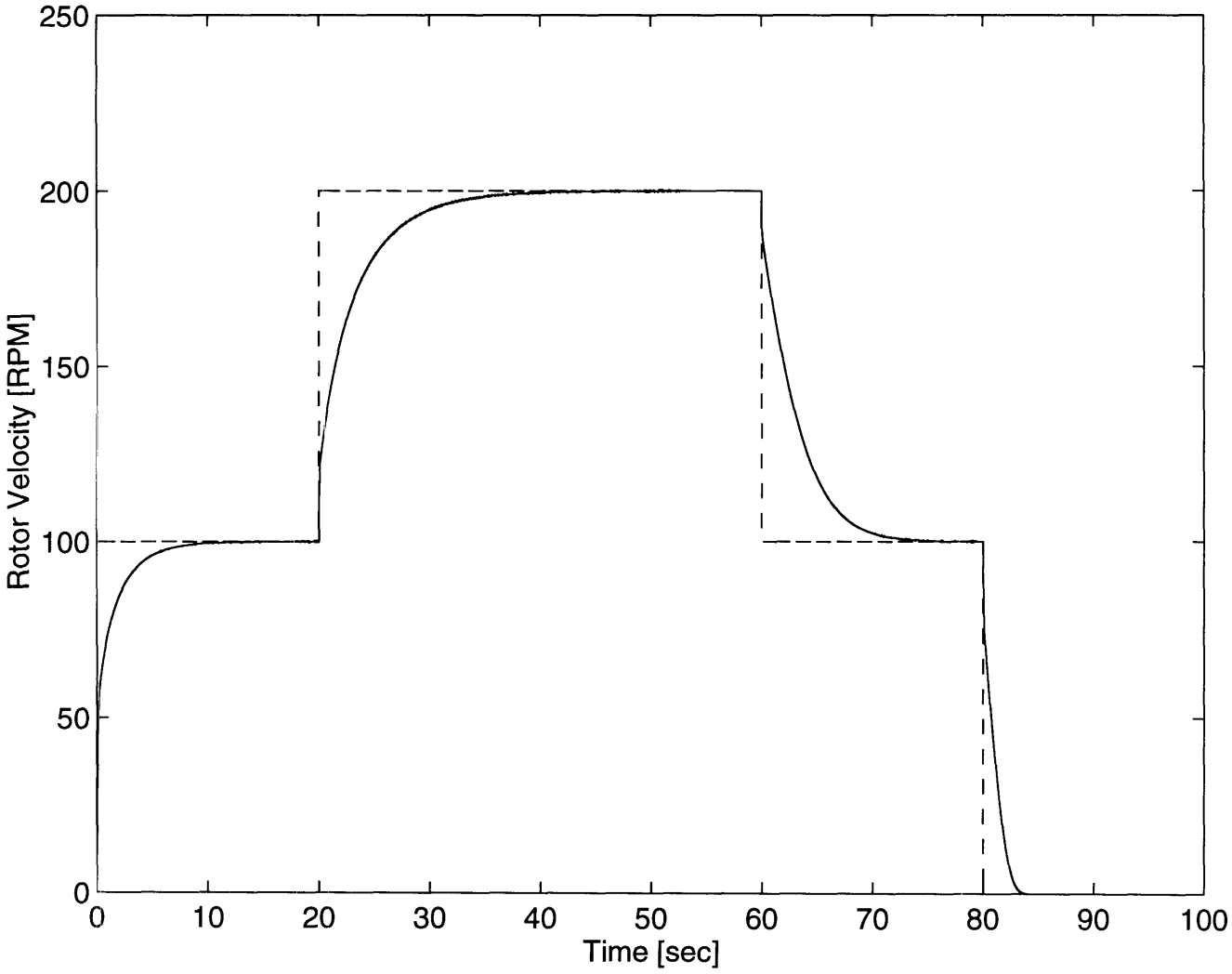

Graph 6.14: Test Run Load Torque Comparison, ATRR Off

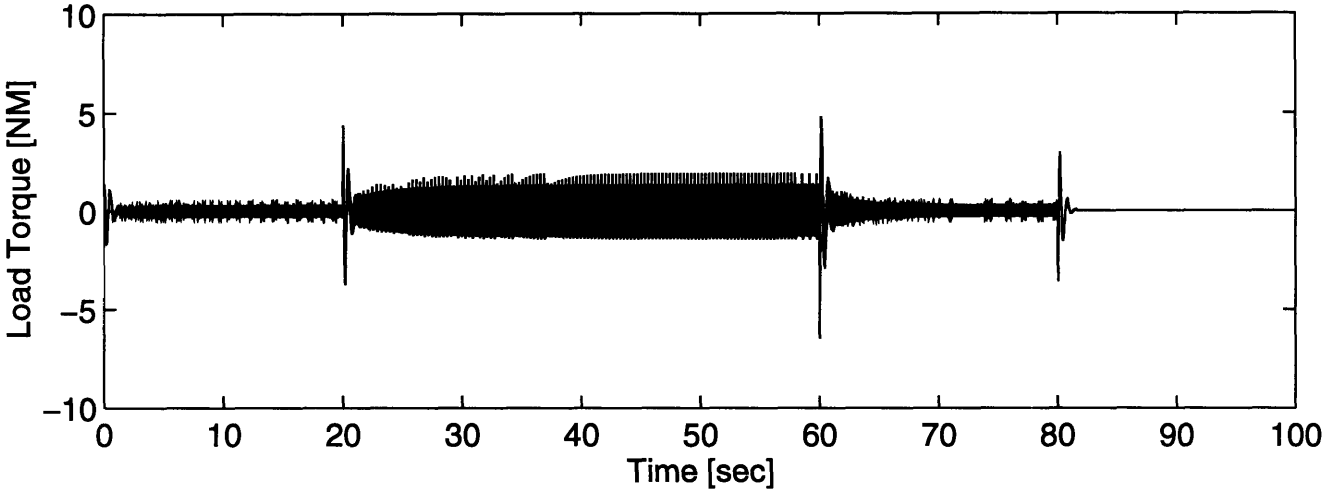

ATRR On

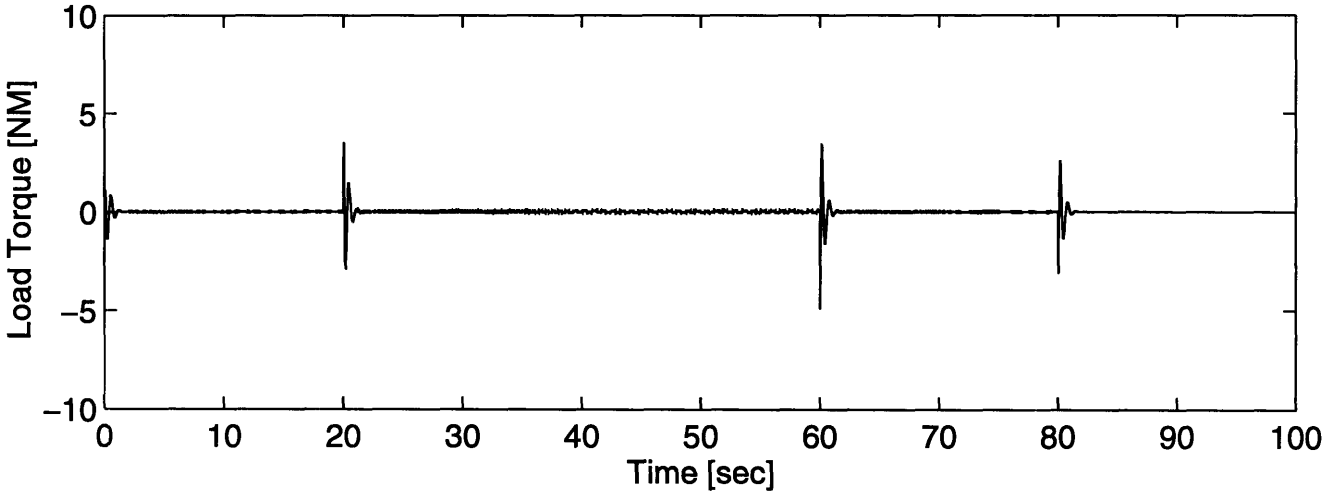

Graph 6.15: Test Run Load Torque Comparison (Zoom 1), ATRR Off

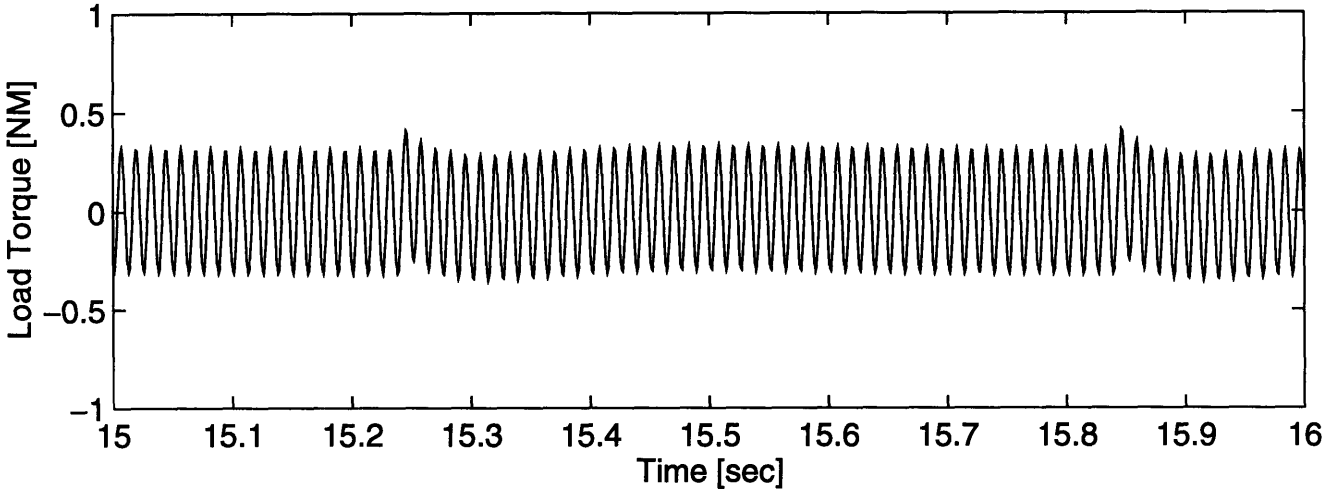

ATRR On

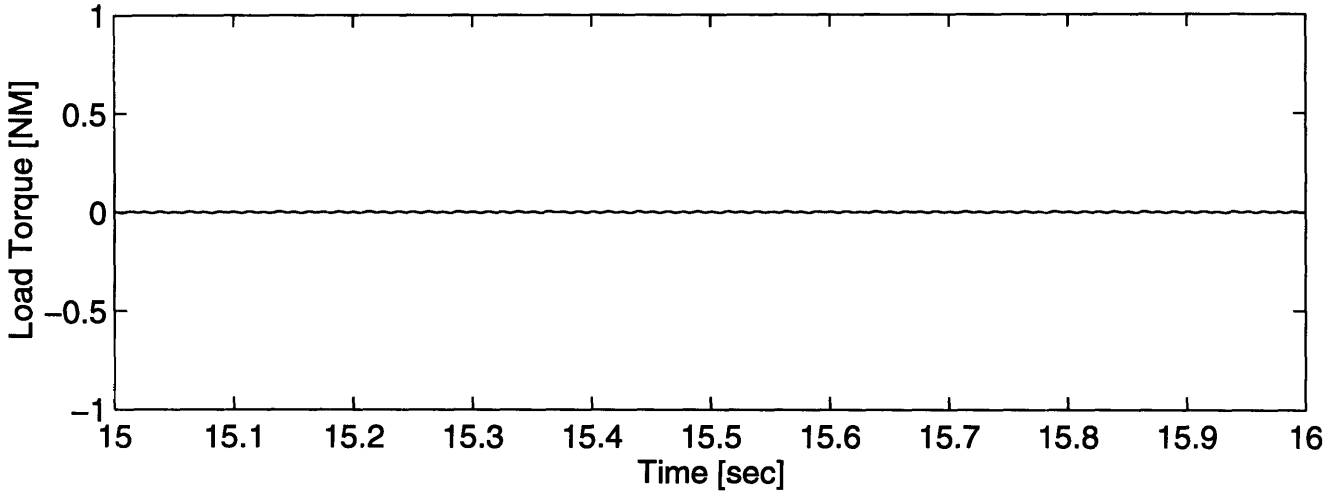

Graph 6.16: Test Run Load Torque Comparison (Zoom 2), ATRR Off

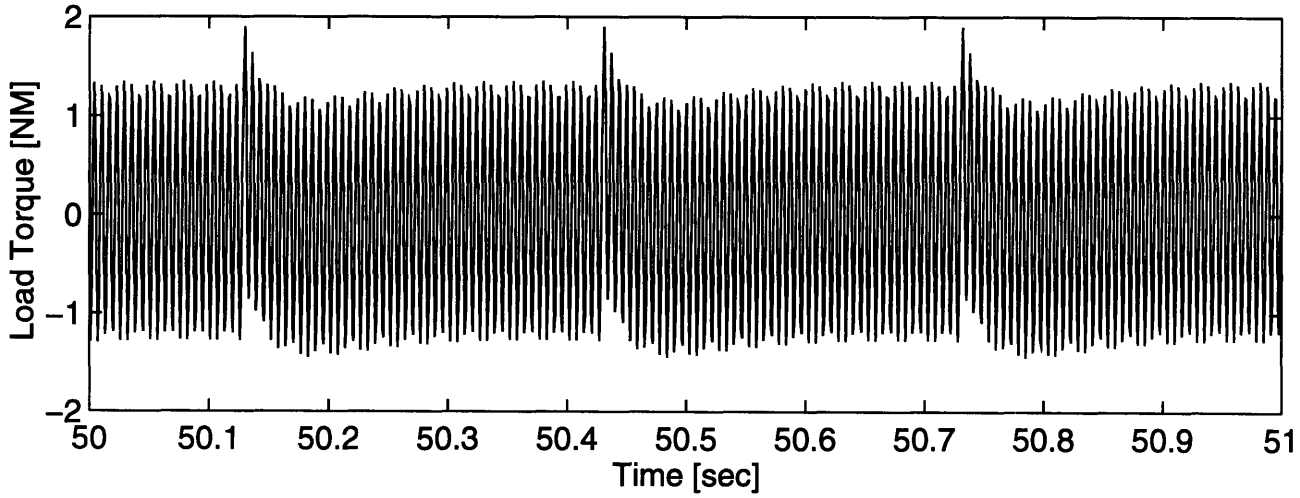

ATRR On

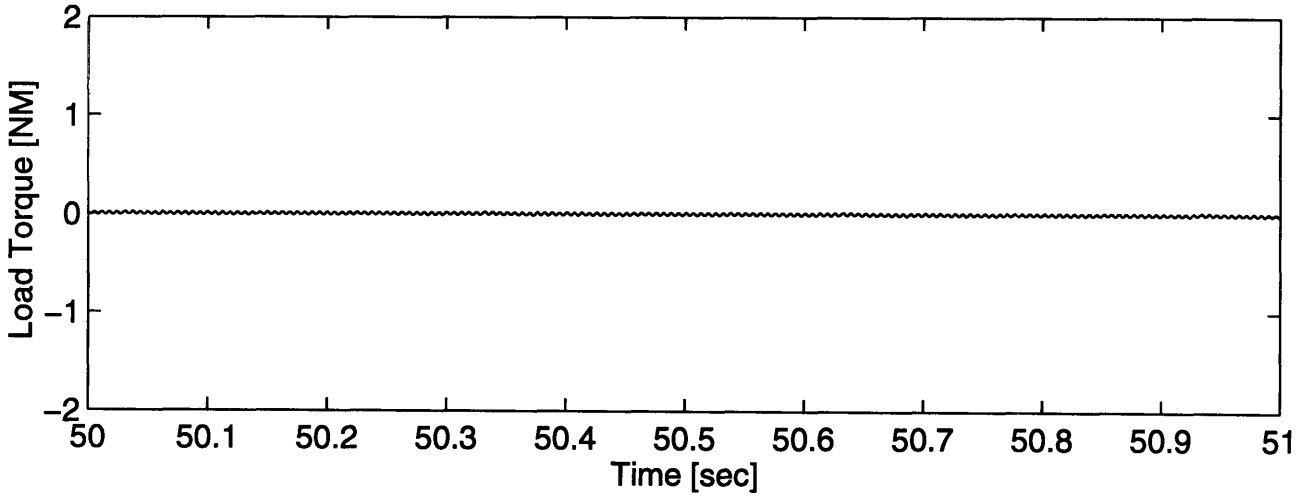

7 Conclusions

7.1 Contributions

The work described in this thesis document has made a number of contributions to the area of active torque ripple reduction especially as it applies to axial-field PMAC motors. Both sides of the problem, current selection and enforcement, are discussed and studied. The relevant issues and trade-offs are indicated, and possible solutions presented.

In the area of current selection, a model of the three-phase PMAC motor which explicitly takes into count the source of torque ripple are presented in Chapter 2. Using the generalized averaging method[25], a transformed model which provided insight into the underlying structure of torque ripple and a methodology for canceling it is presented in Chapter 3. From there, adaptive control and estimation techniques[28] are applied to the problem. A robust system for computing the required current harmonics is later presented and discussed.

In the area of current enforcement, a detailed overview of current tracking power electronics and popular PWM techniques were presented in Chapter 4. The problems associated with these traditional PWM schemes in the context of active torque ripple reduction systems were hi-lighted. Furthermore, a model based PWM scheme which uses knowledge about the stator winding dynamics to provide better current tracking performance was described and studied.

The underlying goal of this thesis is to help illuminate the complex and sometime couple issues associated with torque ripple cancellation in PMAC motor systems. It is the hope that the combination of the research presented here will to a complete system for the active reduction of torque ripple.

7.2 Summary of Results

Through the use of a detailed computer simulation, it was shown that the torque ripple reduction methodology described in this thesis could result in a significant reduction of a motor's torque ripple. The system, which requires no a priori knowledge of motor parameters, demonstrated a 100 dB reduction in torque ripple harmonics provided the required current harmonics could be imposed. It was shown that partial torque ripple reduction could still be achieved if the number enforceable current harmonics were reduced. It was demonstrated that the removal even current harmonics to improve system efficiency resulted in little degradation in performance. This result indicates promise that a low torque ripple drive system need not result in low efficiency. It was also shown that blanket removal of higher current harmonics resulted in a strong degradation in performance, demonstrating the need for high bandwidth current tracking to eliminate torque ripple. Thus, an advance current source inverter and PWM scheme are integral to achieving a low ripple drive system.

7.3 Future Work

The next logical step is the experimental implementation of the system described in this thesis document. Both the adaptive torque ripple reduction algorithm(Chapter 3) and the model reference PWM scheme(Chapter 4) are most easily implemented in software requiring that a micro-processor based test-bed be used.

References

[1] A. J. Healey and D. Lienard, "Multivariable Sliding Mode Control for Autonomous Diving and Steering of Unmanned Underwater Vehicles", *IEEE Journal of Ocean Engineering*, Vol. 18, No. 3, July 1993, pp. 327-336.

[2] D. C. Hanselman, "Sources of Torque Ripple in Brushless Permanent-Magnet Motors", *Proceedings of the International Conference on Electrical Machines*, UK, September 1992, pp. 823-827.

[3] D. C. Hanselman, "Minimum Torque Ripple, Maximum Efficiency Excitation of Brushless Permanent Magnet Motors", *IEEE Transactions on Industrial Electronics*, Vol. 41, No. 3, June 1994, pp. 292-300.

[4] D. Chen and B. Paden, "Nonlinear Adaptive Torque-Ripple Cancellation for Step Motors", *Proceedings of the 20th Conference on Decision and Control*, December 1990, pp. 3319-3324.

[5] D. Chen and B. Paden, "Adaptive Linearization of Hybrid Step Motors: Stability Analysis", *IEEE Transactions on Automatic Control*, Vol. 38, No. 6, June 1993, pp. 874-887.

[6] C. P. Cho and R. A. Bedingfield, "Cogging Torque and Rotor Misalignment Effects on Axial-Field Brushless Permanent Magnet Motors Using Finite Element Analysis", *Technical Memorandum NUWC-NPT TM 942040*, Naval Undersea Warfare Center Division Newport, R.I., May 1994.

[7] C. P. Cho, B. K. Fussell, and J. Y. Hung, "Detent Torque and Axial Force Effects In A Dual Air-Gap Axial Field Brushless Motor", *IEEE Transactions on Magnetics*, Vol. 29, No. 6, November 1993, pp. 2416-2418.

[8] H. Takano, T. Itoh, K. Mori, A. Sakuta, and T. Hirasa, "Optimum Values for Magnet and Armature Winding Thickness for Axial-Field Permanent Magnet Brushless DC Motors", *IEEE Transactions on Industry Applications*, Vol. 28, No. 2, March/April 1992, pp. 350-357.

[R9] T. Ishikawa and G. R. Slemon, "A Method of Reducing Ripple Torque in Permanent Magnet Motors without Skewing", *IEEE Transactions on Magnetics*, Vol. 29, No. 2, March 1993, pp. 2028-2031.

[10] R. Carlson, A. A. Tavares, J. P. Bastos, and M. Lajoie-Mazenc, "Torque Ripple Attenuation in Permanent Magnet Synchronous Motors"

[11] Kwang-Heon Kim, Dong-Joon Sim, and Jong-Soo Won, "Analysis of Skew Effects on Cogging Torque and BEMF for BLDCM"

[12] R. Akmese and J. F. Eastham, "Dynamic Performance of a Brushless DC Tubular Drive System", *IEEE Transactions on Magnetics*, Vol. 25, No. 5, September 1989, pp. 3269-3271.

[13] Z. Q. Zhu and D. Howe, "Analytical Prediction of the Cogging Torque in Radial-Field Permanent Magnet Brushless Motors", *IEEE Transactions on Magnetics*, Vol. 28, No. 2, March 1992, pp. 1371-1374.

[14] M. Goto and K. Kobayashi, "An Analysis of the Cogging Torque of a DC Motor and a New Technique of Reducing the Cogging Torque", *Electrical Engineering in Japan*, Vol. 103, No. 5, 1983, pp. 113-120.

[15] J. De La Ree and J. Latorre, "Permanent Magnet Machines Torque Considerations"

[16] S. Hwang and D. K. Lieu, "Characterization and Reduction of Reluctance Torque in Permanent Magnet DC Motors", *Vibration and Control of Mechanical Systems*, ASME 1993, DE-Vol. 61, pp. 217-222.

[17] Y. Kawashima and Y. Mizuno, "Reduction of Detent Torque for Permanent Magnet Synchronous Motor By Magnetic Field Analysis"

[18] G. Brentani, "The Effects of the Torque Ripple and Cogging Torque On The Instantaneous Speed Variation Of A Brushless DC Motor", *Motor-Con Proceedings*, October 1985, pp. 20-30.

[19] A. Hamler, B. Kreca, and B. Hribernik, "Investigation of the Torque Calculation of a DC PM Motor", *IEEE Transactions on Magnetics*, Vol. 28, No. 5, September 1992, pp. 2271-2273.

[20] J. De La Ree and N. Boules, "Torque Production in Permanent-Magnet Synchronous Motors", *IEEE Transactions on Industry Applications*, Vol. 25, No. 1, January/February 1989, pp. 107-112.

[21] E. Favre, L. Cardoletti, and M. Jufer, "Permanent-Magnet Synchronous Motors: A Comprehensive Approach to Cogging Torque Suppression", *IEEE Transactions on Industry Applications*, Vol. 29, No. 6, November/December 1993, pp. 1141-1149.

[22] L. A. Jones and J. H. Lang, "A State Observer for the Permanent-Magnet Synchronous Motor", *IEEE Transactions on Industrial Electronics*, Vol. 36, No. 3, August 1989, pp. 374-382.

[23] N. Matsui, T. Makino, and H. Satoh, "Auto-Compensation of Torque Ripple of DD Motor by Torque Observer", *Proceedings of the IEEE IAS Annual Meeting*, 1991, pp. 305-310.

[24] A. Khayatian and D. G. Taylor, "Feedback Control of Linear Continuous Systems by Pulse-Width Modulation", *ACC/WM7* 1992, pp. 708-712.

[25] S. Sanders, J. M. Noworolski, X. Z. Liu, and G. C. Verghese, "Generalized Averaging Method for Power Conversion Circuits", *IEEE Transactions on Power Electronics*, Vol. 6, No. 2, April 1991, pp. 251-259.

[26] R. B. Sepe and J. H. Lang, "Real-Time Adaptive Control of the Permanent-Magnet Synchronous Motor", *IEEE Transactions on Industry Applications*, Vol. 27, No. 4, July/August 1991, pp. 706-714.

[27] J. H. Lang, G. C. Verghese, M. D. Ilic, *Electrical Machine Systems: Dynamics, Estimation, and Control*, Laboratory for Electromagnetic and Electronic Systems (LEES), Dept. of Electrical Engineering and Computer Science, Massachusetts Institute of Technology, Cambridge, Massachusetts, 1994.

[28] K. J. Anstrom and B. Wittenmark, *Adaptive Control*, Addison-Wesley Publishing, 1989.

[29] Math Works Inc., *Simulink User's Guide.*

[30] W. J. Rugh, *Linear System Theory*, Prentice-Hall Publishing, 1993.

[31] J. Kassakian, M. Schlect, G. Verghese, *Power Electronic Circuits*,

[32] W. Leonhard, *Control of Electric Drives*, Springer-Verlag 1985.

[33] D. M. Brod and D. W. Novotny, "Current Control of VSI-PWM Inverters", *IEEE Transactions on Industry Applications*, Vol. IA-21, No. 4, May/June 1985 pp. 562-570.

[34] D. C. Hanselman, *Brushless Permanent-Magnet Motor Design*, McGraw-Hill 1994.

[35] H. Le-Huy and L. A. Dessaint, "An Adaptive Current Control Scheme for PWM Synchronous Motor Drives: Analysis and Simulation", *IEEE Transactions on Power Electronics*, Vol. 4, No. 4, October 1989, pp. 486-495.

[36] G. Joos, P. D. Ziogas, and D. Vincenti, "A Model Reference Adaptive PWM Technique", *IEEE Transactions on Power Electronics*, Vol. 5, No. 4, October 1990, pp. 485-494.

[37] D. S. Oh, K. Y. Cho, and M. J. Youn, "A Discretized Current Control Technique with Delayed Input Voltage Feedback for a Voltage-Fed PWM Inverter", *IEEE Transaction on Power Electronics*, Vol. 7, No. 2, April 1992, pp. 364-373.

[38] A.E. Fitzgerald, C. Kingsley, and S.D. Umans, *Electric Machinary*, McGraw-Hill 1983 Fourth Edition.